Deep-water reservoir distribution on a salt-influenced slope, Santos Basin, offshore Brazil

C. R. Rodriguez[1§], C. A-L. Jackson[2], R. E. Bell[2], A. Rotevatn[3], M. Francis[4]

[1]*Exploration Multiclient, WesternGeco Schlumberger, 10001 Richmond Avenue, Houston, Texas, 77042, United States.*

[2]*Basins Research Group (BRG), Department of Earth Science and Engineering, Imperial College London, SW7 2BP, United Kingdom*

[3]*Department of Earth Science, University of Bergen, Allégaten 41, 5007 Bergen, Norway*

[4]*WesternGeco Schlumberger, Schlumberger House, Gatwick Airport, Horley, West Sussex, RH6 0NZ, United Kingdom*

§Corresponding author email: clararodriguez@slb.com

Abstract

Studies of near-seabed datasets show that salt tectonics controls the distribution and architecture of deep-water reservoirs in many salt-influenced basins. It is typically difficult, however, to study the distribution and stratigraphic evolution of depositional systems preserved at deeper, economically significant depths, reflecting poor seismic imaging of steeply dipping strata flanking high-relief salt structures. 3D seismic and borehole data from the Santos Basin, offshore Brazil allow us to identify a range of depositional elements that form the building blocks of three main tectono-stratigraphic phases. During the first phase, channel systems and lobes were confined within updip minibasins and to the hangingwalls of salt-detached faults. During the second phase, channel systems and lobes filled updip minibasins to bypass sediment downslope, with coarse clastic deposition then occurring in downdip minibasins, >100 km from the coeval shelf margin. Syndepositional seafloor relief caused: (i) channel system deflection and diversion around salt-cored highs; (ii) channel system uplift and rotation on the flanks of rising salt structures; (iii) lateral and frontal confinement of channel systems. During the final phase, rising salt walls dissected previously deposited deep-water systems, with MTCs deposition becoming increasingly important. Our results have important implications for post-salt prospectivity in the Santos Basin and other salt-influenced sedimentary basins, with a range of reservoirs and trapping styles present in this underexplored interval. More specifically, we show that large volumes of clastic sediment were not trapped behind the 'Albian Gap', a salt-controlled depocenter dominating the north-western basin margin, but were instead delivered further basinward.

1. Introduction

Understanding the spatial distribution and temporal evolution of deep-water depositional systems relative to the style and evolution of seafloor relief is key to improving the ability to predict reservoir presence, architecture and hydrocarbon trapping styles along deep-water slopes. Seafloor relief and related controls on sediment distribution and architecture can be induced by: (i) tectonic events (e.g., Hubbard et al., 2009; Callec et al., 2010; Lin et al., 2014; Spychala et al., 2017; McArthur et al., 2019); (ii) erosional and depositional features (e.g., Deptuck et al., 2007; Kolla, 2007; Ortiz-Karpf et al., 2015; Spychala et al., 2015); (iii) mud diapirism (e.g., Morley et al., 2003; Adeogba et al., 2005); and (iv) salt movement (e.g. Rowan and Weimer, 1998; Stewart and Clark, 1999; Booth et al., 2003; Gee and Gawthorpe, 2006; Jackson et al., 2010; Mayall et al., 2010; Oluboyo et al., 2014; Doughty-Jones et al., 2017).

Here we focus on understanding how salt-induced seafloor relief interacts with deep-water sedimentation, thus controlling reservoir distribution and architecture and related trapping styles along deep-water slopes (e.g. Booth et al., 2003; Gee and Gawthorpe, 2006, 2007; Jackson et al., 2010; Mayall et al., 2010; Oluboyo et al., 2014; Sylvester et al., 2015; Doughty-Jones et al., 2017; Wang et al., 2017). Overall, these studies suggest that the style of salt-sediment interaction is a result of; i) the nature (e.g. grain-size, erosive power, etc) and temporal evolution of deep-water depositional systems; ii) downdip changes in salt-related structural style (i.e., from predominantly thin-skinned extensional styles near the updip basin margins, to thin-skinned contractional styles towards the basin center), with a key control being the orientation, scale and growth rate of structures relative to the incoming deep-water systems; and iii) the timing of sediment deposition relative to the formation, growth and decay of salt-induced seafloor relief.

Salt-induced seafloor relief can lead to lateral confinement, frontal confinement or blocking, deflection and diversion of deep-water depositional systems (e.g., Clark and Cartwright 2009; 2011; Mayall et al., 2010). Furthermore, sediment subsidence into salt can lead to the formation of minibasin; i.e., relatively small (5-30 km in diameter by up to several kilometres deep) synsedimentary depocenters (e.g. Jackson and Talbot, 1991; Hudec and Jackson, 2007, 2011; Hudec et al., 2009; Goteti et al., 2012). In salt-influenced slopes, deep-water depositional systems may fill updip minibasins before spilling into neighbouring downdip minibasins, showing progressive basinward filling or “healing” of the slope (e.g. Winker, 1996; Prather et al., 1998; Badalini et al., 2000; Booth et al., 2003; Smith, 2004; Hudec et al., 2009; Albertão et al., 2011; Jackson et al., 2010; Oluboyo et al., 2014).

Seismic reflection data are a key tool to understand how salt-influenced seafloor relief controls deep-water sediment distribution and stratigraphic architecture. Most previous seismic reflection-based studies have focused on shallowly buried (i.e. near-seafloor), relatively young deep-water depositional systems that are then used to understand salt-sediment interactions in older, more deeply buried systems (e.g., Winker, 1996; Beaubouef and Friedmann, 2000; Pirmez et al., 2000; Fonnesu, 2003; Gee and Gawthorpe, 2006, 2007; Clark and Cartwright, 2009; 2011). The salt-influenced geometry and temporal evolution of deeply buried systems have also been studied, but only over relatively small areas (within a single or a few closely spaced minibasins; e.g., Booth et al., 2003; Jones et al. 2012). In contrast, regional studies cover many minibasins, but have typically focused on detailed analysis of specific stratigraphic intervals recording relatively short time scales (ca. 15 Myrs; e.g.; Olubuyo et al., 2014).

This study focuses on central deep-water Santos Basin, offshore eastern Brazil. Here, high-quality seismic reflection and borehole data provide a rare opportunity to analyse deep Turonian-to-Paleocene deep-water clastic systems that were deposited on a salt-influenced slope. In contrast to previous studies, our data allow us to document the long-term (ca. 60 Myrs) stratigraphic record of salt-sediment interaction across >10 minibasins that cover an area of c. 20,122 km^2. Previous studies in the Santos Basin predict that little or no deep-water sand was deposited during the Turonian-to-Paleocene due to the presence of a salt-controlled intra-slope depocenter called the ‘Albian Gap’ (e.g.; Modica and Brush, 2004; Guerra and Underhill, 2012). In this study, we challenge the conclusions of these previous studies, showing evidence for the existence of deep-water depositional elements up to 100 km from the coeval shelf margin. More specifically, we: i) document the spatial and temporal variations in the size and type of deep-water depositional elements within the post-salt succession; ii) assess the key controls on minibasin development, paleo-seafloor relief and deep-water stratigraphic architecture; and iii) determine the exploration significance of this hitherto poorly explored succession. This study improves our current understanding of the distribution of and controls on, depositional systems along salt-influenced deep-water slopes, providing new insights into the tectono-stratigraphic evolution of this salt-dominated basin.

2. Geological Setting

The study area is located on the São Paulo Plateau (SPP), Santos Basin, offshore eastern Brazil (Figs. 1 a,b). The Santos Basin formed during the opening of the South Atlantic in the earliest Cretaceous, with the main Hauretivian rift phase being characterized by the development of half-graben filled with fluvial and lacustrine sediments (Guaratiba Group; Fig. 1c) (Meisling et al., 2001; Modica and Brush, 2004; Moreira et al., 2007). The end of the rift phase was marked by the deposition of the main source rocks and reservoirs in the Santos Basin; these included organic-rich lacustrine mudstones and carbonates of the Barremian 'sag' sequence (upper Guaratiba Group), which largely filled and smoothed relict rift-related topography (Fig. 1c; Meisling et al., 2001; Modica and Brush, 2004; Moreira et al., 2007). Episodic marine incursions and an arid climate during the Aptian promoted deposition of the Ariri Formation, an up-to-2.5 km-thick evaporite-dominated succession (Fig. 1 c, d; e.g. Modica and Brush, 2004; Davison, 2007; Karner and Gambôa, 2007; Moreira et al., 2007; Gambôa et al., 2008; Davison et al., 2012; Fiduk and Rowan, 2012; Jackson et al., 2014a; Rodriguez et al., 2018). During the Albian, a shallow-marine carbonate platform was established near the basin margin, with deep-water marlstones deposited basinward in deeper waters (Itanhaem Formation; Figs. 1c,d; e.g., Modica and Brush, 2004). Salt-related deformation commenced in the Albian, with margin tilting and the downslope flow of salt causing stretching and faulting of the carbonate platform, and the development of normal fault-bound rafts in the upslope extensional domain (Fig. 1c; e.g.; Davison et al., 2012; Guerra and Underhill, 2012; Jackson, 2012).

In the Late Cretaceous, periodic uplift and erosion of the onshore Serra do Mar mountain belt drove progradation of a thick clastic wedge into the Santos Basin (Itajai-Acu Formation; Fig. 1c,d; e.g., Modica and Brush, 2004; Moreira et al., 2007; Guerra and Underhill, 2012). Regional paleogeographic mapping based on widely spaced 2D seismic reflection and limited borehole data suggest large volumes of sediment were supplied by the Paraiba do Sul river drainage system, which at this time lay to the N and NW of the São Paulo Plateau (Fig. 2a, Modica and Brush, 2004). However, according to Modica and Brush (2004), much of this sediment was trapped in a relatively proximal setting due to formation of the Albian Gap, a large (4 km thick, 200 km long, 10 km wide), salt-controlled, intraslope depocenter bounding the seaward limit of the extensional domain (Figs. 2 a,b; Jackson et al., 2015a). The interpretation of Modica and Brush (2004) thus argues for limited sediment dispersal to the slope during the Late Cretaceous, implying limited deep-water prospectivity on the São Paulo Plateau (Fig. 2a). Late Campanian-Maastrichtian uplift of the Serra do Mar deflected the Paraiba do Sul river drainage system to the NE, starving the central deep-water Santos Basin of sediment (Fig. 2b; Cobbold et al., 2001; Modica and Brush, 2004; Guerra and Underhill, 2012). Subsequently, during the Eocene, sediment supply to the basin was thus largely derived from catastrophic failure of the middle Eocene shelf margin, which produced debris flows and turbidites of the

Lower Marambaia Formation that were locally trapped in the proximal domain (Fig. 2c). Previous studies also suggest the upper Marambaia Formation varies little in thickness and is dominated by fine-grained sediments, recording a global marine flooding event and sea level highstand (Figs. 1c, d; Modica and Brush, 2004; Moreira et al., 2007; Guerra and Underhill, 2012).

By integrating 3D seismic reflection and borehole data we here show that: (i) deep-water systems of the Itajai-Acu Formation were deposited on the São Paulo Plateau, some distance seaward of the Albian Gap and the coeval Late Cretaceous shelf edge; and (ii) large thickness variations occur within the Marambaia Formation due to continue salt diapirism, and the emplacement of relatively small, intra-minibasin and larger, shelf-derived mass transport complexes (MTCs).

3. Data and methods

In this study, we integrate a 20,122 km^2, high-quality, three-dimensional, post-stack time-migrated seismic reflection dataset provided by CGG, and eight publicly available boreholes (Fig. 1b). The dataset is located in the central deep-water Santos Basin, 200 km southeast of the present Brazilian shelf edge and 200 km southwest of the Campos Basin (Fig. 1b). The seismic dataset contains trace information from sea level down to 5.5 second two-way time (s, TWT), with a vertical sample rate of 4 ms, inline spacing (east-west) of 18.75 m and crossline spacing (north-south) of 25 m. Data from four boreholes indicate that vertical seismic resolution within the post-salt varies not only with depth, but also spatially due to variations in composition (Fig. 3, and Table 1). Vertical resolution within the post-salt sequence decreases from c. 8 m at relatively shallow depths (<2500 ms TWT), to up to 31 m where the post-salt sequence is relatively thick (4500 ms TWT), to up to 64 m where the post-salt sequence is thickest (>5000 ms TWT) (Fig. 3 and Table 1). This decrease in seismic resolution limits the opportunity to identify and map depositional systems occurring deep within the post-salt sequence. Seismic profiles are displayed with SEGY normal polarity, where a downward increase in acoustic impedance is represented by a positive reflection event (red) and a downward decrease in acoustic impedance is represented by a negative reflection event (blue) (inset on Fig. 3). The boreholes contain lithology information and formation markers. Well-log data are restricted to the pre-salt and salt sequences. Only borehole 329D, which penetrates the center of a minibasin encircled by salt diapirs, contain age data for the post-salt interval (Figs. 3 and 4).

We mapped seven key seismic horizons and correlated these to stratigraphic information (e.g. age, lithology) provided by borehole 329D (Fig. 3). We chose horizons defining clear vertical changes in seismic facies, or which correlated to major lithological breaks or unconformities identified in boreholes. The key seismic horizons are of high-amplitude and are regionally mappable, whereas other horizons can only be locally interpreted within a few updip minibasins in the north of the study area (e.g.; intra-units 2, 3 and 4 horizons, Fig. 3). These seismic horizons were used to generate seismic isochron maps of key stratigraphic intervals that illustrate how syndepositional, salt-induced subsidence and uplift varied in space and time, and how this then impacted the development of deep-water depositional systems.

We use a range of volume- and surface-based seismic attributes to identify and map deep-water depositional elements (Table 3); i.e.; (i) *amplitude contrast*, which calculates amplitude derivatives between neighbouring seismic traces in order to highlight salt structures, faults and mass transport complexes (Schlumberger, 2012); (ii) *variance*, which identifies abrupt lateral changes in seismic reflection continuity (Hart, 2008); and (iii) *sweetness*, which integrates amplitude strength (envelope) and instantaneous frequency to highlight lateral changes in seismic facies variations related to inferred changes in lithology (Hart, 2008). We visually blend sweetness and variance to identify and analyze seismic geomorphology of deep-water depositional elements (Fig. 3; see also Hart, 2008). By integrating seismic reflection and borehole data, we identify three main seismic facies (i.e., SF1-SF3; Fig. 3 and Table 2). The integration of map and section views with borehole derived lithology data was central to our interpretation of deep-water depositional elements along the slope.

4. Minibasin structure and stratigraphy

Based on their location relative to the present shelf-edge, their map-view geometry, and the thickness of sediment they contain, we recognise three intraslope minibasin types: (i) *proximal thick minibasins* (e.g; minibasins A, B, C, D, E; Figs. 4a, b, c); (ii) *medial shallow minibasins* (e.g.; minibasins F, G, H; Figs. 4a, b, d); and (iii) *distal elongated minibasins* (e.g.; minibasins I, J, K, L, M; Figs. 4a, b, e). Seismic facies mapping and borehole-derived lithological data also indicate minibasin structure, bulk composition, and, therefore, likely depositional environment, vary in time and space (Fig 4). We define five key stratigraphic units based on vertical seismic facies variations within the minibasins (i.e., units 1-5; Figs. 3 and 4c-e). The approximate age of each unit is largely based on a tie to stratigraphic age information provided by boreholes 329D and 723C (Figs. 3 and 5b). Our age assignments are broadly consistent with, and are thus supported by, regional seismic and stratigraphic data presented in several previous studies (e.g. Modica and Brush, 2004; Moreira et al. 2007; Contreras et al., 2010; Guerra and Underhill, 2012). In this section, we describe the structure and bulk stratigraphy of these minibasins, before outlining their tectono-stratigraphic development and the geomorphology of the deep-water depositional elements they contain.

4.1 Proximal thick minibasins:

***Structure**:* The updip, most proximal part of the study area, immediately seawards of the coeval shelf edge break, is characterized by relatively thick (> 2.5 km, 1.5 mi) minibasin-fill that are underlain by relatively thin (< 500 m, 1640 ft.) or apparently welded salt (e.g.; minibasins A-E; Figs. 4a, b, c; see also Jackson et al., 2014b). The minibasins trend N to NE, are up to 30 km (19 mi) long and 5 km (2.4 mi) wide, and are bound by similarly trending, upright salt walls that are up to 5 km (2.4 mi) wide. Internally, the bases of most minibasins are defined by 'bowl'-shaped packages (*sensu* Rowan and Weimer, 1998), which appear to record deposition of Unit 1 during simple vertical subsidence into underlying thick salt (Fig. 4c). Units 2 and 3 within minibasins B, D and E were also deposited during simple vertical subsidence as suggested by the 'bowl-like' shape of the deepest seismic-stratigraphic units. In contrast, rather than being dominated by bowl-shaped packages, the middle and upper parts of some minibasins are defined by 'wedge'-shaped packages, suggesting the latter stages of subsidence were characterized by asymmetric subsidence and minibasin tilting (e.g.; units 2, 3 and 4 in minibasins A, C; Fig. 4c).

We interpret that minibasin tilting occurred as salt was preferentially expelled from beneath one side of the subsidence depocentre. Differential salt evacuation, coupled with localised welding, caused lateral migration of the earlier-formed depocenter from the minibasin centre to one of its margins (e.g., minibasins A and C, Fig. 4c; see Jackson and Cramez, 1989; Rowan and Weimer, 1998; Hudec et al., 2009; Jackson et al.2014b). Our interpretation that minibasin welding led to asymmetric subsidence and the deposition of wedge-shaped packages is also supported by the local development of turtle-structure anticlines, which reflect structural inversion of minibasin stratigraphy (minibasin C, Fig. 4c; see Trusheim, 1960; Jackson and Cramez, 1989; Duval et al. 1992; Hudec et al., 2011; Jackson & Hudec, 2017).

Stratigraphy*:* A borehole penetrates the central, deepest part of a partly-enclosed proximal deep minibasin (minibasin C, Figs. 3, 4c). This borehole indicates the Unit 1 is dominated by interbedded Albian-Cenomanian marlstone and mudstone (c. 87%), with lesser proportions of coarser-grained carbonate (c. 12%) and clastics (c. 1%). In contrast, overlying units are relatively sandstone-rich (c. 45%), although very fine-grained lithologies (i.e. mudstone) still dominate (>50%; Unit 2 and Unit 3; Fig. 3). The unit capping the minibasins (i.e., Unit 5) is mudstone-dominated (Fig. 3).

4.2 Medial shallow minibasins:

Structure*:* The eastern, most distal part of the study area, which bounds the western flank of the Outer São Paulo Fold belt (*sensu* Jackson et al. 2015b), is characterized by minibasin-fill that are thinner (<1.5 km) than those further west (e.g., minibasins F, G, H; Figs. 4 a, b, d). The shallow minibasins are underlain by relatively thick salt (> 2 km) and welds are absent. The minibasins are sub-circular to oval in planform, are up to 20 km long and 10 km wide, and are enclosed by narrow (<2 km), nearly-triangular diapirs and salt-cored buckle folds (Fig. 4d).

The salt-cored structures bounding the shallow minibasins trend either NE or NW, thus defining a crude polygonal pattern (Fig. 4a, b). Internally, Units 1, 2 and 4 are characterized by negligible thickness variations along the shallow minibasins, although local bowl-shaped packages are suggestive of deposition during simple vertical subsidence into underlying thick salt (e.g., minibasin F; Fig. 4d). Instead, Unit 3 is defined by thin (<200 m) wedge-shaped packages indicating deposition during asymmetric subsidence (e.g., minibasins F, H; Fig. 4d).

Stratigraphy*:* A borehole penetrating a distal shallow minibasin indicates that Unit 1 comprises only interbedded mudstone and marlstone (borehole 369A, Fig. 5a). Likewise, the overlying post-Cenomanian units (2-4) are also dominated (c. 80%) by very fine-grained lithologies (i.e. mudstone and marlstone). However, even in this relatively distal location, some sandstone (40 m net thickness) occurs within Unit 3 (i.e. borehole 369A, Figs. 4d, 5a). The unit capping the minibasins comprises only mudstone and marlstone (Unit 5, Fig. 5a).

4.3 Distal minibasins:

Structure*:* Downdip, in the most distal location of the study area includes part of the Inner São Paulo Plateau Fold Belt (ISPFB, *sensu* Jackson et al. 2015b). This area is characterized by north-south oriented minibasins that are up to 30 km long and 5 km wide. Strata within this minibasins are relatively thin (<1.5 km) and the minibasin-fill are typically underlain by relatively thick salt (c. 1 km; Fig. 4a, b). Some thicker (up to 2.5 km) minibasins overlying thin (<100 m) salt are also locally developed (e.g. minibasin M, eastern part of Fig. 4e). The distal minibasins are bound by salt walls that have flat or rugose-tops, or broadly N-trending, salt-cored anticlines (e.g., minibasins L, M, Fig. 4e; e.g., Jackson et al. 2014a, 2015b). The distal minibasins are internally deformed by NE-trending, salt-cored buckle folds that are spaced approximately 5 km from one another (e.g, minibasins J and K, Fig. 4e). Internally, Unit 1 and Unit 2 are concordantly folded above the salt-cored buckle folds with local development of bowl-shaped packages characteristic of deposition during vertical minibasin subsidence (e.g., minibasin M; Fig. 4e). In contrast, Unit 3 is of variable thickness, defining relatively thin (<200 m), wedge- and bowl-shaped packages that overlie Unit 2 across an incision surface (Fig. 4e). Units 4 and 5 cap the distal minibasins and the flat-topped, bounding salt walls (Fig. 4e).

Stratigraphy: Most of the boreholes penetrating the Inner São Paulo Fold Belt and the distal minibasins indicate Unit 1 is comprised of interbedded mudstone and marlstone (Itanhaem Formation; boreholes 532A, 723C, 709, 594, Fig. 4a). However, a notable exception occurs on the eastern flank of minibasin K, where Unit 1 contain relatively coarse-grained lithologies (e.g. c. 63 m net thickness of siltstone and c. 22 m net thickness of sandstones; borehole 723C, Fig. 5b). The overlying post-Cenomanian units are also dominated by fine-grained lithologies (mudstone, c. 70% of total unit thickness), except on the eastern flank of minibasin K where relatively coarse-grained lithologies occur (i.e., siltstone, borehole 723C, 80% of total unit thickness, 170 m net thickness; Fig. 5b). Sandstone is rare (<5% of total unit thickness), with volumetrically minor proportions only locally developed (i.e. 723C, c. 27 m net thickness, Unit 3, Fig. 5b). In a similar way to the more proximal minibasins, the unit capping the distal minibasins is mainly composed of mudstone (>81% of total unit thickness), although interbedded carbonate, sandstone and siltstone occur in its lower part (Fig. 5b)

5. Deep-water depositional elements

Having defined the key types and bulk lithological trends within the intraslope minibasins, we here integrate seismic stratigraphy and seismic attribute analysis to identify, describe and map the deep-water depositional elements they contain (Table 3). We identify five main seismic geomorphic elements, which we infer represent the following deep-water depositional elements; i) channels (with and without lateral accretion packages (LAPs); ii) levees; iii) lobes; iv) MTCs; and v) background deposits (Table 3).

Channels

In cross-section, this depositional element is characterized by 20-150 m thick packages of parallel, continuous, flat-lying, moderate-to-high amplitude seismic reflections (Table 3). Package bases are flat and only weakly erosional (Table 3). In plan-view, these packages define relatively narrow (0.2-3 km), elongate (up to 200 km), low sinuosity (<1.5), channel forms that pass downdip into lobe-shaped depositional elements. We note these channel forms are defined by SF1, i.e., relatively high amplitudes, and high sweetness and low variance values, suggesting they are sandstone-prone (Table 2). This interpretation is supported by borehole 329D, which penetrates a channel feature and that indicates high-amplitude, continuous seismic facies correspond to the presence of sandstone (SF1; Fig. 5). Based on this observation and by comparison to other borehole-calibrated, seismic reflection-based studies (e.g. Prather et al. 1998; Samuel et al., 2003), we infer channel depositional elements defined by relatively moderate-to-low amplitudes are filled by finer-grained lithologies such as siltstone or mudstone.

Based on their seismic expression, geometry and scale, and by comparison to notable examples from other deep-water margins, this depositional element is interpreted as the seismic expression of turbidite-fed, relatively low-sinuosity, submarine channels (e.g. Gulf of Mexico, Prather et al., 1998, Prather 2003; Nile Delta, Samuel et al., 2003, Espirito Santo Basin; Alves et al., 2009; Lower Congo Basin, offshore Angola; Kolla et al. 2000; Mayall and Stewart; 2000; Fonnesu, 2003; Mayall and O'Byrne, 2002; Gee and Gawthorpe; 2006, 2007).

The inner bends of the relatively sinuous submarine channels (sinuosity index of at least 1.5) are characterized by up to 50 m thick, stacked packages of moderate-to-high-amplitude reflections that dip in towards the channel axis. Seismic attribute analysis indicates these crescent-shaped dipping reflections have a strike extent (i.e. parallel to the overall channel trend) of up to 1 km wide and dip extent (i.e. normal to the overall channel trend) of up to 5 km (Table 3). Boreholes do not penetrate the dipping reflections, although their high amplitudes and high sweetness values suggest they are sandstone-dominated.

The inner bend dipping reflections could represent intra-channel terrace deposits (Deptuck et al., 2007; Hansen et al., 2017). Such deposits are however typically defined by flat-lying rather than dipping reflections, being cross-cut by inclined, more poorly imaged erosion surfaces that dip in towards the channel axis and which document relatively abrupt shifts in the channel position during net lateral migration (Hansen et al., 2017; Babonneau et al., 2010). An alternative interpretation is that the dipping reflections represent lateral accretion packages (LAPs) that developed due to lateral migration of the adjacent channel (cf. Kolla et al., 2000; Abreu et al. 2003; Janocko et al. 2013). This interpretation is consistent with the overall geometry of these features (i.e. inward dip towards the channel axis) and their development only on the inner bends of relatively sinuous channels. Although LAPs previously reported at outcrop are significantly smaller, and more specifically thinner, than those documented here (e.g. up to 13 m thick in the lower Isaac Formation, British Colombia, Canada; Arnott, 2007; up to 4 m thick in the Rosario Formation of Baja California, Mexico; Dykstra & Kneller, 2009), our examples from the Santos Basin are comparable in scale to those described using 3D seismic reflection data from offshore west Africa (up to 40 m, Abreau et al. 2003; up to 50 m, Janocko et al. 2013).

Levees

Some of the submarine channels are locally flanked by wedge-shaped seismic packages of subparallel, low-to-moderate amplitude seismic reflections that are thickest (up to 150 m but typically thinner) immediately adjacent to the channels (Table 3). Due to the predominantly low-amplitude seismic reflections these elements are not clearly imaged by surface attributes. However, isochron maps indicate this depositional element is up to 5 km wide, up to 10 km long in dip extent, and are typically asymmetrically developed on both sides of the channel (isochron map on Table 3). None of the boreholes available penetrate this depositional element; however, these wedge-shaped seismic packages are characterized by low-to-moderate- amplitudes and sweetness values, suggesting they are composed of relatively fine-grained lithologies such as siltstone or mudstone.

Based on their seismic expression, geometry, scale and development adjacent to submarine channels, we interpret these depositional elements as levees, deposited by sediment gravity currents that escaped from their channels. Geometrically similar features are identified in many deep-water basins (e.g. Fonnesu, 2003; Viana et al., 2003; Gee and Gawthorpe, 2006, 2007; Clark and Cartwright, 2009, 2011; Janocko et al., 2013; Oluboyo et al., 2014; Ortiz-Karpf et al., 2015).

Lobes

This depositional element is defined by tabular to mounded packages of subparallel, continuous, moderate-to-high-amplitude reflections. These packages are up to 10 km long, 5 km wide and 200 m thick, thinning towards their fringes. Bidirectional downlap onto underlying strata is also observed in distal locations (Table 3). The plan-view morphology of this element ranges from sub-rounded, to lobate, to elongate occurring at the mouth of channel depositional elements (Table 3). Based on their high-amplitude character and moderate-to-high-sweetness values, we infer this depositional element is sandstone-dominated. This inference is supported by borehole data, which indicates some of the units containing these depositional elements are sandstone-bearing (Unit 2, Unit 3, 329D and Unit 3 in 723C, 369A; Figs. 3, 5). Further support for a sandstone dominated composition comes from the mounded externally morphology of these features, which may reflect differential compaction between the lobes and adjacent finer-grained sediment.

Based on their geometry in map- and section-view, we interpret these depositional elements as lobes that occur at the mouth of and are genetically linked to updip submarine channels (cf. Gee and Gawthorpe, 2006, 2007; Saller et al., 2008; Prélat et al., 2010; Oluboyo et al., 2014; Doughty-Jones et al., 2017).

Mass-transport complexes (MTCs)

This depositional element is characterized by up to 200 m thick, 50 km long packages of discontinuous to chaotic, low-to-moderate amplitude reflections (Table 3). The basal surface of this element is either sharp and apparently not erosional, or highly irregular and defined by 'v'-shaped grooves. The upper surfaces are invariably rugose. The plan-view morphologies of these elements are fan-shaped, defined by laterally extensive subparallel lineations or locally ponded within the minibasins (Table 3). Within these chaotic intervals we recognise laterally restricted 'blocks' of parallel, continuous moderate-to-high-amplitude reflectivity. These blocks are up to 100 m thick, 1 km long and 5 km wide.

Based on the seismic stratigraphy and geometry, we interpret these depositional elements as mass-transport complexes (MTCs). The chaotic seismic facies likely represent highly disaggregated, debritic material, whereas the coherent packages represent relatively coherent slide blocks (cf. Posamentier and Kola, 2003; Gee and Gawthorpe, 2006, 2007; Gamboa et al. 2010; Jones et al. 2012; Oluboyo et al. 2014).

Background deposits

This depositional element dominates the stratigraphic fill of all minibasins, encasing the depositional elements described above. This depositional element is characterized by parallel, continuous, high-frequency, low-to-moderate amplitude reflections, although subtle variations in amplitude and sweetness occur (SF2; Tables 2 and 3). Borehole data indicate these seismic facies consists of fine-grained lithologies (i.e. mudstone and marlstone, e.g., unit 5; Fig. 3). Based on the seismic stratigraphy and the integration with borehole data we interpret this depositional element as fine-grained slope deposits emplaced by dilute turbidity currents or suspension setting (cf. Hadler-Jacobson et al. 2007; Oluboyo et al. 2014).

6. Tectono-stratigraphic development of intraslope minibasins

The key seismic stratigraphic units defined within the post-salt succession document the tectono-stratigraphic development of the intraslope minibasins in central deep-water Santos Basin (Fig. 4). Here, we interpret the isochron-derived thickness variations and depositional elements occurring within each unit; this allows us to understand minibasin filling history and, more specifically, to assess how syndepositional, salt-induced seafloor relief controlled deep-water sediment dispersal and sediment architecture. Based on previous regional studies (e.g., Modica and Brush, 2004; Guerra and Underhill, 2012), we infer that the dominate sediment transport direction was from N-S and NW-SE, although we recognise local diversions from this within minibasins due to syndepositional deformation.

6.1 Unit 1: Albian - Cenomanian

The Unit 1 isochron indicates this unit is extensive and displays significant thickness variations (Figs. 6a). Overall, we observe a central thinner wedge or 'tongue' of relatively thin strata, which is surrounded by areas of thicker strata (up to 350 ms, TWT) (Fig. 6a). Seismic stratigraphic and attribute analysis provide no evidence for at least seismic-scale deep-water depositional systems within Unit 1.

Based on seismic reflection and borehole data (Fig. 5), we interpret that Unit 1 represents the distal expression of the Albian-Cenomanian carbonate platform (Fig. 4c-e, 5). Thickness variations across the study area possibly reflects differences in the timing and style of salt tectonics (e.g., Jackson et al. 2015b).

6.2 Unit 2: Turonian to Mid-Campanian

Unit 2 is less extensive than Unit 1, with the main depocenters focused within proximal minibasins presently encircled by salt walls (minibasins A, C; Fig. 6b). Locally, a thick succession is observed, however, occurring landward of a salt roller within minibasin B (depocenter B1; Figs. 6b, 7a). In contrast, within the Inner Fold Belt and more distal minibasins, thinner successions occur (e.g. minibasins F-M; Fig. 6b).

In unit 2, deep-water depositional elements, such as channels and lobes, occur only within proximal thick minibasins (Fig. 7b). Low sinuosity (<1.5), narrow (<1 km wide) submarine channels enter from the north of, and are vertically stacked within, minibasin A (Fig. 7b). Channels of similar dimensions and sinuosities trend WNW in the proximal part of minibasin B and N in minibasin C, changing to NNE towards the south where they encounter the salt wall bounding the minibasins eastern margin (Fig. 7b). At the downdip mouths of some of the channels we identify lobes, with these being particularly well-developed within depocenter C1 where they correlate with SF1 in borehole 329D and are interpreted to be sandstone-rich (Fig. 7b; Table 2).

The distribution of deep-water sediments within Unit 2 was clearly controlled by salt-related deformation, with isochron, seismic attribute and borehole data indicating Turonian to Mid-Campanian, relatively coarse-grained channels only extended downdip into and were at least partly ponded within, proximal minibasins (minibasins A and northern part of minibasin B). In addition, we interpret that channels within minibasin C are now separated from their updip counterparts in depocenter B1 by a large salt wall that pierces the stratigraphic interval within which they are developed (Fig. 7)

6.3 Unit 3: Mid-Campanian to Paleocene

Overall, Unit 3 is more extensive than Unit 2, with major intraslope depocenters still present in actively subsiding proximal minibasins (minibasins A-C; Fig. 6c). More specifically, local increases in sediment thickness occur next to intra-minibasin salt rollers and thin-skinned normal faults, and along minibasin flanks associated with growing salt walls (Figs. 8a, b; 9). However, in contrast to Unit 2, significant thicknesses of strata are now preserved in downdip minibasins, especially in synclines flanking folds, above salt-cored faults, and along minibasin flanks (minibasins D-M; Fig. 6c).

Deep-water depositional systems are widespread in unit 3 (Figs. 8 c-e; 9c). Minibasins A-C are still dominated by relatively low sinuosity (<1.5), narrow (<1 km wide) submarine channels. However, these channels extend further downdip than those in Unit 2. For example, channels in minibasin A are no longer restricted to the northern part of the depocenter, now extending c. 10 km further south to the junction between minibasins A and B, where they appear to pass downslope into a lobe (Figs. 8c,d). Likewise, channels and lobes initially ponded in depocenters B1-B2 extend further downslope along minibasin B, depositing lobes in depocenter B3 (Fig. 8d). Some of the channels entering minibasin B in Unit 3 extend downslope towards minibasin C, although channels along the western flank of the minibasin appear to be diverted towards depocenter B3 at their southern end (Figs. 8d; 9 a,b). During deposition of unit 3, lobes are also deposited against the salt wall bounding the SE margin of the minibasin (depocenters C2, Figs. 8d; 9c). Continued filling of minibasin C was accompanied by the shifting of depocenters C2 to C3 related to deposition of SE-trending submarine channels, which apparently terminate abruptly against the salt wall defining the southern limit of minibasin C; however, further downslope, on the other side of this structure, channels of similar dimensions, orientation and morphology occur in minibasin D and E (Figs. 8e; 9d).

In distal regions, N-trending, slightly sinuous channels occur within and trend parallel to the long axes of several broadly N-trending minibasins (channels 1, 2 and 3 in minibasins I-K; Fig. 10). Channels that trend at a relatively high angle (>30°) to bounding salt walls and salt-cored anticlines change course within the minibasins, becoming parallel to the minibasin axis and bounding salt walls (channels 4, 5; Fig. 10). Locally, channel bends also occur next to salt-cored folds, in some cases leading to the deposition of LAPs (channel 2; Figs. 10, 11a,b). Within distal minibasins, lobes are confined to minibasin flanks and within fold-bounded synclines, downlapping onto the lows and onlapping and converging towards salt-cored highs (Figs. 12a-f).

Channel continuity between adjacent minibasins across bounding salt walls is observed downslope in distal minibasins (e.g. channel 5 across minibasins L and M; Fig. 10). However, changes in channel geometry are evident between, for example, minibasin L to M. In minibasin L, we identify an erosional channel, up to 1 km wide and, 50 m thick (Fig. 10, 13). The channel trends NW and is flanked by levees and overlying an intra-minibasin MTC (channel 5 in Figs. 13 a-d). Within minibasin M, this channel increases in reflectively, width (to 5 km) and thickness (to 200 m), in addition to bending to trend NE, sub-parallel to the minibasin axis (Figs. 13a,b,e). The asymmetric levees flanking channel 5 onlap onto and are seemingly rotated on the limbs of, the western salt-cored anticline (Fig. 14).

During deposition of Unit 3, the locus of subsidence in minibasin A shifted towards the center and eastern margin of the depocenter possibly due to welding (depocenters A1 to A3; Figs. 8b-d). In addition, the cessation of activity on landward-dipping listric faults at the northern updip end of minibasin B meant that channels were able to spill southwards and flow axially along minibasin B (depocenters B1 to B3; Figs. 8b,d and 9a,b). Continued deposition drove welding of minibasin C and shifting of the main depocenter within minibasin C, leading to eventual inversion of the minibasin stratigraphy and the formation of a turtle anticline (depocenters C2 to C3; Figs. 8a,b and 9c). Eventual filling of minibasin C resulted in sediment spilling downslope to the SE into minibasin D and E (Figs. 8e, 9d). Based on similar trends and morphology, we suggest channels presently contained in minibasins D and E, and now separated by a large diapir, were previously part of a through-going, continuous system that extended across the diapir (Figs. 8e, 9d). Likewise, we suggest that at least the northern part of the salt wall currently dividing minibasins B and C did not represent a barrier to channels flowing between these depocenters, but that subsequent growth of the diapir initially underlying the channels, subsequently dissected these depositional systems (Figs. 8c,d). Furthermore, we interpret that channels flowing across the ISPFB and the distal minibasins probably spilled over from proximal minibasins west of minibasin A, which are not imaged in the seismic dataset. Towards the distal minibasins, structurally-induced changes in channel sinuosity occurred due to coeval salt-cored highs on the paleoseafloor (Figs. 10-14). LAPs are only developed when channels are unconfined or only weekly confined, recording lateral channel migration to towards the minibasin centers (Figs. 10,11). In addition, levees and lobes are deposited confined within minibasins or in the intra-minibasin fold- and thrust-bounded synclines associated with shortening of salt and its overburden (Fig. 12-14).

6.4 Unit 4: Paleocene to Mid-Oligocene

Deposition within Unit 4 extends further east than in unit 3 (Fig. 6d). Thickness changes in Unit 4 indicate proximal thick minibasins were still activity subsiding, although deposition was now also occurring above bounding salt walls (e.g., minibasin D; Fig. 6d).

Rather than containing relatively abundant channel-levee systems and lobes like units 2 and 3, Unit 4, more specifically sub-units 4a and 4b within the proximal thick minibasins, are dominated by MTCs (Figs. 9a,b and 15a). MTCs within unit 4a contain relatively angular megaclasts that are up to 5 km long and 1 km wide overlying sub-continuous to chaotic seismic facies (Fig. 9b). In contrast, MTC blocks within unit 4b are less angular and smaller (1 km long by 500 m wide; Figs. 9a,b; 15b). In the Inner Fold Belt and within the downdip elongated minibasins, at least 200 km long, N- and NW-trending linear, sub-parallel grooves are developed along a single seismic event at the base of unit 4 (Fig. 16). These grooves are overlain by blocks that are smaller (200 m long by 100 m wide) than those observed in the proximal thick minibasins (section A-A’ in Fig. 16).

During deposition of Unit 4, some of the proximal and distal minibasins continue to actively subside into salt (Fig. 6d). However, unit 4 marks a significant change in the style of clastic sediment deposition within the basin. More specifically, we see a cessation of coarse-grained clastic deposition within channels and lobes, and the initiation of widespread MTC emplacement (Fig. 15). It is not possible to constrain the source of MTCs contained within the proximal thick minibasins, and it is thus unknown if they were derived from collapse of the distal shelf-edge or slope, or if they were locally sourced from the uplifted and rotated minibasin margins flanking the bounding diapirs. However, thrusts within unit 4a within the proximal minibasins may indicate MTCs were sourced from the NE (Fig. 9a). In contrast, the regionally extensive grooves capping the distal minibasins and ISPFB suggest MTC emplacement from the NNW (Fig. 16).

6.5 Unit 5: Mid-Oligocene to Pleistocene

Unit 5 is more extensive than underlying units, with the main minibasin depocenters still occurring in the NW of the study area (e.g., minibasin D; Fig. 6e). We identify at least three MTC-bearing sub-intervals within Unit 5, all of which are contained within a single minibasin in the W of the study area (Figs. 6e; 17). In contrast to the regionally developed, Paleocene MTC identified within Unit 3, these younger MTCs are confined by salt-cored diapirs. The lowermost MTCs are dominated by highly chaotic seismic facies and lack megaclasts, whereas the shallower MTC contains abundant megaclasts within a chaotic matrix (Fig. 17; see also Jackson et al., 2011).

Because these MTCs extend to the NW outside of the seismic dataset, their source is unknown. However, regional considerations suggest they were sourced from large shelf-edge and slope failures north or north-west of the study area (Contreras et al., 2010; Jackson, 2011). Therefore, Unit 5 records Neogene emplacement of several MTCs in response to repeated collapse of the north-western basin margin shelf-edge and/or slope.

7. Discussion

We used 3D seismic reflection and borehole data to illustrate the spatial and temporal variations in the size and type of salt-influenced deep-water depositional systems, Santos Basin, offshore Brazil. We here discuss regional salt-tectonic controls on minibasin development, and the key local controls on paleo-seafloor relief and how this influenced deep-water stratigraphic architecture.

7.1. Salt-related controls on the tectono-stratigraphic evolution of the Santos Basin

We show that the initial phase (Turonian to Mid Campanian; unit 2) of coarse clastic deposition was restricted to the north, with submarine channels and lobes confined within proximal minibasin depocenters (minibasins A and C, Fig. 7 a, b). Intra-minibasin relief was generated by salt diapirs and landward-dipping, salt-detached listric faults (Fig. 9 a, b). The main phase of clastic deposition occurred during the Maastrichtian to Paleocene (unit 3), during which time salt- and fault-related accommodation in the proximal minibasins was filled or 'healed', allowing deep-water sediment to bypass the now-filled proximal minibasins and to be deposited further downslope (minibasins C, D and E; Figs. 8e 9). Furthermore, eventual welding of proximal led to the formation of a turtle anticline and a lateral shift of the related depocenters from the minibasin centre towards the immediate flanks of the bounding diapirs (minibasin C, Fig. 8b, 9c). During the third and final phase of clastic deposition (unit 4;

Paleocene to mid-Oligocene), MTCs dominated, being sourced from either the flanks of intraslope minibasins, or the shelf-edge and/or slope. Channels and lobes are very rare in this stratigraphic interval, suggesting a regionally significant change in sediment supply occurred between the Paleocene (late Unit 3) and Eocene (early Unit 4) (Figs. 15, 16). This abrupt change in deep-water deposition may have been driven by river capture and diversion of sediment supply towards the northern Santos and the Campos Basin, a process that has been attributed to the uplift of the onshore coastal mountain range (e.g. Cobbold et al. 2001). Localised salt flow and minibasin subsidence continued during a fifth and final phase (unit 5; mid-Oligocene to present-day). Deposition at this time was dominated by suspension settling of relatively fine-grained deposits, although MTCs provide evidence for continued failure of the shelf-edge and/or slope (Fig. 17).

Previous regional studies in the Santos Basin assume that most coarse clastic sediment was trapped behind a large (4 km thick, 200 km long, 10 km wide), salt-controlled, intra-slope depocenter (i.e., the Albian Gap; e.g, Ge et al., 1997; Modica and Brush, 2004; Guerra and Underhill, 2012; Jackson et al., 2015a). However, our study provides conclusive evidence that relatively coarse-grained deep-water depositional elements were deposited up to 200 km from the Late Cretaceous shelf margin, clearly indicating that not all coarse-grained sediment was trapped landward of the Albian Gap (cf. Modica and Brush, 2004; Guerra and Underhill, 2012).

7.2. Beyond the ‘fill and spill’ model

The two initial phases of sediment deposition, first in proximal locations (Unit 2) and then reaching further downslope along a healed slope (Unit 3), indicate progressive basinward filling or 'healing' of this salt-influenced slope (Fig 18). The stratigraphic development of the deep-water central Santos Basin thus displays many of the characteristics captured in the 'fill and spill' model (e.g. Winker, 1996; Prather et al., 1998). Furthermore, our results show that spilling between minibasins tends to occur in locations where salt-cored structures trend perpendicular to sediment transport, with long-distance confinement characterising locations where salt walls are oriented parallel or at a low angle to sediment transport (e.g., Booth et al., 2003; Oluboyo et al., 2014). More specifically, we document local sediment spilling due to minibasin welding and the associated formation of turtle anticlines; these two processes together cause diversion of deep-water channels towards the downslope minibasin (e.g.; Fig. 8b, Fig 18).

A key result of this work is that post-depositional growth of salt diapirs can cause dissection of previously through-going depositional systems, resulting in 'pseudo-onlap' onto the diapir flanks (e.g., salt wall between D and E, Figs. 8e, 9d, 18). This process has perhaps been overlooked in previous studies focusing on relatively young (i.e. Neogene-Quaternary), near-seabed stratigraphy because in these cases, despite being influenced by syn-depositional salt movement, the deposition systems of interest presently still overlie or occur on the flanks of large salt bodies (e.g. Pirmez et al., 2000; Fonnesu, 2003; Gee and Gawthorpe, 2006, 2007). This highlights an important, perhaps ignored aspect of the fill-and-spill model, namely that the depositional substrate, be it salt or mudstone, is not static (e.g. Winker, 1996; Prather et al., 1998); instead, this substrate is highly mobile, with related structures continuing to grow post-deposition of any one stratigraphic interval. This has obvious implications for the formation of hydrocarbon traps (see below).

Finally, this study illustrates that the pattern of minibasin filling is influenced by the formation and growth of intra-minibasin salt-cored faults and salt rollers (Fig. 8 a; 9 a,b; 18). More specifically, growing intra-minibasin structures can lead to somewhat counterintuitive depositional patterns; for example, deepwater systems may be diverted away from proximal minibasins, meaning that distal minibasins are filled first, contrary to the classical 'fill and spill' model (Fig 18; e.g. Booth et al., 2003; Hudec et al., 2009; Jackson et al., 2010; Albertão et al., 2011; Oluboyo et al., 2014).

7.3. Impact of salt-induced seafloor relief on reservoir distribution and architecture

Having discussed the regional controls on basin-scale deep-water stratigraphic architecture, we now consider the local controls on syndepositional seafloor relief and sediment dispersal and architecture. In addition, we discuss the implications of our findings for the overall salt-tectonic evolution of the Santos Basin. Local seafloor relief can lead to lateral confinement, frontal confinement or blocking), deflection and diversion of deep-water depositional systems; thus, directly impacting reservoir distribution and architecture along slopes (e.g. Booth et al., 2003; Adeogba et al., 2005; Gee and Gawthorpe, 2006; Deptuck et al., 2007; Clark and Cartwright 2009; Hubbard et al., 2009; Callec et al., 2010; Mayall et al., 2010; Oluboyo et al., 2014; Spychala et al., 2017; Doughty-Jones et al., 2017).

In the salt-influenced Santos Basin, we observe the following end-member styles of salt-sediment interaction: (i) local *diversion* of channels by pre-existing seafloor relief, which also results in a change in channel sinuosity (e.g., Figs. 13, 18) (cf. Oluboyo et al., 2014, Doughty-

Jones et al., 2017); (ii) *deflection* of channels towards syn-depositional structural lows, leading to channel lateral migration from and stacking adjacent to, emerging salt-cored highs (e.g., Figs. 11a, 12, 18); (iii) *confinement* of channels by adjacent salt-cored highs resulting in channel stacking and levee growth, and lobe deposition in parts of the system that are frontally confined (e.g., Figs. 12); (iv) *blocking* of channels by intra-minibasin salt rollers and salt-detached faults, preventing deposition downslope (e.g.; Figs. 7, 8, 18) (cf. Clark and Cartwright 2009; 2011). Two key questions we address below are; (i) were salt-cored highs static or actively growing *during* the entire life-cycle of the depositional elements?; and (ii) did the structures continue to grow *after* the channels and lobes were deposited?

Local channel *deflection* is evident in the south of the study area, occurring next to emerging shortening-related, salt-cored buckle folds and thrust-cored folds (Figs. 10; 11a; 12; 18). Likewise, channel *diversion* also occurs to in the south of the study area, next to a salt wall (minibasin M, Fig. 13), as well as within the proximal minibasins (minibasins B, C, Fig. 8 d). The salt-cored highs next to which channel *deflection* and *diversion* are observed are oriented nearly-perpendicular to the depositional slope. The structurally-induced sinuous geometry of the channels adjacent to these highs clearly suggest the latter grew *before* Late Maastrichtian/Paleocene submarine channels propagated downslope and across the São Paulo Plateau. Syndepositional growth of salt-cored highs is supported by the following evidence: (i) onlap and thinning towards the coeval highs (Figs. 12, 14); (ii) local stacking/ponding in the thrust-cored syncline (minibasin J; Figs. 12e, 18); and (iii) uplift, tilting and rotation of levee towards the channel axis (sensu Clark and Cartwright, 2009; minibasin M; Fig. 14). Salt structure growth may have also continued *after* deposition, as indicated by the channel tilting and uplift (Fig. 14).

Our data provide evidence for channel *blocking* and *confinement* (e.g., within proximal minibasins B, Figs. 9 a,b; 18). For example, channels and lobes initially confined north of minibasin B (depocenters B1, B2) or diverted towards minibasin C, eventually extended along minibasin B before being frontally confined against a salt wall at the southern end of the minibasin (depocenters B3; Fig. 8d). We suggest local increases in accommodation during minibasin confinement leads to: (i) an increase in channel width and thickness along the minibasin axis, with a corresponding increase in seismic amplitude also suggesting a downslope increase in sandstone deposition (e.g., Fig. 14) (cf. Gee and Gawthorpe, 2006); (ii) preferential deposition of levees where accommodation locally increases (minibasins L, M, Figs. 13, 14); (iii) preferential deposition of (confined) lobes (and healing of syn-depositional relief) in synclines between intra-minibasin salt-cored anticlines (Figs. 12, 18). We suggest synsedimentary growth of the salt-cored structures bounding the folded minibasins in the contractional domain provided confined accommodation, causing channels to aggrade and triggering deposition of related levees and lobes.

These observations have implications for the salt-related structural evolution of the central deep-water Santos Basin. We propose that the seafloor salt-cored folds were the expression of Late Cretaceous-to-Paleocene, synsedimentary, thin-skinned shortening, resulting from downslope flow of salt and its overburden, possibly related to the formation of the Albian Gap (Jackson et al. 2015a; Pichel et al. 2018). The distribution and architecture of synkinematic channels and levees systems provide a stratigraphic record of this structural growth (Fig. 18).

7.4 Exploration significance

We propose that the salt-related controls observed in the central deep-water Santos Basin led to changes in the geometry, distribution and potential structural and stratigraphic trapping of reservoir-prone units. As such, post-salt sequences in this part of the Santos Basin may be prospective (see Fainstein et al., 2001). In particular, we have illustrated the presence of: (i) fault-block traps (e.g., Figs. 9 a,b); (ii) turtle anticlines (minibasin C, Fig. 9 c); (iii) stratigraphic traps related to the pinch-out of channels and lobes towards salt-cored highs (e.g., Figs. 9 a,b; 14). Potential reservoir-prone units include channel-fill, lobes and, possibly, levees, whereas 'background' deposits, such as slope mudstone, and salt represent the main seals (Table 3). Mudstone-rich MTCs may also form lateral and vertical seals (e.g., minibasin L, Fig. 15). The seismic stratigraphic geometry and distribution of the more proximal reservoir-prone intervals of stacked submarine channels and fans or sheet-sand reservoirs illustrated in this study are strikingly similar to reservoir-prone units being currently produced in the Gulf of Mexico (i.e., Auger Basin, Booth et al., 2003; Jackson and Hudec, 2017; Fig. 9 a, b).

The deep-water depositional systems we have identified in the Santos Basin could be distal analogues of the unconfined turbidites in the Merluza (Turonian) (e.g., Enciso and Tisi, 1998), and Roncador fields (Campanian-Maastrichtian), Campos Basin (e.g., Bruhn et al., 2003; Hongquan et al., 2018). Unlike those further north, the distal deep-water depositional systems in the Santos Basin have been confined axially for more than 150 km and because of this confinement, it is possible the associated reservoirs are thicker than those developed in the Campos Basin (cf. Gulf of Mexico; e.g., Booth et al., 2003). Furthermore, the play fairway, in terms of reservoir distribution, will likely be narrower due to syn-depositional confinement of the deep-water depositional systems. A key exploration risk for the whole Santos Basin is migration, principally due to the presence of thick, likely very low-permeability salt between sub-salt source rocks and supra-salt reservoirs. This is a particular risk in distal areas, where thick allochthonous salt remains, whereas in proximal areas salt welds may facilitate the vertical migration of hydrocarbon. Even if hydrocarbons migrate through weld, the mudstone-dominated nature of many of the minibasin may still pose a migration risk.

Shallowly buried MTCs may represent drilling hazards due to unpredictable pore pressures and hole conditions. In addition, syn-emplacement erosion at the base of salt diapir-flank MTCs may have locally removed underlying submarine channel reservoirs and compromise reservoir continuity (e.g.., minibasin K; Fig. 13c).

8 Conclusions

Our 3D seismic reflection and borehole-based analysis illustrates a long timescale (ca. 60 Myrs) record of salt-sediment interaction in more than ten minibasins covering an area of c. 20,122 km^2; thus, documents the post-salt tectonostratigraphic evolution of the central deep-water Santos Basin from the initial minibasin development in the Turonian up to present-day:

1. Overall, we recognise three minibasin types, from proximal updip to distal location downdip; i.e. (i) proximal thick minibasins, apparently welded, (ii) medial shallow minibasins, overlying thick salt, and (iii) distal elongated minibasins deformed by shortening-related folds and thrusts

2. Four main types of deep-water sediment depositional elements were deposited within the minibasins in central deep-water Santos Basin: channels, levees, lobes, MTCs and background deposits.

3. Borehole information indicates that the minibasin-confined channel-levee systems are composed of interbedded sandstone, siltstone and mudstone. Whereas distal boreholes suggest siltstone rich channel-fill and lobes.

4. Sedimentation in central deep-water Santos Basin occurred during three main phases of minibasin subsidence:

- Phase I: Turonian to the Mid-Campanian: sand-rich channel systems and lobes were confined within proximal updip minibasins and to the hangingwalls of landward-dipping, salt-detached listric faults.

- Phase II-Mid-Campanian to the Paleocene: sand-rich channels and lobes eventually filled and bypassed proximal updip minibasins, with coarse clastic deposition then occurring further downslope in distal minibasins, >100 km from the coeval shelf margin.

- Phase III and IV: Paleocene-to-middle Oligocene: continued rise of proximal salt walls dissected previously deposited deep-water systems, with deposition from diapir- and shelf-edge sourced MTCs becoming increasingly important

5. Syndepositional seafloor relief, driven by passive and active diapirism, and salt-detached thrusting and folding, caused changes in the geometry, architecture and distribution of deep-water depositional systems:

i) channel deflection and diversion around salt-cored highs

ii) channel and levee uplift and rotation on the flanks of rising salt-cored anticlines and diapirs

iii) progressive lateral channel migration, expressed in the form of lateral accretion packages (LAPs)

iv) Lateral and frontal confinement of channel, levees and lobes.

v) channel width and thickness increase due to lateral confinement

6. The deep-water depositional elements identified have important implications for post-salt hydrocarbon prospectivity in the central, deep-water Santos Basin, with a range of reservoir types and trapping styles being developed in this previously underexplored interval

ACKNOWLEDGEMENTS

We would like to thank CGG for providing access to the 3D seismic data and for granting permission to publish the results of this study. We also thank Statoil and ANP Brazil for providing access to the borehole data. Schlumberger WesternGeco is also gratefully acknowledged for providing 2D seismic regional data, partial funding and support of this work. We thank reviewers David Hodgson, Jory Pacht and Ian Clark and editor Barry Katz for their suggestions which have significantly improved the quality of this manuscript. We also acknowledge Rachelle Kernen for her insightful suggestions.

FIGURE CAPTIONS

FIGURE 1: (a) Offshore Brazil sedimentary basins; (b) Santos Basin topography and bathymetry map highlighting the location of study area and dataset. 3D seismic reflection

data courtesy of CGG and public Brazilian boreholes; (c) Geoseismic profile across the study area based on interpretation of 2D seismic data courtesy of WesternGeco, Schlumberger. See location in b; (d) Seismic stratigraphic framework. After Modica and Brush (2004); Moreira et al. (2007); Jackson (2012).

FIGURE 2: Central deepwater Santos Basin paleogeography highlighting sedimentation trapped or ponded landwards of the Albian Gap with limited deposition in the area of study. Modified after Modica and Brush, 2004. (a) Late Campanian paleogeography; (b) Middle Eocene paleogeography; (c) Late Eocene paleogeography.

FIGURE 3: Intra-minibasin seismic-well correlation. Key seismic horizons and units are indicated and defining a turtle anticline due to inversion of the minibasin stratigraphy. Seismic attributes response highlights vertical variations in seismic facies within the minibasin. See also Table 2 for a description of SF1, SF2, and SF3. Dominant frequency and vertical seismic resolution decreases with depth, as indicated in the last three columns and in Table 1. Borehole location is shown in Figure 4a

FIGURE 4: 4a) Postsalt isopach (Seabed to top salt depth thickness map) illustrating sediment thickness variations across the study area. Depth thickness map estimated using the depth-converted seafloor depth structural map and the top salt structural map also in depth. 4b) Top salt structural map illustrating the main minibasin types in the study area. Proximal minibasins (A-E); shallow minibasins (F-H) and distal elongated minibasins (I-M). 4c) Geoseismic profile across the proximal thick minibasins A to E. 4d) Geoseismic profile across shallow minibasins F-H. 4e) Geoseismic profile across part of the inner fold belt and across some of the distal elongated minibasins (K-M). See Figure 4b for location of geoseismic profiles.

FIGURE 5: Intra-minibasin seismic-well tie showing the presence of reservoir-prone sandstones in distal locations, i.e., > 50 km from the coeval shelf margin. (a) Borehole 369a penetrates a medial shallow minibasin. See Figure 4a for location. (b) Borehole 723C penetrates the flank of a downdip distal minibasin. See Figure 4a for location.

FIGURE 6: Regional isochrons illustrating deposition and salt-related deformation in the post-salt of central deep-water Santos Basin. 6a) Albian-Cenomanian unit 1 twt thickness map; 6b) Turonian to Mid-Campanian Unit 2 twt thickness map; 6c) Mid-Campanian to Paleocene Unit 3 twt thickness map; 6d) Paleocene to Mid Oligocene Unit 4 twt thickness map; 6e) Mid-Oligocene to present-day Unit 5 twt thickness map.

FIGURE 7: Detailed thickness maps and attributes of the proximal minibasins (A-C) illustrating local intra-minibasins depocenters and shifting of depocenters during minibasin development. (a) Unit 2 thickness map highlighting initial depocenters A1, B1 and C1 within updip proximal minibasins A, B and C. Present-day Top Salt is shown in pink. (b) Unit 2b seismic attributes blending (interval is shown on section in Figure 9c). Present-day Top Salt structure map is shown in pink. Attributes visually blended correspond to Variance and Sweetness (described in the Methods section). Purple colours correspond to more transparent background facies. Yellow to red colours highlight deep-water depositional elements interpreted in the accompanying map. Depocenters A1, B1 and C1 are interpreted based on thickness map in Figure 7a.

FIGURE 8: Detailed thickness maps and attributes of the proximal minibasins (A-C) illustrating local intra-minibasins depocenters and shifting of depocenters during minibasin

development. Visually blended seismic attributes correspond to Variance and Sweetness described in the Methods section. Purple and dark blue colours correspond to more transparent background facies. Yellow to red colours highlight deep-water depositional systems interpreted in the accompanying map. Depocenters are interpreted based on the isochrons. (a) Proximal thick minibasins - Sub-Unit 3a isochron highlighting shifting of depocenters A1, B1, C1 (Fig. 7a) to new depocenters A2, B2 and C2. Present-day Top Salt is shown in pink. (b) Proximal thick minibasins - Sub-Unit 3b isochron highlighting shifting of depocenters A2, B2 and C2 (Fig 8a) to new depocenters A3, B3 and C3. (c) Sub-unit 3a seismic attributes blending and interpretation. Sub-unit 3a is shown on sections in Figures 9a, b and c. (Fig. 8a). (d) Sub-unit 3b seismic attributes blending and interpretation. Sub-unit 3b is shown on sections in Figures 9a, b and c. (e) Unit 3b sweetness and variance attribute visual blending illustrating the post-depositional dissection of submarine clastic systems caused by the rise of the salt wall presently bounding minibasins B and C, C and D and D and E.

FIGURE 9: Seismic profiles along and across the updip/proximal minibasins illustrating the key horizons and units mapped and the thickness and seismic facies variations defining the minibasin stratigraphy. Highly-reflective intervals correspond to interpreted depositional elements highlighted with seismic attributes in Figure 8. The locations of the seismic sections are also shown on Figure 8. (a) Seismic section along Minibasin B. Insets illustrate potential sandstone-rich depositional elements with an amplitude- and frequency-based seismic attribute (Sweetness). (b) Laterally and frontally confined deep-water depositional elements along minibasin B based on seismic stratigraphic interpretation and seismic attribute analysis. (c) Seismic profile across Minibasin C illustrating the main units interpreted. Initial confinement is illustrated by thinning and onlapping of minibasin stratigraphy towards the

downdip (SE) salt wall (units 2a, 2b and 3a). Minibasin filling and welding led to inversion of the minibasin stratigraphy (units 2a, 2b, and 3a), and spilling and shifting of the initial depocenters from Minibasin B towards the SE and downdip minibasins (units 3b and 4). See location of seismic profile in Figure 8

FIGURE 10: Deep-water depositional systems and distal downdip minibasins (I, M) in the Inner São Paulo Fold Belt and the São Paulo Plateau. Updip, channel systems are relatively linear and unconfined. Local variations in architecture are controlled by salt-cored folds and anticlines and salt walls. Lateral and frontal confinements is observed downdip. See area location in Figure 6c. Interpretation is based on seismic stratigraphy, geomorphology, seismic attributes and thickness maps. Detailed isochrons, attribute maps, and seismic sections are shown in Figures 11-14.

FIGURE 11: (a) Sweetness and variance blending illustrating local increase in channel sinuosity and lateral accretion packages described in Table 3. See channel 2 location and associated structural elements in Figure 10. (b) Seismic section illustrating channel bend and high-amplitude lateral accretion packages. See Figure 11a for location of seismic section.

FIGURE 12: Isochron (a) and seismic attribute blending (b) for unit 3 covering minibasins I and J illustrating salt-related controls on coeval deep-water depositional systems. Increase in thickness occurs around salt-cored folds and associated to lobes deposition where frontally confined. Deflection of submarine channel 2 (ch2) occurs around a salt-cored fold in Minibasin J and this is highlighted in the amplitude contrast attribute in the inset. See interpretation and location in Figure 10. (c) and (d): Seismic sections across the distal part of minibasin I, illustrating lobes deposition and confinement. (e) and (f) Seismic sections across and along

minibasin J. illustrating salt-related controls on deposition. Location of seismic sections are highlighted in Figures 12 a and b

FIGURE 13: Isochron (a) and seismic attribute blending (b) for unit 3 covering minibasin L and M illustrating deep-water submarine channels across present-day minibasins and salt-related controls. Channel 5 (ch5) is oriented SE and relatively thinner along Minibasin L but gets diverted and laterally confined and wider along Minibasin M due to the bounding salt-wall oriented nearly-perpendicular to the slope. See location and interpretation in Figure 10. (c) A local MTC underlies submarine channel 5 within Minibasin L. Seismic sections in (d) and (e) highlight bounding salt walls and salt-cored anticline, channel 5 and associated levees in minibasins L and M. See location of seismic sections in Figures 13 a and b.

FIGURE 14: Submarine channel and levee geometry variations along Minibasin M. Isochron and section A-A’ illustrate wing-shaped levees developed adjacent to the channel. Seismic attribute and sections illustrate that high-amplitudes are restricted to the channel axis, whereas the levees are characterized by medium to low amplitudes. Channel onlaps and its apparently tilted and rotated where it gets diverted and closer to the bounding salt wall (section B-B’). Intra-levee reflections are rotated towards the channel axis (sections C-C’ and D-D’) indicating salt movement during deposition

FIGURE 15: Seismic attributes sweetness and variance blending and interpretation of intra-minibasin clasts characterizing MTCs in proximal updip minibasins during deposition of Unit 4. See location of minibasins A, B and C in regional map Figure 6c and seismic and geoseismic sections in Figures 9a and 9b.

FIGURE 16: Seismic attributes and seismic sections illustrating linear grooves characterizing regional-scale MTCs across the São Paulo inner fold-belt and the São Paulo plateau and highlighting a drastic change in the evolution of the central deep-water Santos Basin during deposition of Unit 4. See location of minibasins J, K, L, and M in regional map in Figure 6c.

FIGURE 17: Seismic expression of MTCs within Unit 5. a) Amplitude contrast attribute of intra-Unit 5 horizon highlighting clasts and a chaotic matrix; b) seismic section across the minibasin; c) seismic section along the minibasin.

FIGURE 18: a) Block diagram summarizing sedimentation within proximal minibasins: Ponding occurs within proximal, updip, intra-minibasin depocenters prior to spilling and deposition along the minibasins (1). Filling of minibasins and subsequent welding of minibasin floor led to spilling towards downdip minibasins (2). Channel systems are post-depositionally dissected by rising salt walls bounding the present-day minibasins (3). Subsequent spilling from updip depocenters and diversion by rising salt walls led to deposition in downdip depocenters (4). b) Block diagram summarizing salt-related controls in deep-water sedimentation across part of the São Paulo inner fold-belt and the distal minibasins in the São Paulo plateau. Channel systems spilling from the proximal minibasins are relatively linear updip and away from salt-cored structures (1). Local controls in channel system architecture (2) and sediment distribution (3) are observed. Present-day salt walls dissected channel systems similarly to what it is observed in the updip minibasins (4). The architecture of channel systems varies between adjacent minibasins controlled by the presence of intra-minibasin MTCs and confinement (5 and 6).

TABLE CAPTIONS

Table 1: Vertical seismic resolution of key intervals in different structural domains

Table 2: Table 2: Seismic facies interpretation and seismic attributes calibration with lithology from borehole 329D, minibasin C. See Figure 4a for location

Table 3: Seismic facies and depositional elements identified within the post-salt in central deep-water Santos Basin. Depositional elements are defined based on the integration of seismic stratigraphy and seismic geomorphology.

REFERENCES

Abreu, V., M. Sullivan, C. Pirmez, and D. Mohrig, 2003, Lateral accretion packages (LAPs): an important reservoir element in deep water sinuous channels: Marine and Petroleum Geology, v. 20, p. 631-648.

Adeogba, A.A., McHargue, T.R. and Graham, S.A., 2005. Transient fan architecture and depositional controls from near-surface 3-D seismic data, Niger Delta continental slope. AAPG bulletin, 89(5), pp.627-643.

Albertão, G. A., T. Mulder, and R. Eschard, 2011, Impact of salt-related palaeotopography on the distribution of turbidite reservoirs: Evidence from well-seismic analyzes and structural restorations in the Brazilian offshore: Marine and Petroleum Geology, v. 28, p. 1023-1046.

Alves, T. M., J. Cartwright, and R. J. Davies, 2009, Faulting of salt-withdrawal basins during early halokinesis: Effects on the Paleogene Rio Doce Canyon system (Espírito Santo Basin, Brazil): AAPG Bulletin, v. 93, p. 617-652.

Anderson, J. E., J. Cartwright, S. J. Drysdall, and N. Vivian, 2000, Controls on turbidite sand deposition during gravity-driven extension of a passive margin: examples from Miocene sediments in Block 4, Angola: Marine and Petroleum Geology, v. 17, p. 1165-1203.

Argent, J.D., Stewart, S.A. and Underhill, J.R., 2000. Controls on the Lower Cretaceous Punt Sandstone Member, a massive deep-water clastic deposystem, Inner Moray Firth, UK North Sea. Petroleum Geoscience, 6(3), pp.275-285.

Arnott, R.W.C., 2007. Stratal architecture and origin of lateral accretion deposits (LADs) and conterminuous inner-bank levee deposits in a base-of-slope sinuous channel, lower Isaac Formation (Neoproterozoic), East-Central British Columbia, Canada. Marine and Petroleum Geology, 24(6-9), pp.515-528.

Bacoccoli, G., R. G. Morales, and P. J. M. De Castro, 1979, Oil Exploration in Campos Basin, Brazil; Model for Exploration in Atlantic-Type Basins: ABSTRACT, 412-412 p.

Bacoccoli, G., R. G. Morales, and O. A. Campos, 1980, The Namorado oil field: A major oil discovery in the Campos basin, Brazil.

Badalini, G., Kneller, B. and Winker, C.D., 2000, Architecture and processes in the late Pleistocene Brazos-Trinity turbidite system, Gulf of Mexico continental slope. In Deep-Water Reservoirs of the World: SEPM, Gulf Coast Section, 20th Annual Research Conference, pp. 16-34.

Beaubouef, R.T. and Friedmann, S.J., 2000, December. High resolution seismic/sequence stratigraphic framework for the evolution of Pleistocene intra slope basins, western Gulf of Mexico: depositional models and reservoir analogs. In Deep-water reservoirs of the world: Gulf Coast Section SEPM 20th Annual Research Conference (pp. 40-60).

Babonneau, N., Savoye, B., Cremer, M. and Bez, M., 2010. Sedimentary architecture in meanders of a submarine channel: detailed study of the present Congo turbidite channel (Zaiango project). Journal of Sedimentary Research, 80(10), pp.852-866.

Booth, J. R., M. C. Dean, A. E. DuVernay, and M. J. Styzen, 2003, Paleo-bathymetric controls on the stratigraphic architecture and reservoir development of confined fans in the Auger Basin: central Gulf of Mexico slope: Marine and Petroleum Geology, v. 20, p. 563-586.

Broucke, O., F. Temple, D. Rouby, C. Robin, S. Calassou, T. Nalpas, and F. Guillocheau, 2004, The role of deformation processes on the geometry of mud-dominated turbiditic systems, Oligocene and Lower–Middle Miocene of the Lower Congo basin (West African Margin): Marine and Petroleum Geology, v. 21, p. 327-348.

Bruhn, C. H., and R. G. Walker, 1995, High-resolution stratigraphy and sedimentary evolution of coarse-grained canyon-filling turbidites from the Upper Cretaceous transgressive megasequence, Campos Basin, offshore Brazil: Journal of Sedimentary Research, v. 65.

Bruhn, C. H., J. A. T. Gomes, C. Del Lucchese Jr, and P. R. Johann, 2003, Campos basin: reservoir characterization and management-Historical overview and future challenges: Offshore Technology Conference.

Brun, J.-P., and X. Fort, 2004, Compressional salt tectonics (Angolan margin): Tectonophysics, v. 382, p. 129-150.

Callec, Y., Deville, E., Desaubliaux, G., Griboulard, R., Huyghe, P., Mascle, A., Mascle, G., Noble, M., Padron de Carillo, C. and Schmitz, J., 2010. The Orinoco turbidite system: Tectonic controls on sea-floor morphology and sedimentation. AAPG bulletin, 94(6), pp.869-887.

Candido, A., and C. A. Cora, 1992, The Marlstoneim and Albacora Giant Fields, Campos Basin, Offshore Brazil: Chapter 8.

Clark, I. R., and J. A. Cartwright, 2009, Interactions between submarine channel systems and deformation in deep-water fold belts: Examples from the Levant Basin, Eastern Mediterranean Sea: Marine and Petroleum Geology, v. 26, p. 1465-1482.

Clark, I. R., and J. A. Cartwright, 2011, Key controls on submarine channel development in structurally active settings: Marine and Petroleum Geology, v. 28, p. 1333-1349.

Cobbold, P. R., K. E. Meisling, and V. S. Mount, 2001, Reactivation of an Obliquely Rifted Margin, Campos and Santos Basins, Southeastern Brazil: AAPG Bulletin, v. 85, p. 1925-1944.

Contreras, J., R. Zühlke, S. Bowman, and T. Bechstädt, 2010, Seismic stratigraphy and subsidence analysis of the southern Brazilian margin (Campos, Santos and Pelotas basins): Marine and Petroleum Geology, v. 27, p. 1952-1980.

Davison, I., 2007, Geology and tectonics of the South Atlantic Brazilian salt basins: Geological Society, London, Special Publications, v. 272, p. 345-359.

Davison, I., L. Anderson, and P. Nuttall, 2012, Salt deposition, loading and gravity drainage in the Campos and Santos salt basins: Geological Society, London, Special Publications, v. 363, p. 159-174.

Deptuck, M.E., Sylvester, Z., Pirmez, C. and O'Byrne, C., 2007. Migration–aggradation history and 3-D seismic geomorphology of submarine channels in the Pleistocene Benin-major Canyon, western Niger Delta slope. Marine and Petroleum Geology, 24(6-9), pp.406-433.

De Gasperi, A., and O. Catuneanu, 2014, Sequence stratigraphy of the Eocene turbidite reservoirs in Albacora field, Campos Basin, offshore Brazil: AAPG bulletin, v. 98, p. 279-313.

Doughty-Jones, G., Mayall, M. and Lonergan, L., 2017. Stratigraphy, facies and evolution of deep-water lobe complexes within a salt-controlled intra-slope minibasin. AAPG Bulletin, (20,170,215).

Duval, B., Cramez, C. and Jackson, M.P.A., 1992. Raft tectonics in the Kwanza basin, Angola. Marine and Petroleum Geology, 9(4), pp.389-404.

Dykstra, M. and Kneller, B., 2009. Lateral accretion in a deep-marine channel complex: implications for channellized flow processes in turbidity currents. Sedimentology, 56(5), pp.1411-1432.

Fainstein, R., Jamieson, G., Hannan, A., Biles, N., Krueger, A. and Shelander, D., 2001, October. Offshore Brazil Santos Basin exploration potential from recently acquired seismic data. In 7th International Congress of the Brazilian Geophysical Society.

Fiduk, J. C., and M. G. Rowan, 2012, Analysis of folding and deformation within layered evaporites in Blocks BM-S-8 & -9, Santos Basin, Brazil: Geological Society, London, Special Publications, v. 363, p. 471-487.

Figueiredo, A., M. Pereira, W. Mohriak, P. Gaglianone, and L. Trinidade, 1985, Salt Tectonics and Oil Accumulation in Campos Basin, Offshore Brazil: ABSTRACT: AAPG Bulletin, v. 69, p. 255-255.

Fonnesu, F., 2003, 3D seismic images of a low-sinuosity slope channel and related depositional lobe (West Africa deep-offshore): Marine and Petroleum Geology, v. 20, p. 615-629.

Fort, X., J.-P. Brun, and F. Chauvel, 2004, Salt tectonics on the Angolan margin, synsedimentary deformation processes: AAPG Bulletin, v. 88, p. 1523-1544.

Gamboa, D., T. Alves, J. Cartwright, and P. Terrinha, 2010, MTD distribution on a ‘passive’continental margin: the Espírito Santo Basin (SE Brazil) during the Palaeogene: Marine and Petroleum Geology, v. 27, p. 1311-1324.

Gambôa, L. A. P., M. A. P. Machado, D. P. Silveira, J. T. R. De Freitas, and S. R. P. Da Silva, 2008, Evaporitos estratificados no Atlantico Sul: Interpretacao sismica e controle tectono-estratigrafino na Bacia de Santos.: In Mohriak, W., Szatmari, P. & Anjos, S.M.C. Sal: Geologia e Tectonica, Exemplos nas Basicas Brasileiras., v. Beca Edicoes Ltda, Sao Paulo, Brasil, p. 340-359.

Ge, H., Jackson, M.P. and Vendeville, B.C., 1997. Kinematics and dynamics of salt tectonics driven by progradation. AAPG bulletin, 81(3), pp.398-423.

Gee, M., and R. Gawthorpe, 2006, Submarine channels controlled by salt tectonics: Examples from 3D seismic data offshore Angola: Marine and Petroleum Geology, v. 23, p. 443-458.

Gee, M., and R. Gawthorpe, 2007, Early evolution of submarine channels offshore Angola revealed by three-dimensional seismic data: Geological Society, London, Special Publications, v. 277, p. 223-235.

Gee, M., R. Gawthorpe, and S. Friedmann, 2006, Triggering and evolution of a giant submarine landslide, offshore Angola, revealed by 3D seismic stratigraphy and geomorphology: Journal of Sedimentary Research, v. 76, p. 9-19.

Giles, K. A., and M. G. Rowan, 2012, Concepts in halokinetic-sequence deformation and stratigraphy: Geological Society, London, Special Publications, v. 363, p. 7-31.

Goteti, R., S. J. Ings, and C. Beaumont, 2012, Development of salt minibasins initiated by sedimentary topographic relief: Earth and Planetary Science Letters, v. 339, p. 103-116.

Guardado, L. R., L. A. Gamboa, and C. F. Lucchesi, 1989, Petroleum Geology of the Campos Basin, Brazil, a Model for a producing atlantic type basin: part 1. Guardado, L., A. Spadini, J. Brandão, and M. Mello, 2000, AAPG Memoir 73, Chapter 22: Petroleum System of the Campos Basin, Brazil.

Guerra, M. C. M., and J. R. Underhill, 2012, Role of halokinesis in controlling structural styles and sediment dispersal in the Santos Basin, offshore Brazil: Geological Society, London, Special Publications, v. 363, p. 175-206.

Hadler-Jacobsen, F., M. H. Gardner, and J. M. Borer, 2007, Seismic stratigraphic and geomorphic analysis of deep-marine deposition along the West African continental margin: Geological Society, London, Special Publications, v. 277, p. 47-84.

Hansen, L., Janocko, M., Kane, I. and Kneller, B., 2017. Submarine channel evolution, terrace development, and preservation of intra-channel thin-bedded turbidites: Mahin and Avon channels, offshore Nigeria. Marine Geology, 383, pp.146-167.

Hart, B., 2008, Stratigraphically significant attributes: The Leading Edge, v. 27, p. 320-324.

Hearon IV, T. E., M. G. Rowan, K. A. Giles, and W. H. Hart, 2014, Halokinetic deformation adjacent to the deep-water Auger diapir, Garden Banks 470, northern Gulf of Mexico: Testing the applicability of an outcrop-based model using subsurface data: Interpretation, v. 2, p. SM57-SM76.

Hongquan, K.A.N.G., Jinluo, M.E.N.G., Cheng, T., Huaicun, J.I.A., Bo, B.A.I. and Minggang, L.I., 2018. Characteristics of deep water depositional system in Campos basin, Brazil. Petroleum Exploration and Development, 45(1), pp.99-110.

Horschutz, P. M. C., L. Freitas, C. V. Stank, A. d. S. Barroso, W. Cruz, and M. Halbouty, 1978, The Linguado, Carapeba, Vermelho and Marimbá Giant Fields, Campos Basin, Offshore Brazil: Giant oil and gas fields of the decade, v. 1988, p. 137-153.

Hubbard, S.M., de Ruig, M.J. and Graham, S.A., 2009. Confined channel-levee complex development in an elongate depo-center: deep-water Tertiary strata of the Austrian Molasse basin. Marine and Petroleum Geology, 26(1), pp.85-112.

Hudec, M. R., M. P. Jackson, and D. D. Schultz-Ela, 2005, A Compressional Origin for Minibasins near the Sigsbee Scarp, Gulf of Mexico.

Hudec, M. R., and M. P. A. Jackson, 2007, Terra infirma: Understanding salt tectonics: Earth-Science Reviews, v. 82, p. 1-28.

Hudec, M. R., M. P. A. Jackson, and D. D. Schultz-Ela, 2009, The paradox of minibasin subsidence into salt: Clues to the evolution of crustal basins: Geological Society of America Bulletin, v. 121, p. 201-221.

Jackson, C.A., Kane, K.E. and Larsen, E., 2010. Structural evolution of minibasins on the Utsira High, northern North Sea; implications for Jurassic sediment dispersal and reservoir distribution. Petroleum Geoscience, 16(2), pp.105-120.

Jackson, C. A.-L., M. P. Jackson, and M. R. Hudec, 2015a, Understanding the kinematics of salt-bearing passive margins: A critical test of competing hypotheses for the origin of the Albian Gap, Santos Basin, offshore Brazil: Geological Society of America Bulletin, v. 127, p. 1730-1751.

Jackson, C. A.-L., M. P. A. Jackson, M. R. Hudec, and C. Rodriguez, 2014 (a), Internal structure, kinematics, and growth of a salt wall: Insights from 3-D seismic data: Geology, v. 42, p. 307-310.

Jackson, C. A.-L., K. E. Kane, and E. Larsen, 2010, Structural evolution of minibasins on the Utsira High, northern North Sea; implications for Jurassic sediment dispersal and reservoir distribution: Petroleum Geoscience, v. 16, p. 105-120.

Jackson, C.A., 2011, Three-dimensional seismic analysis of megaclast deformation within a mass transport deposit; implications for debris flow kinematics. Geology, 39(3), pp.203-206.

Jackson, C. A. L., 2012, The initiation of submarine slope failure and the emplacement of mass transport complexes in salt-related minibasins: A three-dimensional seismic-reflection case study from the Santos Basin, offshore Brazil: Geological Society of America Bulletin, v. 124, p. 746-761.

Jackson, C. A. L., M. P. A. Jackson, M. R. Hudec, and C. R. Rodriguez, 2015b, Enigmatic structures within salt walls of the Santos Basin—Part 1: Geometry and kinematics from 3D seismic reflection and well data: Journal of Structural Geology, v. 75, p. 135-162.

Jackson, C.A.L., Rodriguez, C.R., Rotevatn, A. and Bell, R.E., 2014 (b). Geological and geophysical expression of a primary salt weld: An example from the Santos Basin, Brazil. Interpretation, 2(4), pp.SM77-SM89.

Jackson, M.P.A. and Cramez, C., 1989, December. Seismic recognition of salt welds in salt tectonics regimes. In Gulf of Mexico salt tectonics, associated processes and exploration potential: Gulf Coast Section SEPM Foundation 10th Annual Research Conference (pp. 66-71).

Jackson, M.P. and Hudec, M.R., 2017. Salt Tectonics: Principles and Practice. Cambridge University Press.

Jackson, M., and C. J. Talbot, 1991, A glossary of salt tectonics, Bureau of Economic Geology, University of Texas at Austin.

Janocko, M., W. Nemec, S. Henriksen, and M. Warchoł, 2013, The diversity of deep-water sinuous channel belts and slope valley-fill complexes: Marine and Petroleum Geology, v. 41, p. 7-34.

Jones, G., M. Mayall, and L. Lonergan, 2012, Contrasting depositional styles on a slope system and their control by salt tectonics: through-going channels, ponded fans, and mass transport complexes: Rosen, NC, Weimer, P., Coutes dos Anjos SM, Henrickson, S., Marques, E., Mayall, M., Fillon, p. 40-60.

Karner, G. D., and L. A. P. Gambôa, 2007, Timing and origin of the South Atlantic pre-salt sag basins and their capping evaporites: Geological Society, London, Special Publications, v. 285, p. 15-35.

Kolla, V., and J. Urruty, 2000, Ph. Bourges 'Evolution of a deep-water Tertiary sinuous channel offshore Angola (Africa) and implications to reservoir architecture': AAPG Bulletin, p. 1373.

Lin, C., Liu, J., Eriksson, K., Yang, H., Cai, Z., Li, H., Yang, Z. and Rui, Z., 2014. Late Ordovician, deep-water gravity-flow deposits, palaeogeography and tectonic setting, Tarim Basin, Northwest China. Basin Research, 26(2), pp.297-319.

Lopes, M., C. Bruhn, R. Santos, C. Corá, M. Becker, R. Alves, and D. Sarzenski, 1999, Architecture of Sand-Rich, Turbidite Reservoirs from Deep Water Campos Basin, Brazil: 1999 AAPG Conference & Exhibition, San Antonio, Texas.

Macedo, J., L. A. P. Gamboa, J. A. Ricci, L. F. G. Caddah, and W. Winter, 1998, Stratigraphic comparisons between the post-rift section of the Campos and Santos Basins, Southeast Brazilian margin: Extended Abstracts, AAPG: ABGP/AAPG International Conference and Exhibition, Rio de Janeiro.

Machado, L. C. R., R. O. Kowsmann, W. Almeida-Jr, C. Y. Murakami, S. Schreiner, D. J. Miller, and P. Piauilino, 2004, Geometria da porção proximal do sistema deposicional turbidítico moderno da Formação Carapebus, Bacia de Campos: modelo para heterogeneidades de reservatório: Boletim de Geociências da Petrobras, v. 12, p. 287-315.

Mayall, M., and I. Stewart, 2000, The architecture of turbidite slope channels: Deep-Water Reservoirs of the World: SEPM, Gulf Coast Section, 20th Annual Research Conference, p. 586.

Mayall, M. and O'Byrne, C., 2002, January. Reservoir prediction and development challenges in turbidite slope channels. In *Offshore Technology Conference*. Offshore Technology Conference.

Mayall, M., L. Lonergan, A. Bowman, S. James, K. Mills, T. Primmer, D. Pope, L. Rogers, and R. Skeene, 2010, The response of turbidite slope channels to growth-induced seafloor topography: AAPG bulletin, v. 94, p. 1011-1030.

McArthur, A.D., Claussmann, B., Bailleul, J., McCaffrey, W. and Clare, A., 2019. Variation in syn-subduction sedimentation patterns from inner to outer portions of deep-water fold and thrust belts: examples from the Hikurangi subduction margin of New Zealand. Geological Society, London, Special Publications, 490, pp.SP490-2018.

Meisling, K. E., P. R. Cobbold, and V. S. Mount, 2001, Segmentation of an Obliquely Rifted Margin, Campos and Santos Basins, Southeastern Brazil: AAPG Bulletin, v. 85, p. 1903-1924.

Modica, C. J., and E. R. Brush, 2004, Postrift sequence stratigraphy, paleogeography, and fill history of the deep-water Santos Basin, offshore southeast Brazil: AAPG Bulletin, v. 88, p. 923-945.

Mohriak, W., M. Mello, J. Dewey, and J. Maxwell, 1990, Petroleum geology of the Campos Basin, offshore Brazil: Geological Society, London, Special Publications, v. 50, p. 119-141.

Moraes, M. A., 1989, Diagenetic evolution of Cretaceous-Tertiary turbidite reservoirs, Campos Basin, Brazil: AAPG Bulletin, v. 73, p. 598-612.

Moraes, M. A., P. R. Blaskovski, and P. Joseph, 2004, The Grès d’Annot as an analogue for Brazilian Cretaceous sandstone reservoirs: comparing convergent to passive-margin confined turbidites: Geological Society, London, Special Publications, v. 221, p. 419-437.

Moreira, J. L. P., C. Madeira, J. A. Gil, and M. A. P. Machado, 2007, Bacia de Santos: Bulletin Geociencias Petrobras, v. 15, p. 531-549.

Morley, C.K., 2003. Mobile shale related deformation in large deltas developed on passive and active margins. Geological Society, London, Special Publications, 216(1), pp.335-357.

Oluboyo, A., R. Gawthorpe, K. Bakke, and F. Hadler-Jacobsen, 2014, Salt tectonic controls on deep-water turbidite depositional systems: Miocene, southwestern Lower Congo Basin, offshore Angola: Basin Research, v. 26, p. 597-620.

Ortiz-Karpf, A., Hodgson, D.M. and McCaffrey, W.D., 2015. The role of mass-transport complexes in controlling channel avulsion and the subsequent sediment dispersal patterns on an active margin: the Magdalena Fan, offshore Colombia. Marine and Petroleum Geology, 64, pp.58-75.

Pessoa, J., C. C. Martins, J. Heinerici, R. J. Jahnert, A. B. França, L. Trindade, and C. Francisco, 1999, Petroleum System And Seismic Expression In The Campos Basin: 6th International Congress of the Brazilian Geophysical Society.

Pichel, L.M., Jackson, C.A.L., Peel, F. and Dooley, T., 2018. Effects of Pre-salt Relief on Salt Tectonics on the S o Paulo Plateau and Implications for the Albian Gap.

Pirmez, C., Beaubouef, R.T., Friedmann, S.J., Mohrig, D.C. and Weimer, P., 2000, December. Equilibrium profile and baselevel in submarine channels: examples from Late Pleistocene systems and implications for the architecture of deepwater reservoirs. In Global deep-water reservoirs: Gulf Coast Section SEPM Foundation 20th Annual Bob F. Perkins Research Conference (pp. 782-805).

Posamentier, H. W., and V. Kolla, 2003, Seismic geomorphology and stratigraphy of depositional elements in deep-water settings: Journal of Sedimentary Research, v. 73, p. 367-388.

Prather, B.E., 2003. Controls on reservoir distribution, architecture and stratigraphic trapping in slope settings. Marine and Petroleum Geology, 20(6-8), pp.529-545.

Prather, B.E., Booth, J.R., Steffens, G.S. and Craig, P.A., 1998. Classification, lithologic calibration, and stratigraphic succession of seismic facies of intraslope basins, deep-water Gulf of Mexico. AAPG bulletin, 82(5), pp.701-728.

Prélat, A., Covault, J.A., Hodgson, D.M., Fildani, A. and Flint, S.S., 2010. Intrinsic controls on the range of volumes, morphologies, and dimensions of submarine lobes. Sedimentary Geology, 232(1), pp.66-76.

Rodriguez, C.R., Jackson, C.L., Rotevatn, A., Bell, R.E. and Francis, M., 2018. Dual tectonic-climatic controls on salt giant deposition in the Santos Basin, offshore Brazil. Geosphere, 14(1), pp.215-242.

Rowan, M. G., F. J. Peel, and B. C. Vendeville, 2004, Gravity-driven fold belts on passive margins, in K. R. McClay, ed., Thrust tectonics and hydrocarbon systems: AAPG Memoir 82, p.157-182.

Rowan, M.G. and Weimer, P., 1998, Salt-sediment interaction, northern Green Canyon and Ewing bank (offshore Louisiana), northern Gulf of Mexico. AAPG bulletin, 82(5), pp.1055-1082.

Saller, A., Werner, K., Sugiaman, F., Cebastiant, A., May, R., Glenn, D. and Barker, C., 2008. Characteristics of Pleistocene deep-water fan lobes and their application to an upper Miocene reservoir model, offshore East Kalimantan, Indonesia. AAPG bulletin, 92(7), pp.919-949.

Schlumberger, 2012, Interpreter's guide to seismic attribuite, 4^{th} edition, p. 112-114.

Sinclair, H.D. and Tomasso, M., 2002, Depositional evolution of confined turbidite basins. Journal of Sedimentary Research, 72(4), pp.451-456.

Spychala, Y.T., Hodgson, D.M., Flint, S.S. and Mountney, N.P., 2015. Constraining the sedimentology and stratigraphy of submarine intraslope lobe deposits using exhumed examples from the Karoo Basin, South Africa. Sedimentary Geology, 322, pp.67-81.

Spychala, Y.T., Hodgson, D.M., Stevenson, C.J. and Flint, S.S., 2017. Aggradational lobe fringes: The influence of subtle intrabasinal seabed topography on sediment gravity flow processes and lobe stacking patterns. Sedimentology, 64(2), pp.582-608.

Stewart, S. A., 2007, Salt tectonics in the North Sea Basin: a structural style template for seismic interpreters: Geological Society, London, Special Publications, v. 272, p. 361-396.

Stewart, S. A., and J. A. Clark, 1999, Impact of salt on the structure of the Central North Sea hydrocarbon fairways: Geological Society, London, Petroleum Geology Conference series, v. 5, p. 179-200.

Sylvester, Z., Cantelli, A. and Pirmez, C., 2015. Stratigraphic evolution of intraslope minibasins: Insights from surface-based model. AAPG Bulletin, 99(6), pp.1099-1129.

Trusheim, F., 1960. Mechanism of salt migration in northern Germany. AAPG Bulletin, 44(9), pp.1519-1540.

Viana, A., Figueiredo, A., Faugeres, J.C., Lima, A., Gonthier, E., Brehme, I. and Zaragosi, S., 2003. The Sao Tomé deep-sea turbidite system (southern Brazil Basin): Cenozoic seismic stratigraphy and sedimentary processes. AAPG bulletin, 87(5), pp.873-894.

Waisman, G., 2008, Tectonica de sal da Bacia de Campos: Sal: Geologia e Tectônica. Editora Beca, Sao Paulo. Editora Beca, Sao Paulo, p. 314-339.

Wang, X., Luthi, S.M., Hodgson, D.M., Sokoutis, D., Willingshofer, E. and Groenenberg, R.M., 2017. Turbidite stacking patterns in salt-controlled minibasins: Insights from integrated analogue models and numerical fluid flow simulations. Sedimentology, 64(2), pp.530-552.

Winker, C.D., 1996, January. High-resolution seismic stratigraphy of a late Pleistocene submarine fan ponded by salt-withdrawal mini-basins on the Gulf of Mexico continental slope. In Offshore Technology Conference. Offshore Technology Conference.

Winter, W., R. Jahnert, and A. França, 2007, Bacia de Campos: Boletim de Geociências da PETROBRAS, v. 15, p. 511-529.

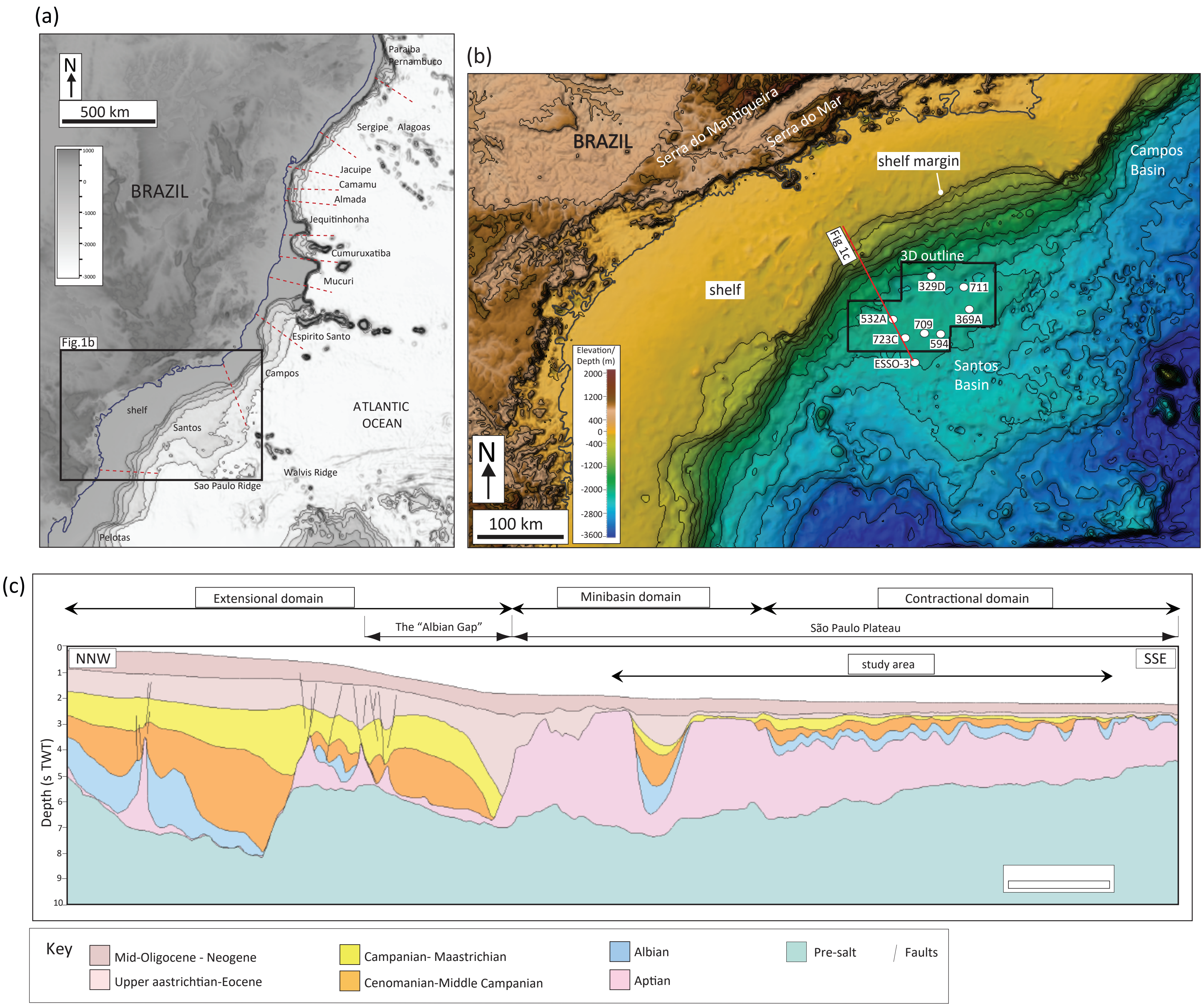

FIGURE 1: (a) Offshore eastern Brazil sedimentary basins; (b) Santos Basin topography and bathymetry map highlighting the location of study area and dataset. 3D seismic reflection data courtesy of CGG and public Brazilian boreholes; (c) Geoseismic profile across the study area based on interpretation of 2D seismic data courtesy of WesternGeco, Schlumberger. See location in b; (d) Seismic stratigraphic framework. After Modica and Brush (2004); Moreira et al. (2007); Jackson (2012).

(d)

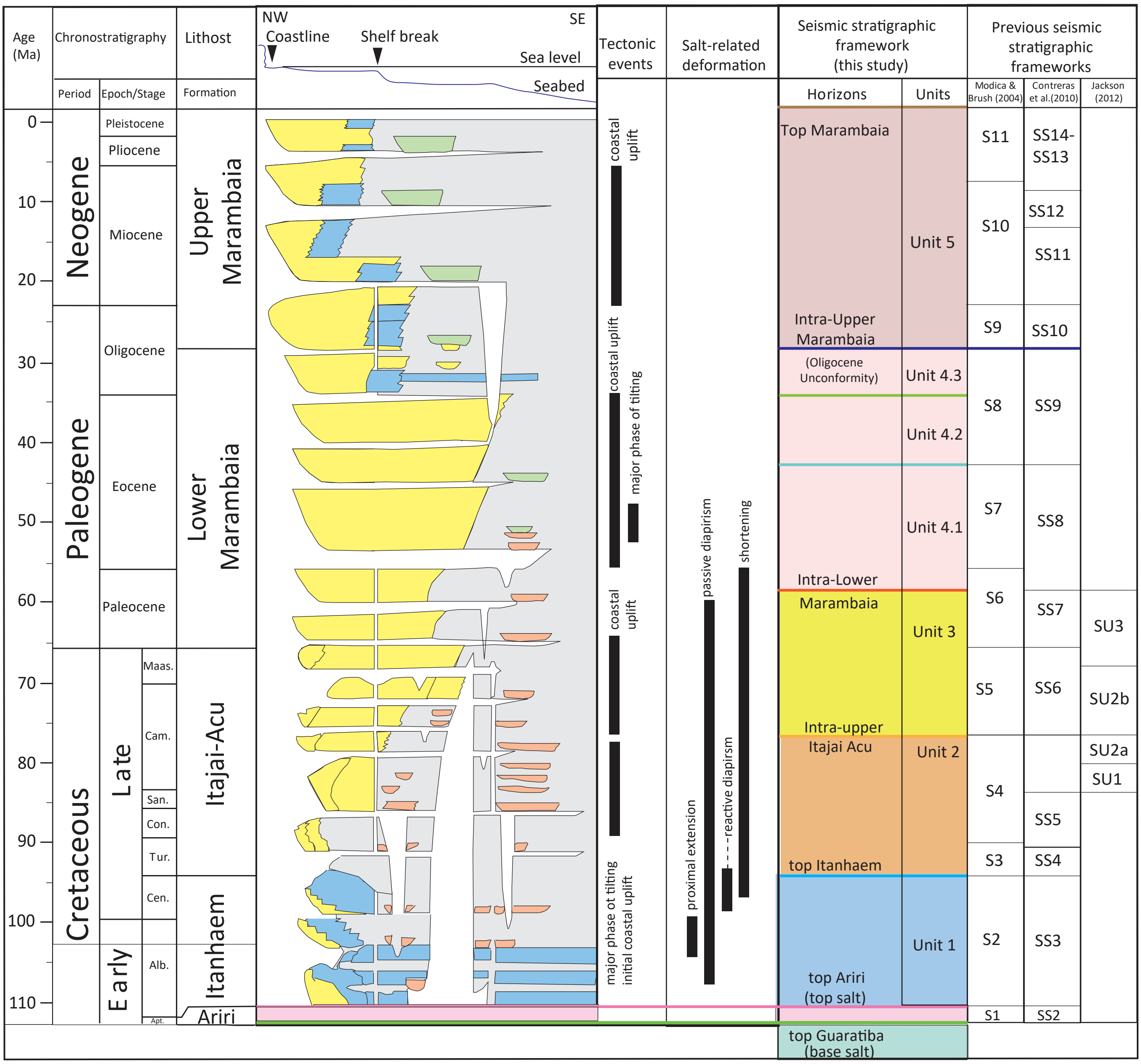

Key to lithologies and depositional e nvironments

- Fluvial to shallow-marine sandstone
- Slope to basin floor mudstone
- Mudstone-dominated mass-transport deposit
- Slope to basin floor turbidite sandstone
- Carbonate (undifferentiated)
- Salt

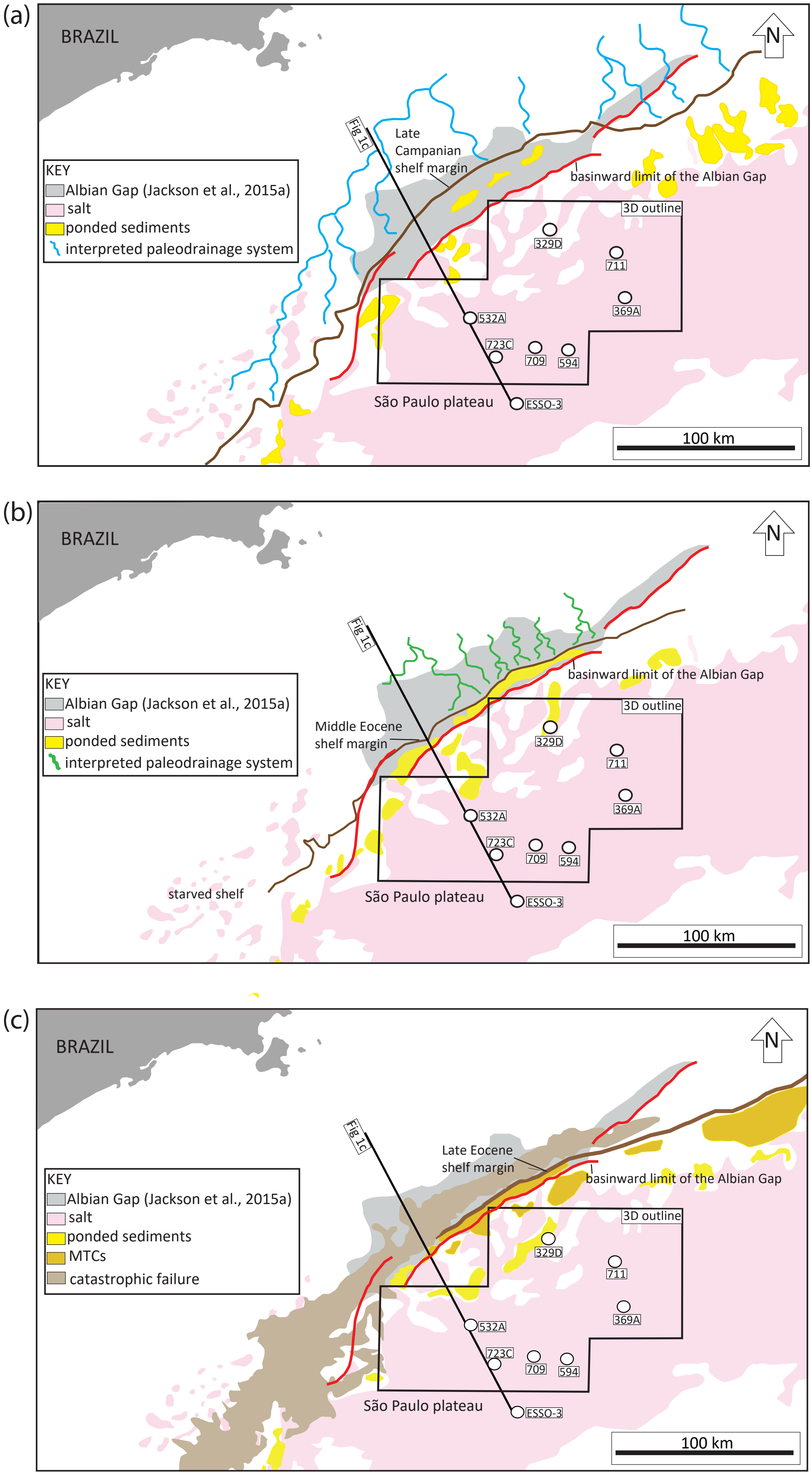

Figure 2: Central deepwater Santos Basin paleogeography highlighting sedimentation trapped or ponded landwards of the Albian Gap with limited deposition in the area of study. Modified after Modica and Brush, 2004. (a) Late Campanian paleogeography; (b) Middle Eocene paleogeography; (c) Late Eocene paleogeography.

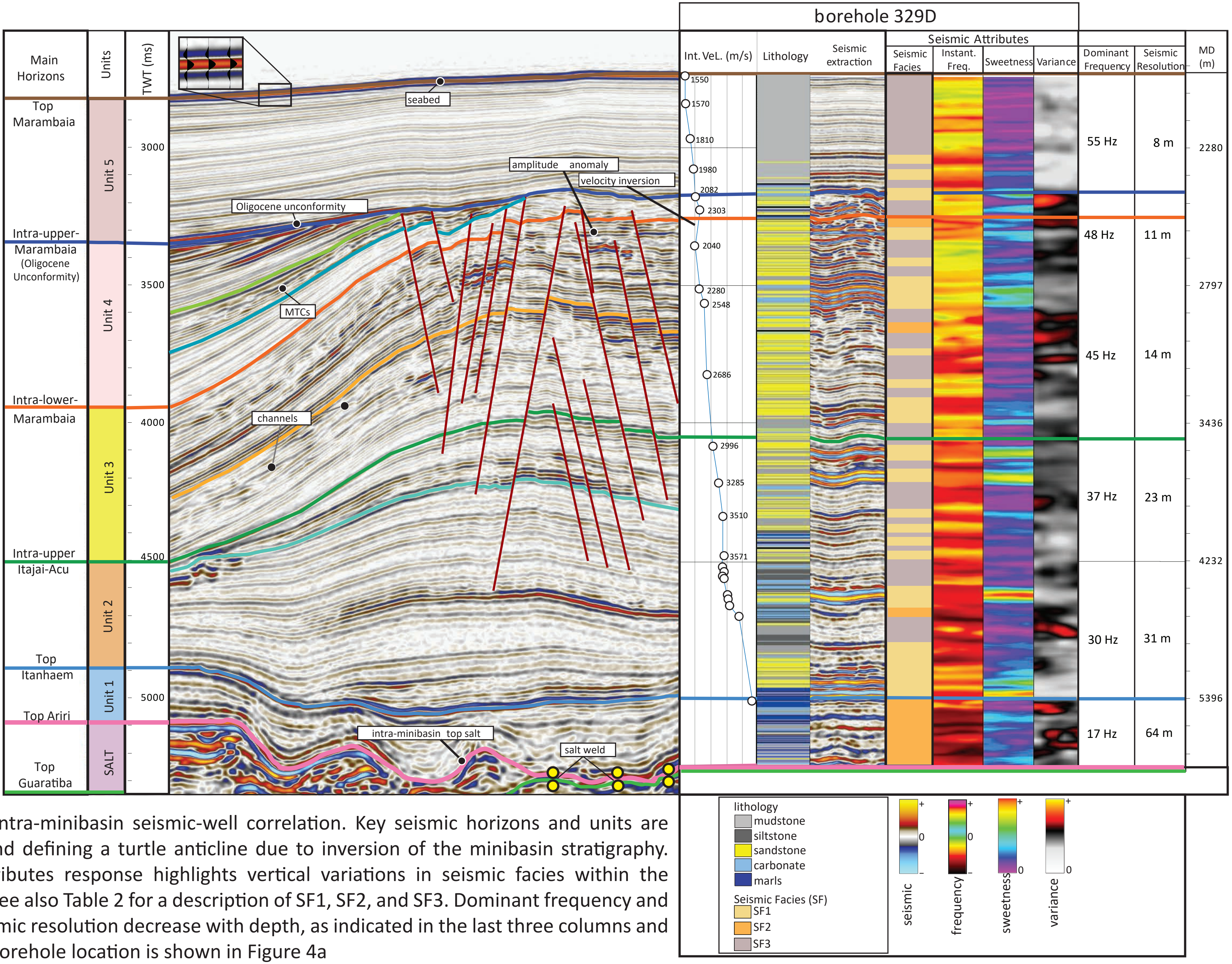

FIGURE 3: Intra-minibasin seismic-well correlation. Key seismic horizons and units are indicated and defining a turtle anticline due to inversion of the minibasin stratigraphy. Seismic attributes response highlights vertical variations in seismic facies within the minibasin. See also Table 2 for a description of SF1, SF2, and SF3. Dominant frequency and vertical seismic resolution decrease with depth, as indicated in the last three columns and in Table 1. Borehole location is shown in Figure 4a

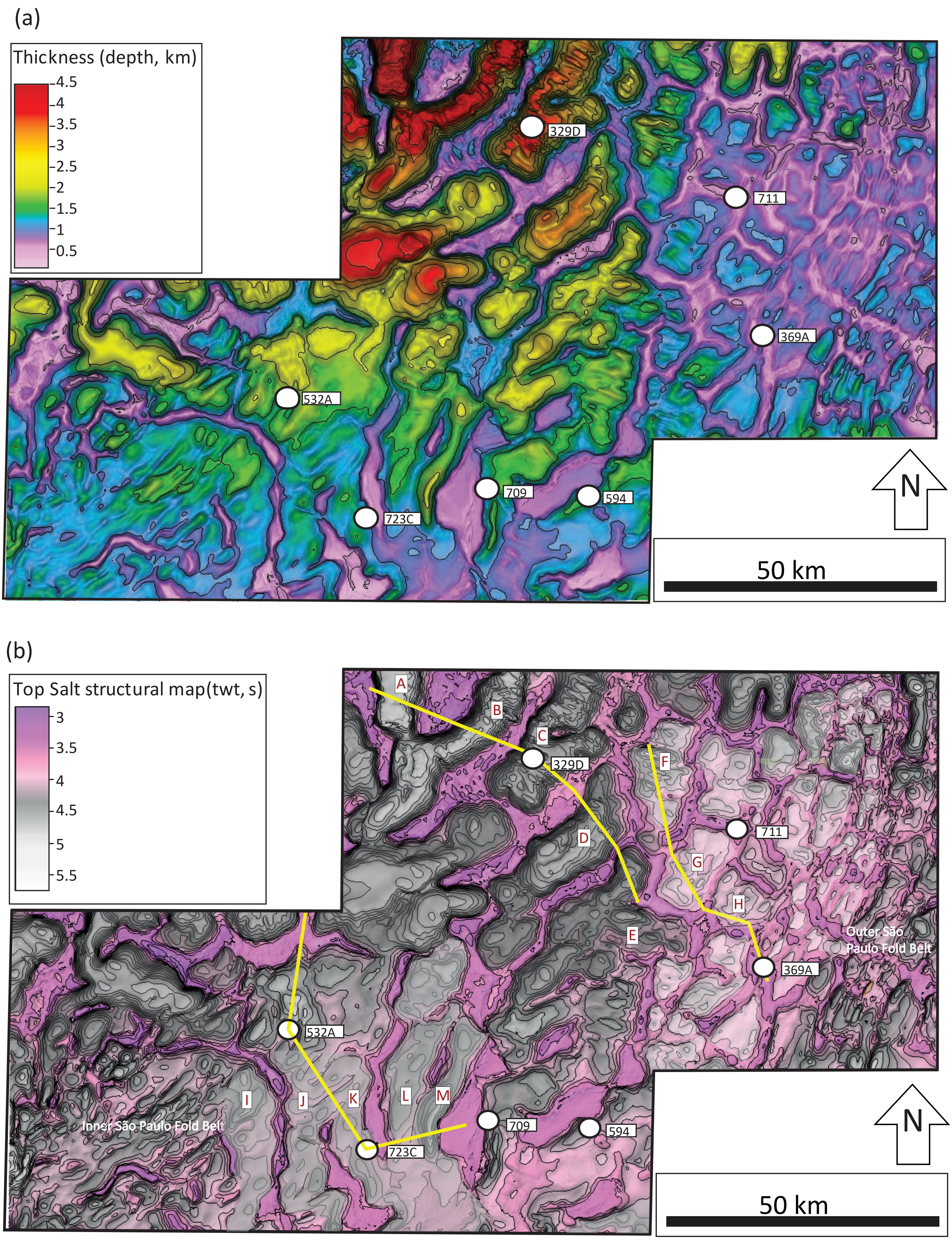

FIGURE 4: (a) Postsalt isopach (Seabed to top salt depth thickness map) illustrating sediment thickness variations across the study area. Depth thickness map estimated using the depth-converted seafloor depth structural map and the top salt structural map also in depth; (b) Top Salt structural map highlighting present-day salt structures bounding the minibasins of interest, i.e. updip proximal thick minibasins (A-E), shallow minibasins (F-H), and downdip distal minibasins (I-M) ; (c) Geoseismic section across the updip proximal thick minibasins; (d) Geoseismic section across the medial shallow minibasins; (e) Geoseismic section across the downdip distal elongated minibasins. See Figure 4b for location of geoseismic profiles.

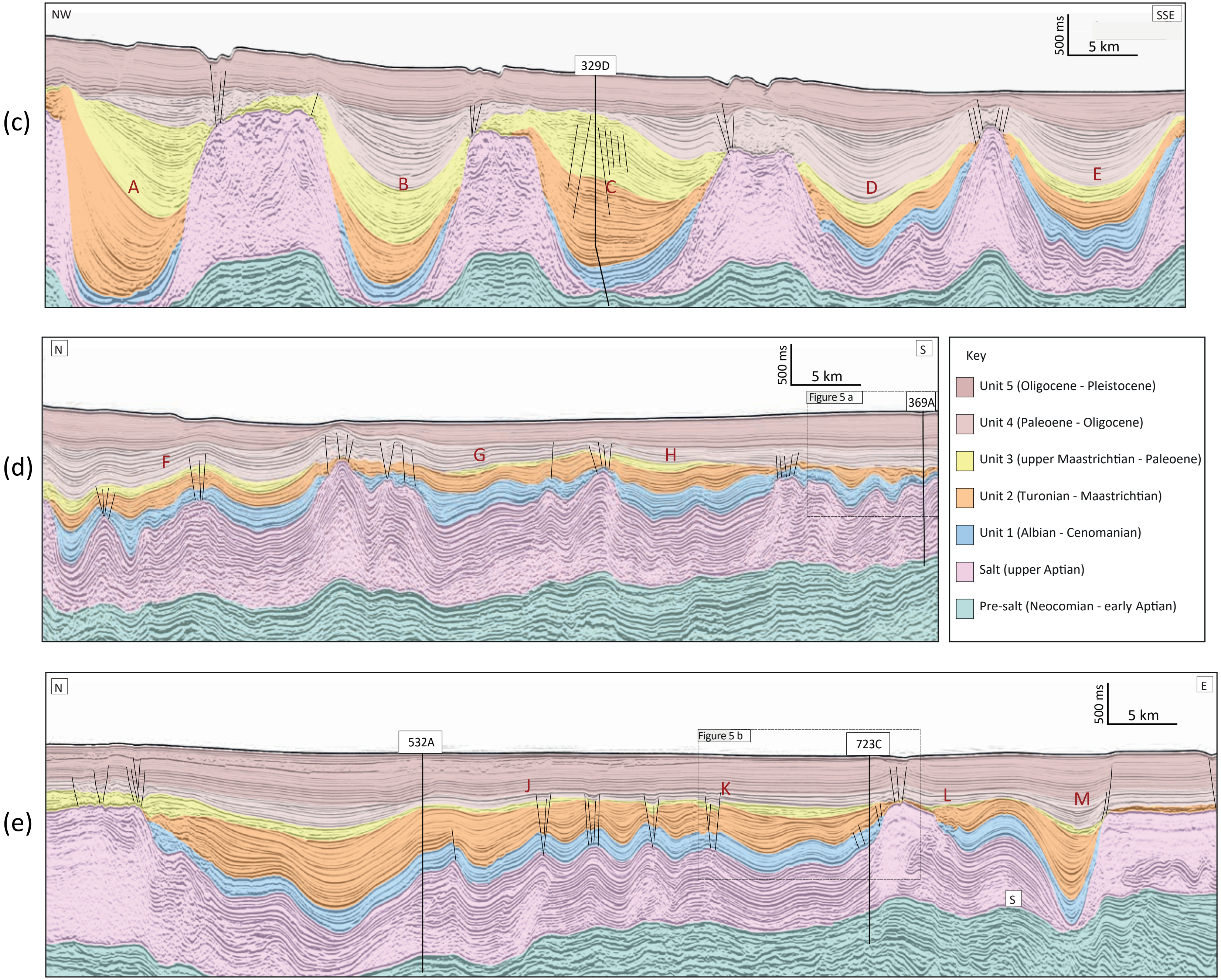
(c)
NW
SSE
500 ms
5 km
329D
A
B
C
D
E
(d)
N
S
500 ms
5 km
Figure 5 a
369A
F
G
H
Key
Unit 5 (Oligocene - Pleistocene)
Unit 4 (Paleoene - Oligocene)
Unit 3 (upper Maastrichtian - Paleoene)
Unit 2 (Turonian - Maastrichtian)
Unit 1 (Albian - Cenomanian)
Salt (upper Aptian)
Pre-salt (Neocomian - early Aptian)
(e)
N
E
500 ms
5 km
532A
Figure 5 b
723C
J
K
L
M
S

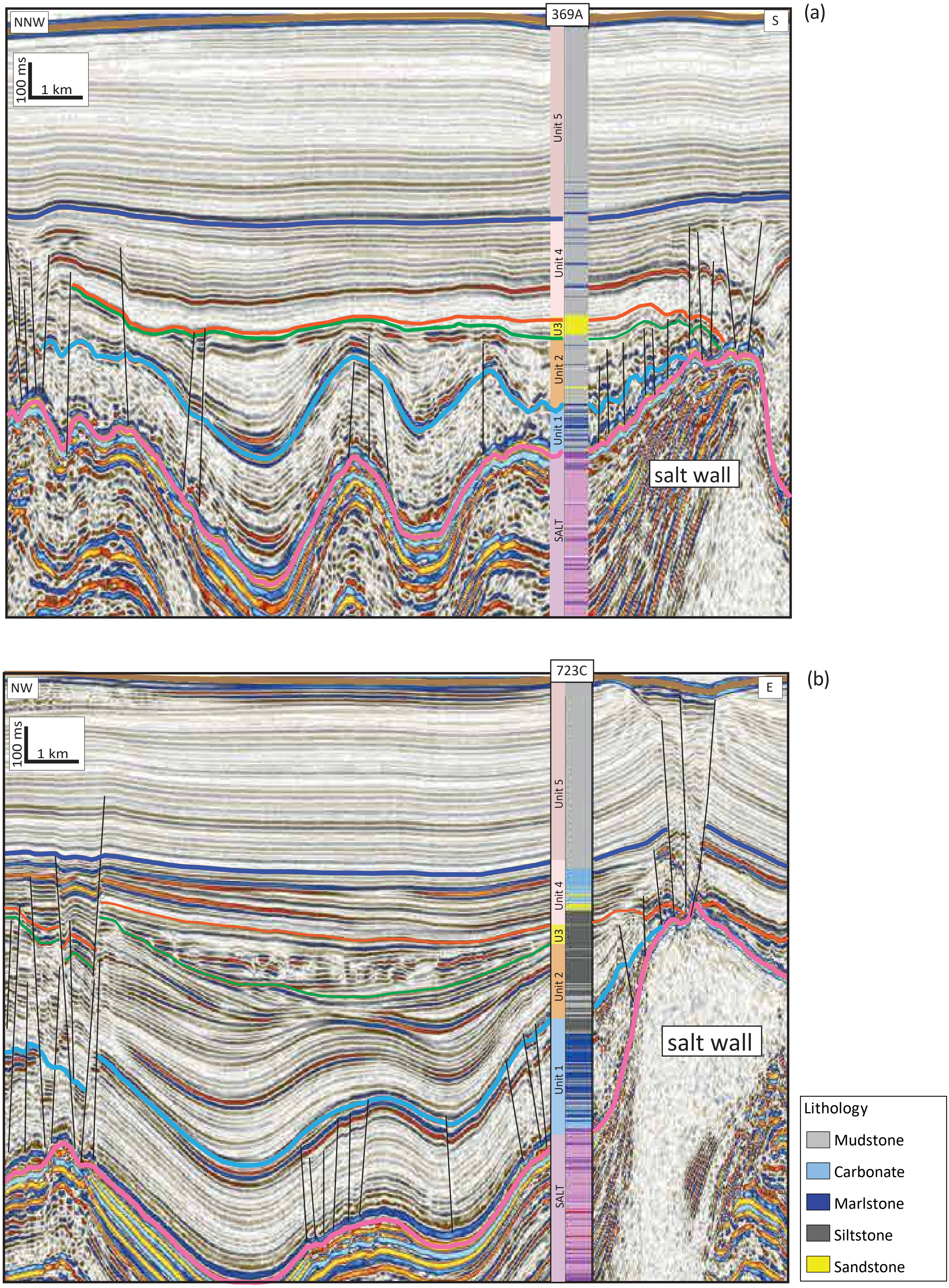

FIGURE 5: Intra-minibasin seismic-well tie showing the presence of reservoir-prone sandstones in distal locations, i.e., > 50 km from the coeval shelf margin. (a) Borehole 369a penetrates a medial shallow minibasin. See Figure 4a for location. (b) Borehole 723C penetrates the flank of a downdip distal minibasin. See Figure 4a for location.

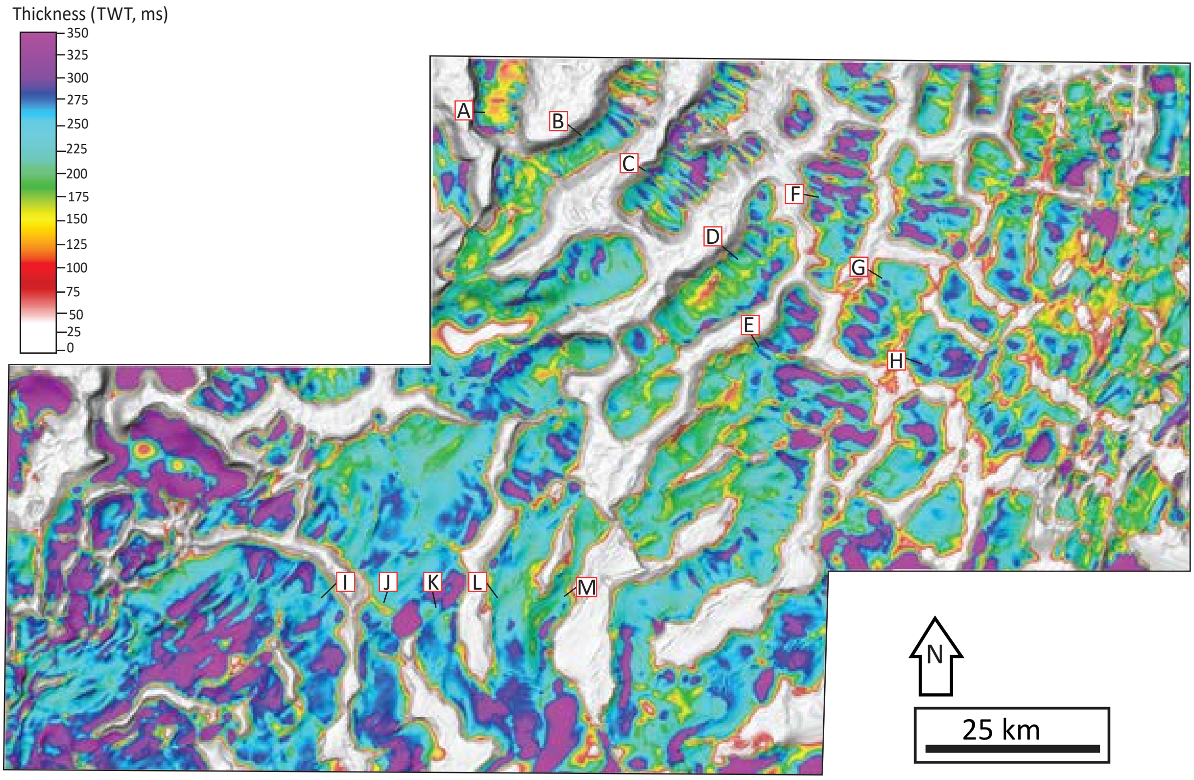

FIGURE 6.a: Unit 1 time thickness map

FIGURE 6: Regional isochrons illustrating deposition and salt-related deformation in the post-salt of central deep-water Santos Basin. (a) Albian-Cenomanian unit 1 twt thickness map; (b) Turonian to Mid-Campanian Unit 2 twt thickness map; (c) Campanian to Paleocene Unit 3 twt thickness map; (d) Paleocene to Mid Oligocene Unit 4 twt thickness map; (e) Mid-Oligocene to present-day Unit 5 twt thickness map.

FIGURE 6b: Unit 2 twt thickness map

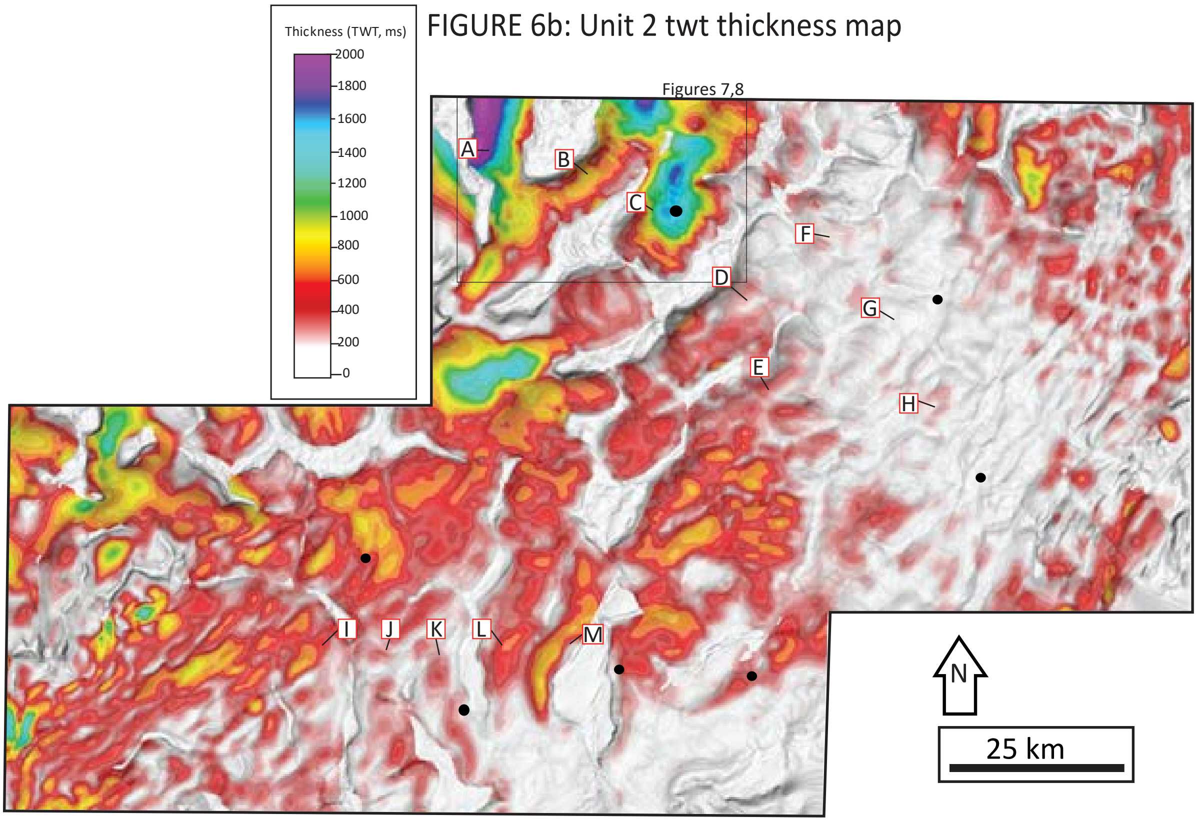

FIGURE 6c: Unit 3 twt thickness map

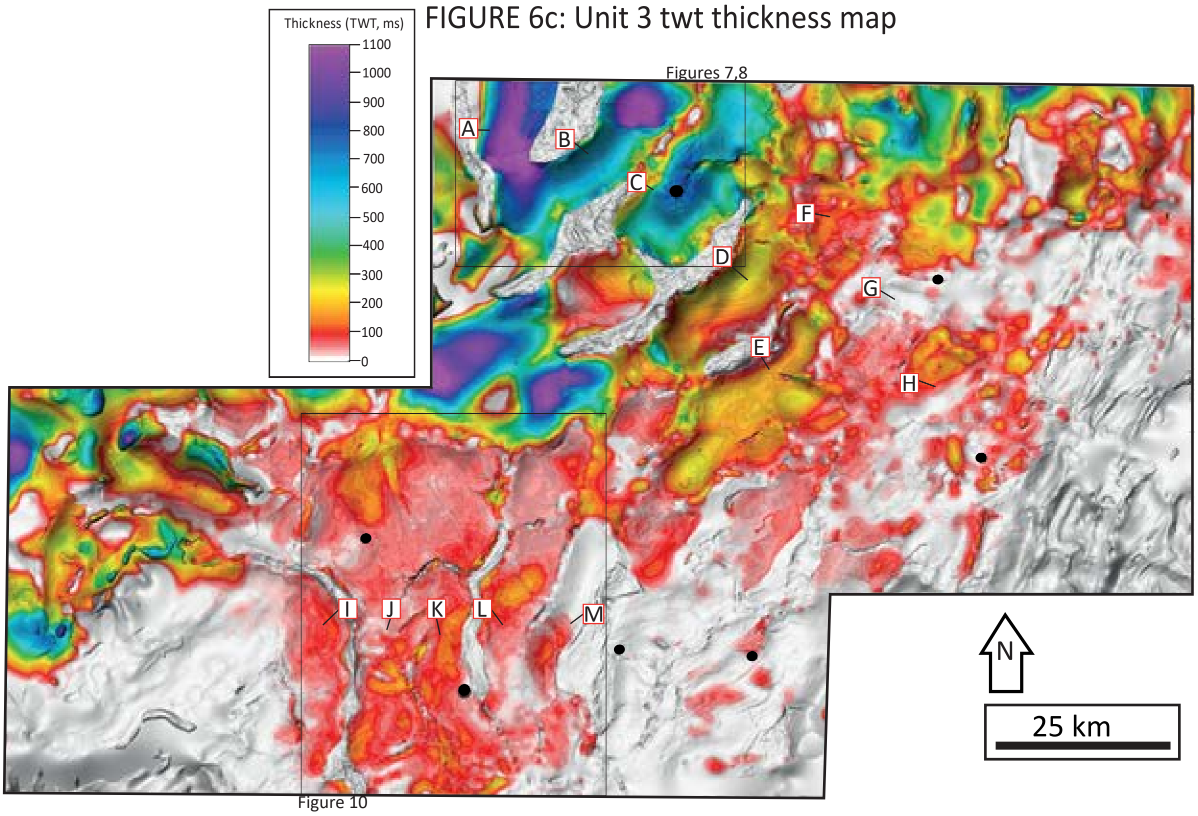

FIGURE 6d: Unit 4 twt thickness map

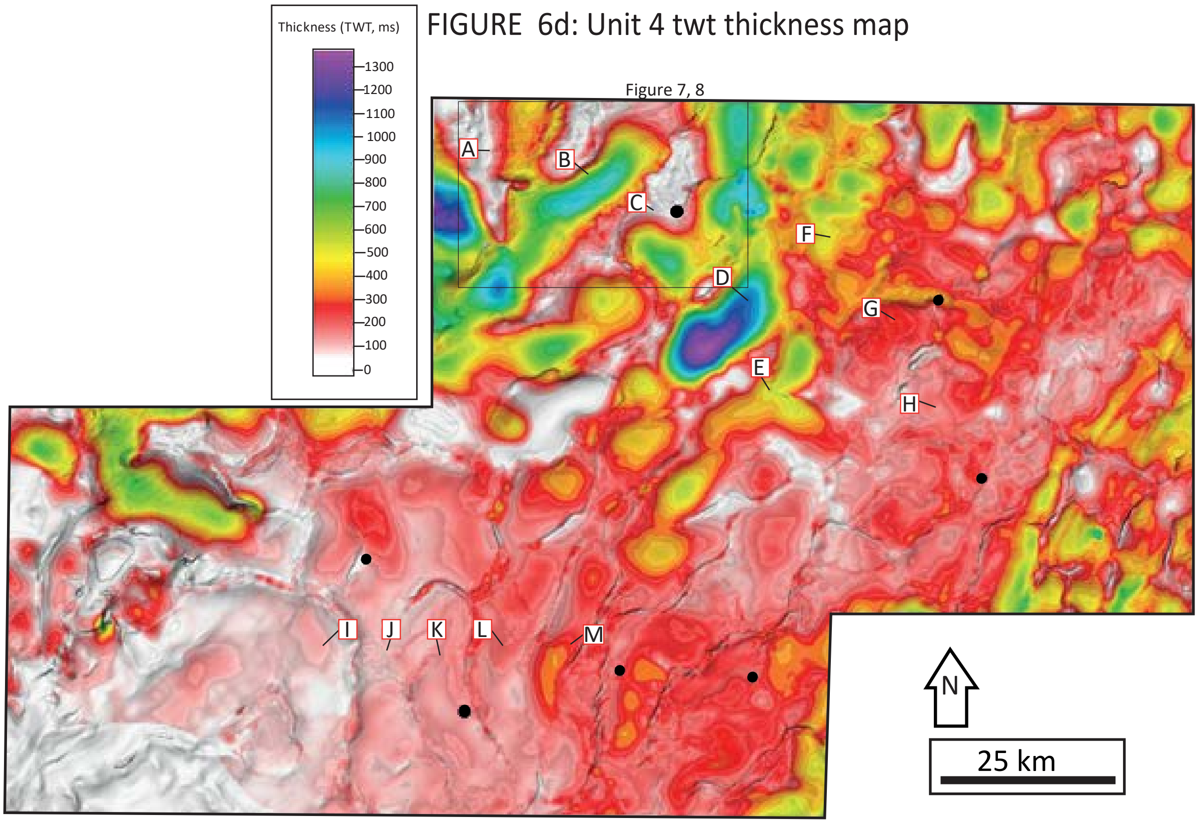

FIGURE 6e: Unit 5 twt thickness map

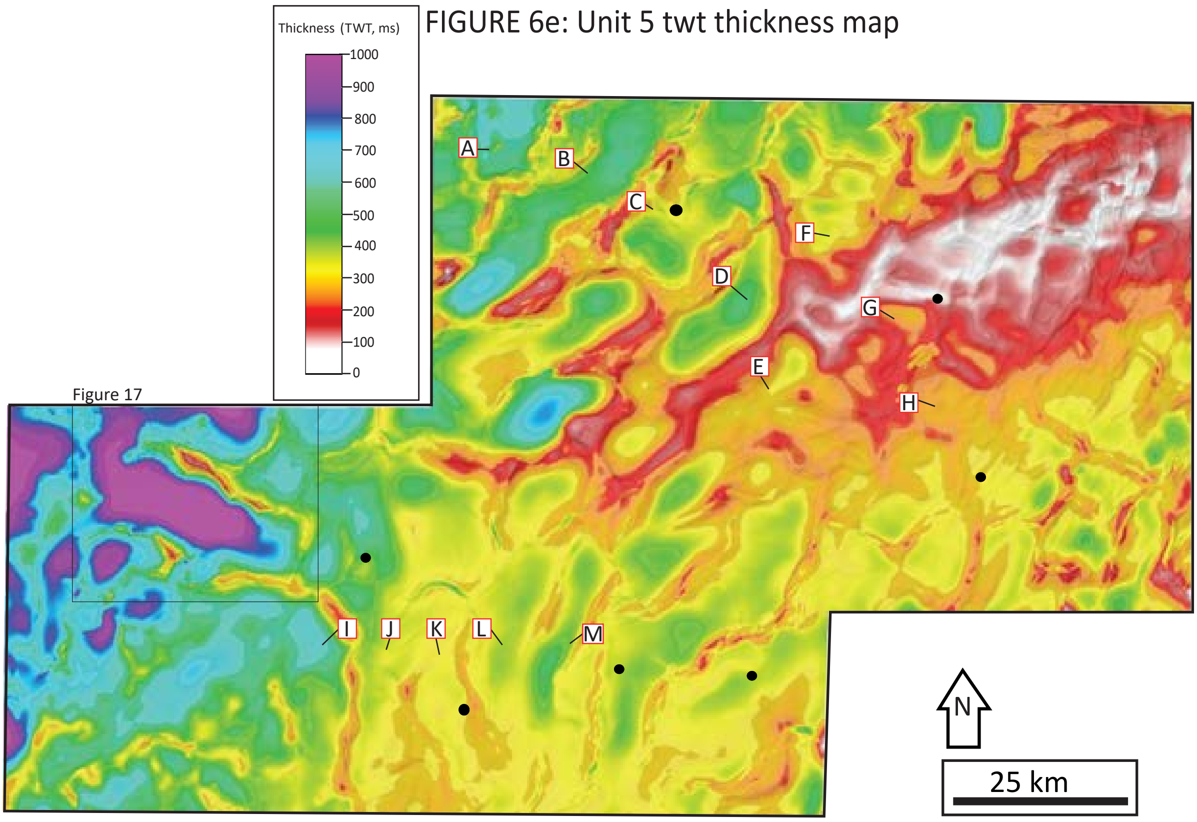

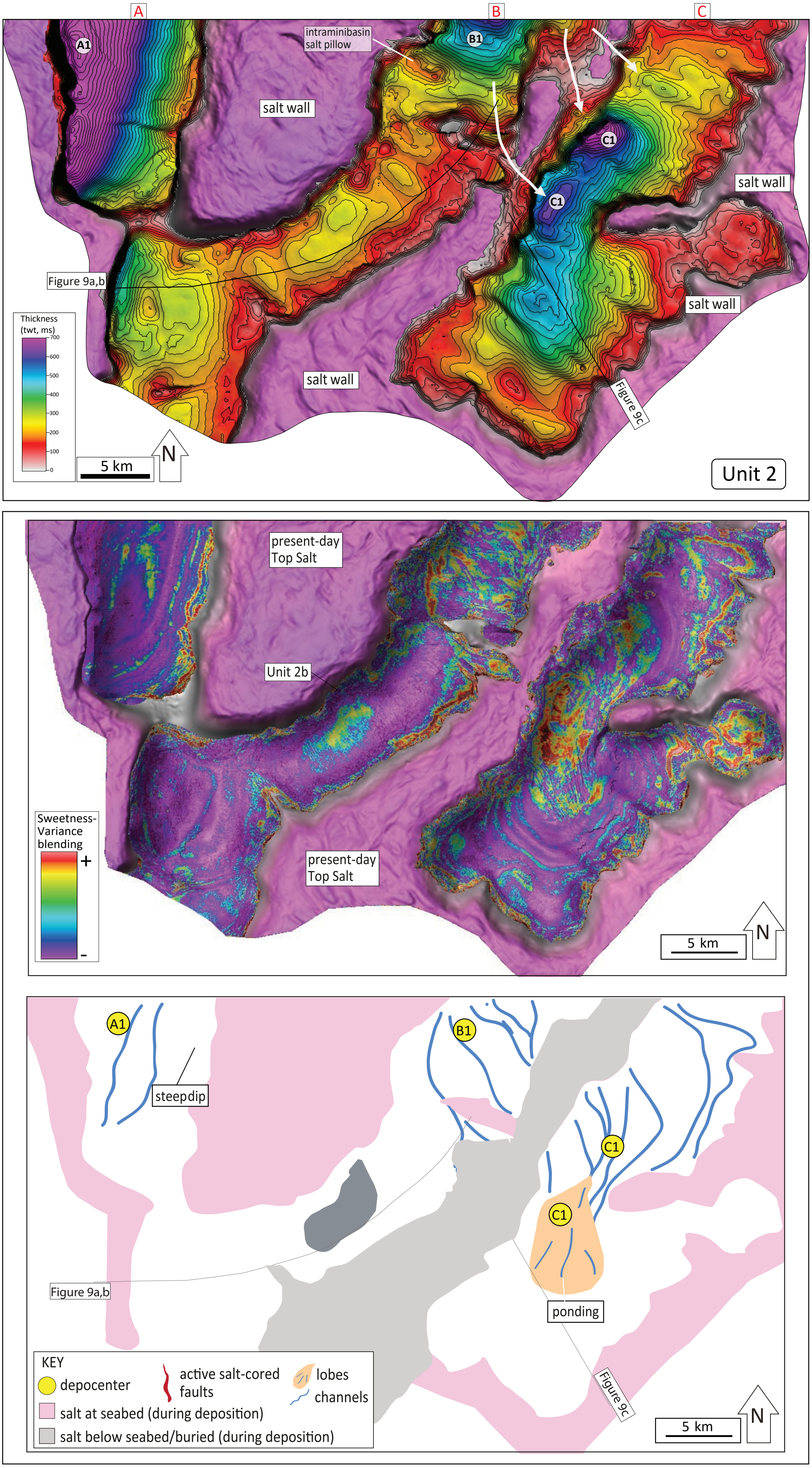

FIGURE 7: (a) Unit 2 thickness map highlighting initial depocenters A1, B1 and C1 within updip proximal minibasins A, B and C. Present-day Top Salt is shown in pink. (b) Unit 2b seismic attributes blending (interval is shown on section in Figure 9c). Present-day Top Salt structure map is shown in pink. Attributes visually blended correspond to Variance and Sweetness (described in the Methods section). Purple colours correspond to more transparent background facies. Yellow to red colours highlight deep-water depositional elements interpreted in the accompanying map. Depocenters A1, B1 and C1 are interpreted based on thickness map in Figure 7a.

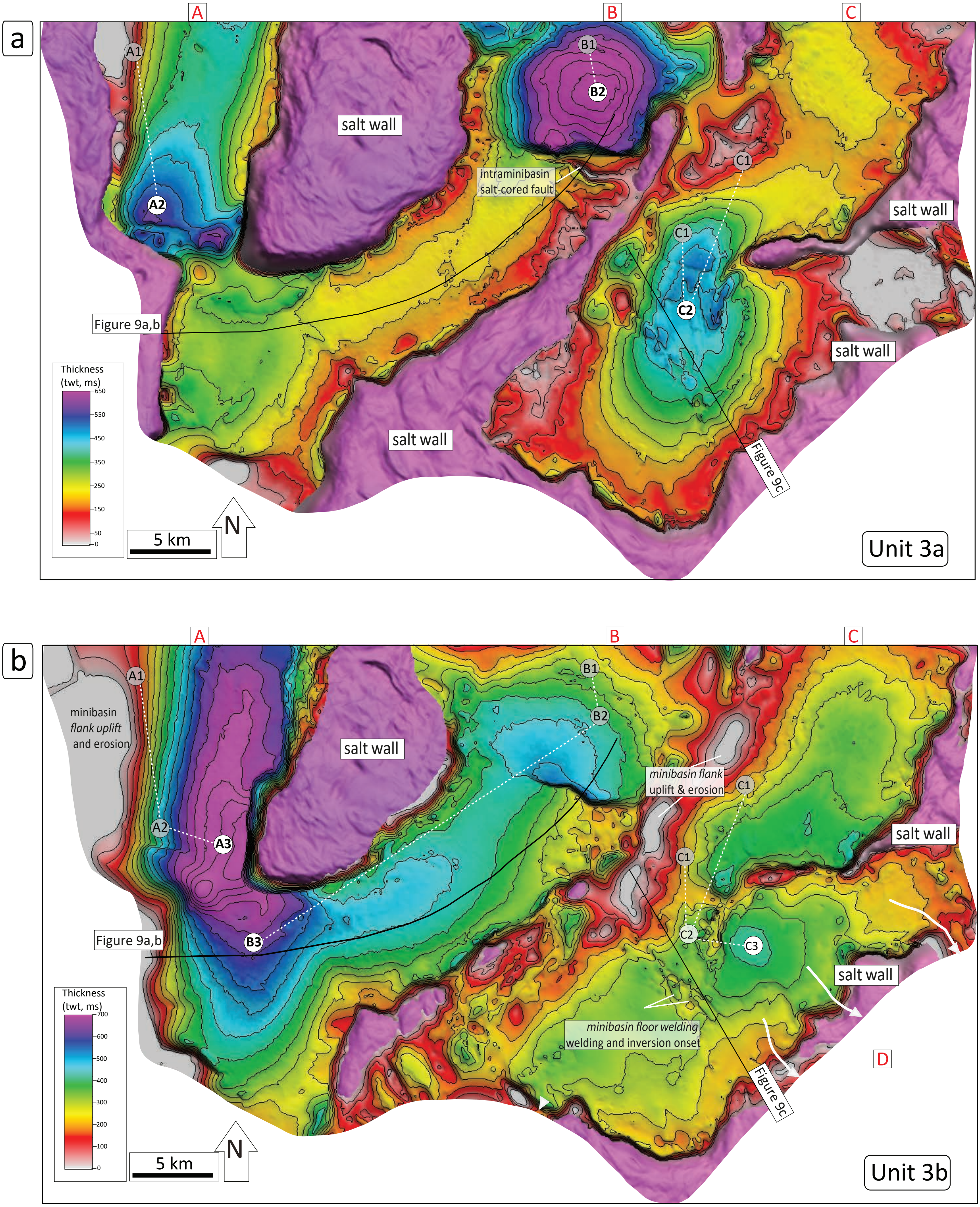

FIGURE 8: (a) Proximal thick minibasins - Sub-Unit 3a isochron highlighting shifting of depocenters A1, B1, C1 (Fig. 7a) to new depocenters A2, B2 and C2. Present-day Top Salt is shown in pink. (b) Proximal thick minibasins - Sub-Unit 3b isochron highlighting shifting of depocenters A2, B2 and C2 (Fig 8a) to new depocenters A3, B3 and C3. (c) Sub-unit 3a seismic attributes blending and interpretation. Sub-unit 3a is shown on sections in Figures 9a, b and c. Visually blended seismic attributes correspond to Variance and Sweetness described in the Methods section. Purple and dark blue colours correspond to more transparent background facies. Yellow to red colours highlight deep-water depositional systems interpreted in the accompanying map. Depocenters are interpreted based on the isochron (Fig. 8a). (d) Sub-unit 3b seismic attributes blending and interpretation. Sub-unit 3b is shown on sections in Figures 9a, b and c. Visually blended attributes correspond to Variance and Sweetness. Purple and dark blue colours correspond to more transparent background facies. Yellow to red colours highlight depositional elements interpreted in the accompanying map. Depocenters are interpreted based on the isochron (Fig. 8b).

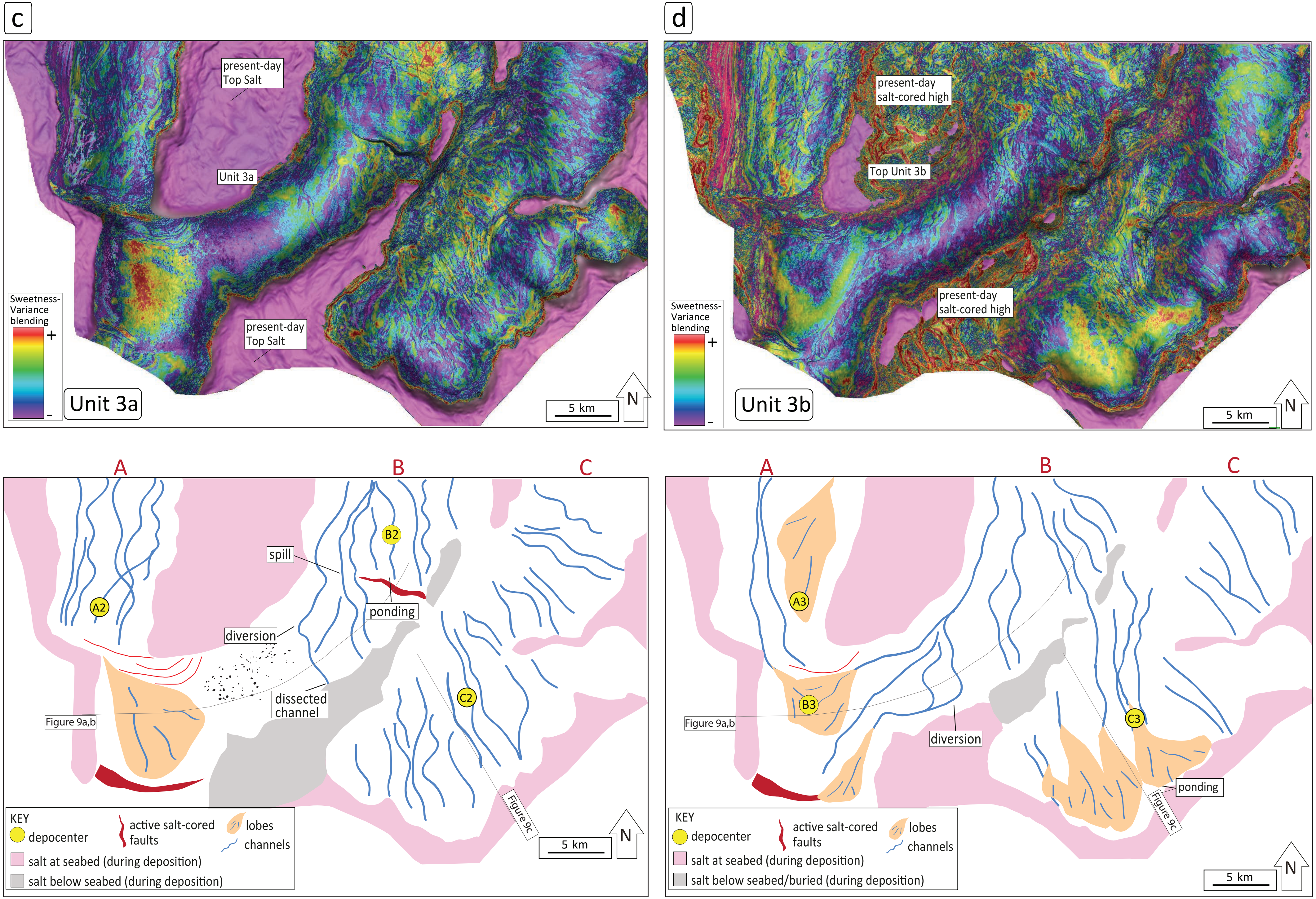

c
present-day Top Salt
Unit 3a
present-day Top Salt
Sweetness-Variance blending
+
-
Unit 3a
5 km
N
d
present-day salt-cored high
Top Unit 3b
present-day salt-cored high
Sweetness-Variance blending
+
-
Unit 3b
5 km
N
A
B
C
spill
B2
ponding
A2
diversion
dissected channel
C2
Figure 9a,b
Figure 9c
KEY
depocenter
active salt-cored faults
lobes
channels
salt at seabed (during deposition)
salt below seabed (during deposition)
5 km
N
A
B
C
A3
B3
C3
Figure 9a,b
diversion
ponding
Figure 9c
KEY
depocenter
active salt-cored faults
lobes
channels
salt at seabed (during deposition)
salt below seabed/buried (during deposition)
5 km
N

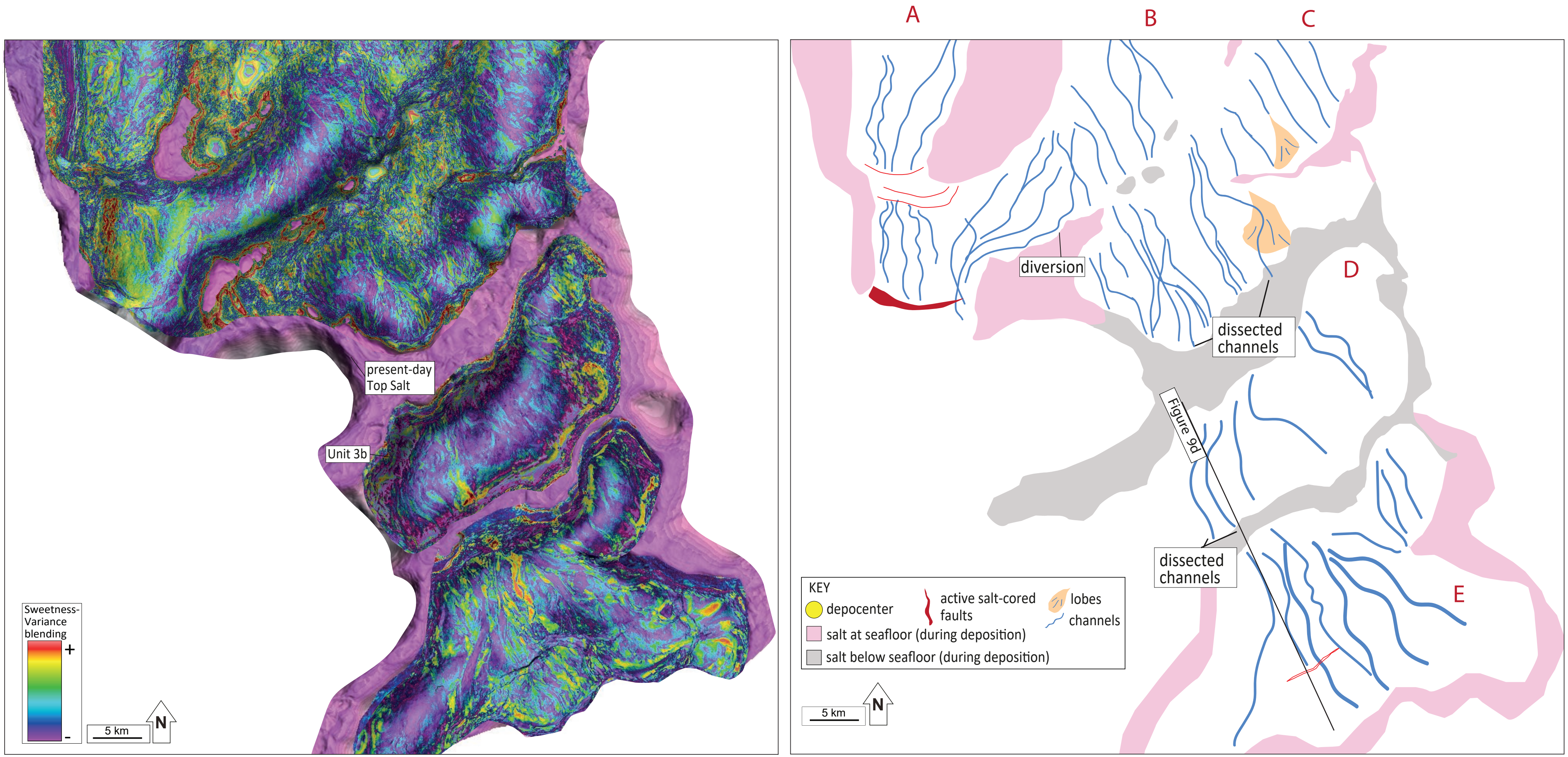

Figure 8e: Unit 3b sweetness and variance attribute visual blending illustrating the post-depositional dissection of submarine clastic systems caused by the rise of the salt wall presently bounding minibasins B and C, C and D and D and E.

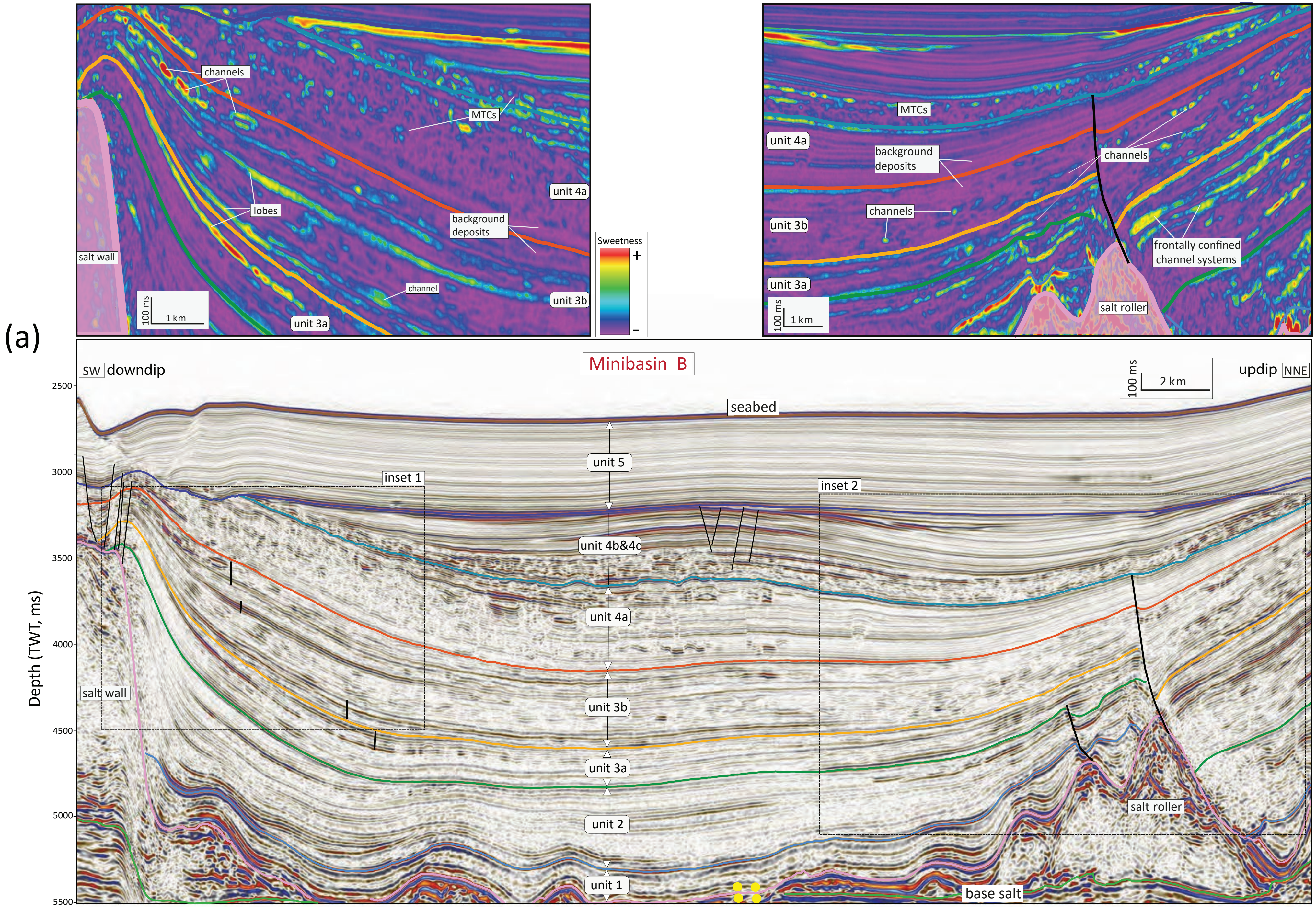

Figure 9: Seismic profiles along and across the updip/proximal minibasins illustrating the key horizons and units mapped and the thickness and seismic facies variations defining the minibasin stratigraphy. Highly-reflective intervals correspond to interpreted depositional elements highlighted with seismic attributes in Figure 8. The locations of the seismic sections are also shown on Figure 8. (a) Seismic section along Minibasin B. Insets illustrate potential sandstone-rich depositional elements with an amplitude- and frequency-based seismic attribute (Sweetnes).

(b)

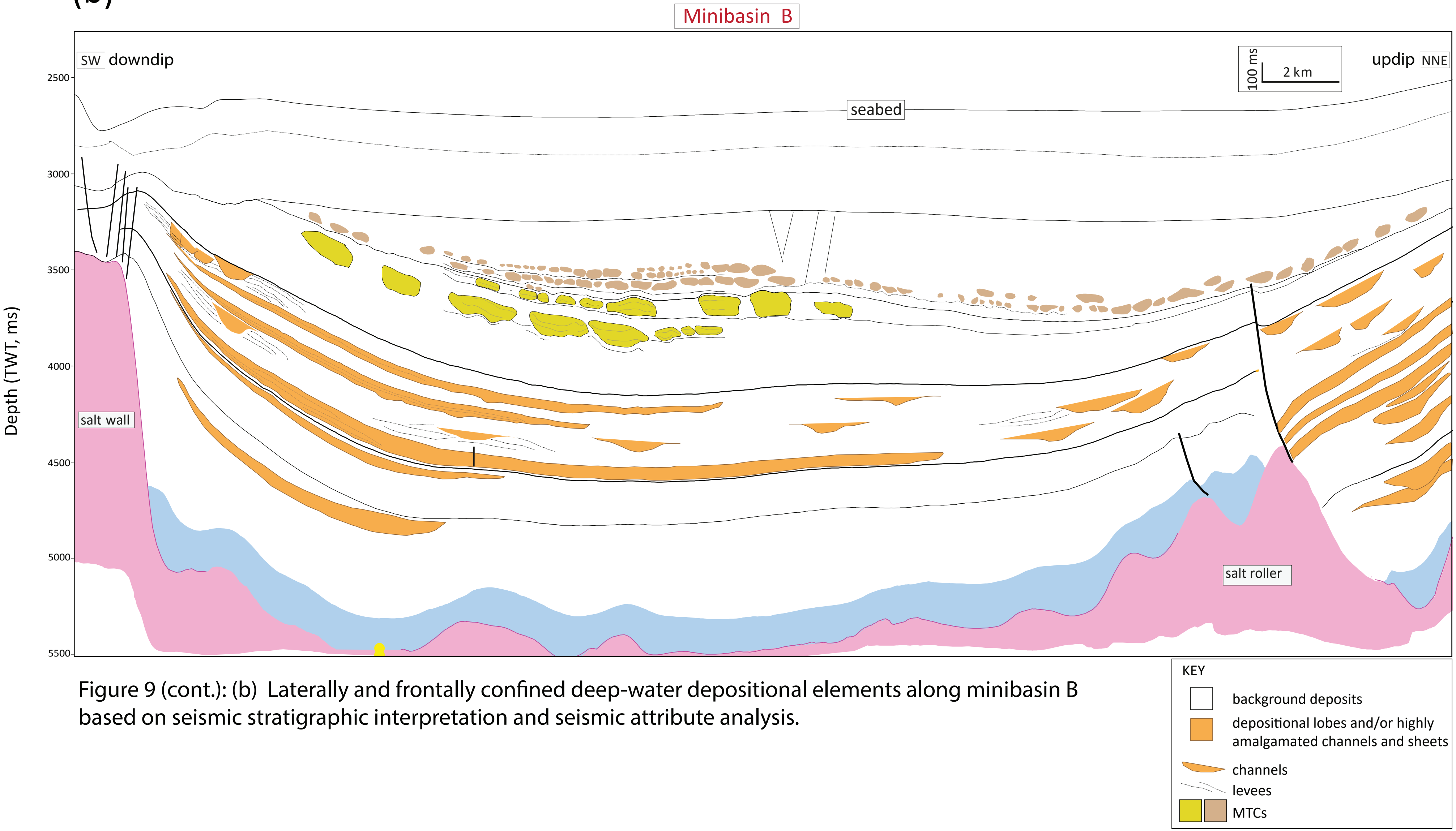

Figure 9 (cont.): (b) Laterally and frontally confined deep-water depositional elements along minibasin B based on seismic stratigraphic interpretation and seismic attribute analysis.

(c)

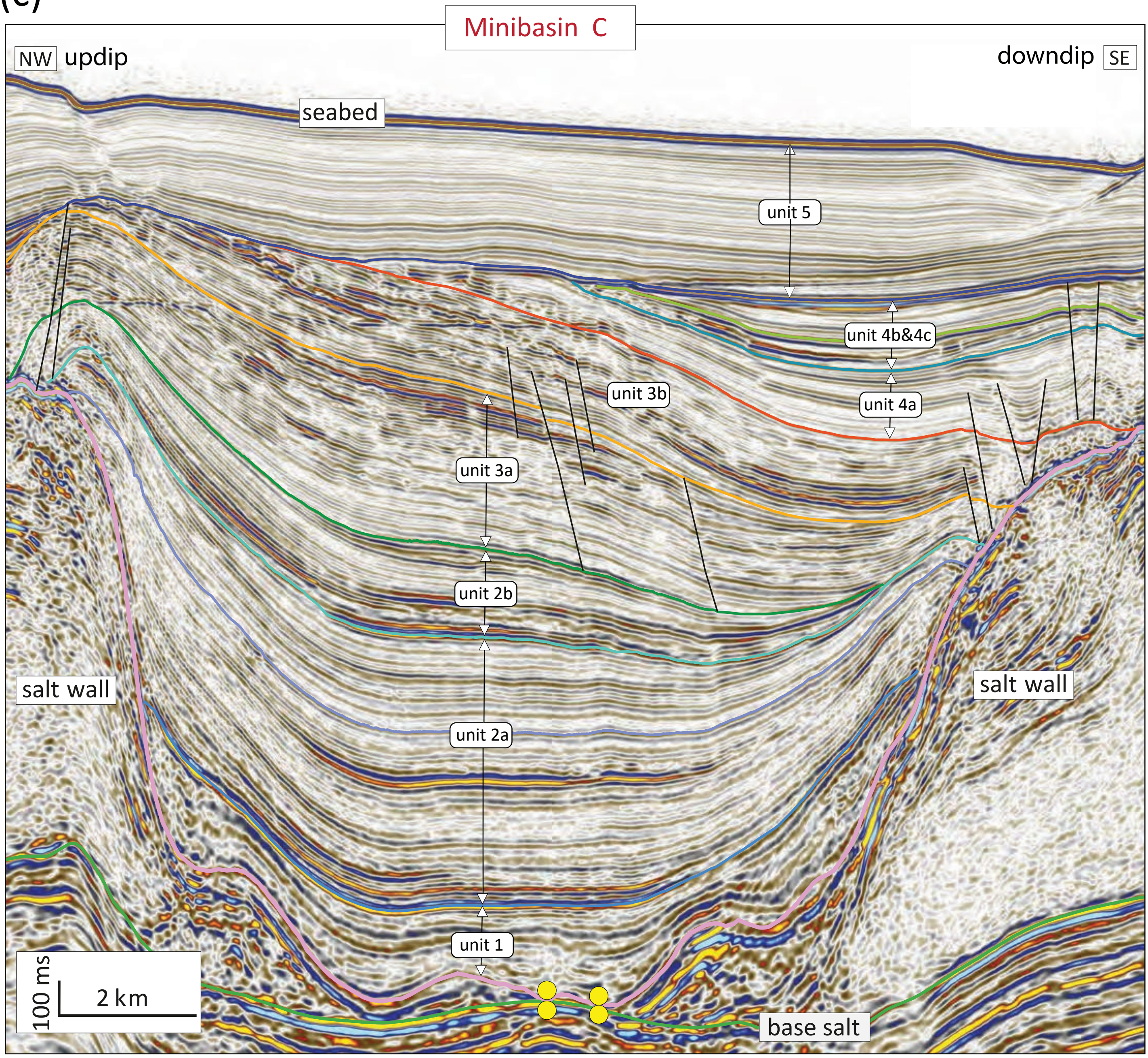

Figure 9 (cont.): (c) Seismic profile across Minibasin C illustrating the main units interpreted. Initial confinement is illustrated by thinning and onlapping of minibasin stratigraphy towards the downdip (SE) salt wall (units 2a, 2b and 3a) . Minibasin filling and welding led to inversion of the minibasin stratigraphy (units 2a, 2b, and 3a), and spilling and shifting of the initial depocenters from Minibasin B towards the SE and downdip minibasins (units 3b and 4). See location of seismic profile in Figure 8

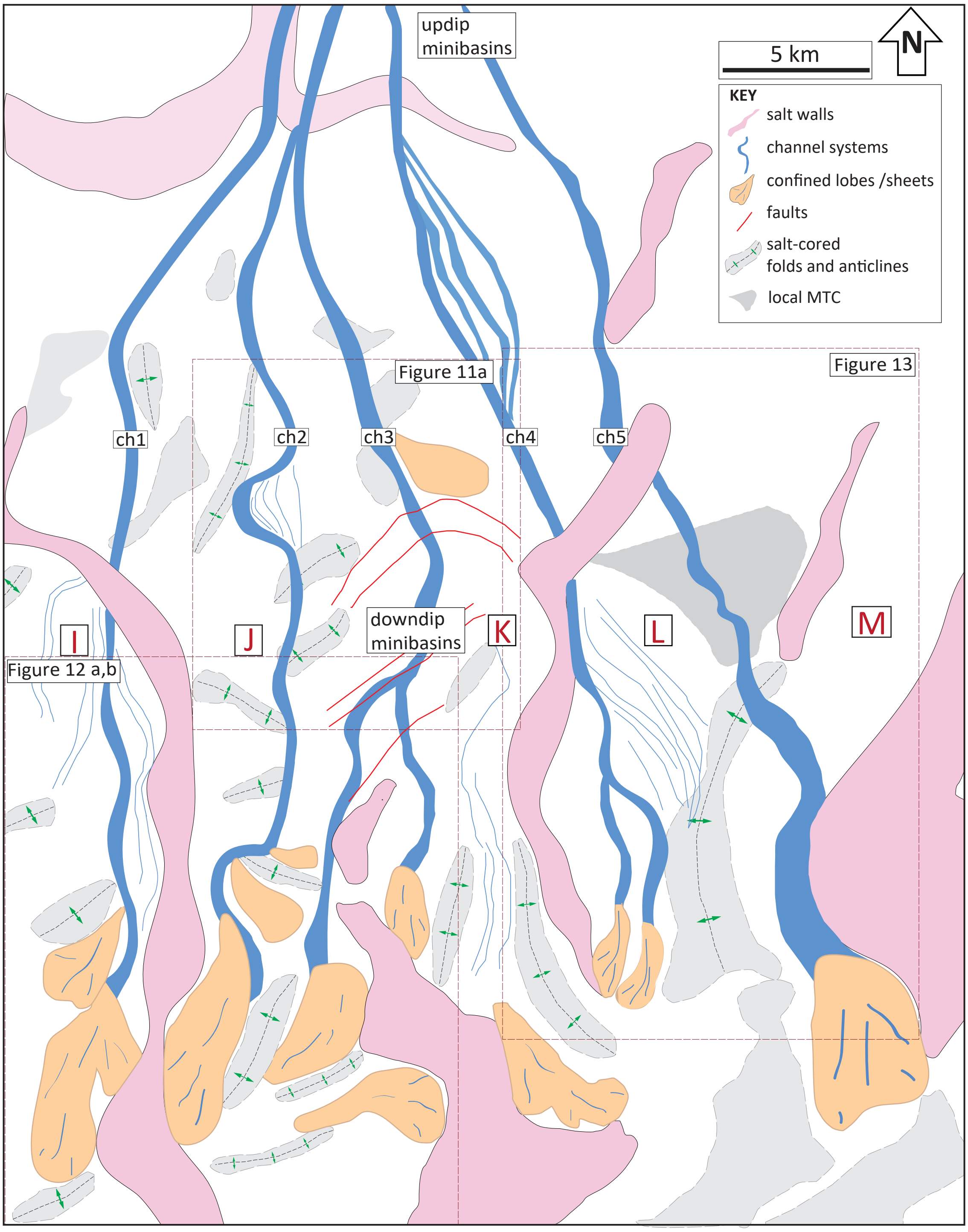

FIGURE 10: Deep-water depositional systems and distal downdip minibasins (I, M) in the Inner São Paulo Fold Belt and the São Paulo Plateau. Updip, channel systems are relatively linear and unconfined. Local variations in architecture are controlled by salt-cored folds and anticlines and salt walls. Lateral and frontal confinements is observed downdip. See area location in Figure 6c. Interpretation is based on seismic stratigraphy, geomorphology, seismic attributes and thickness maps. Detailed isochrons, attribute maps, and seismic sections are shown in Figures 11-14.

(a)

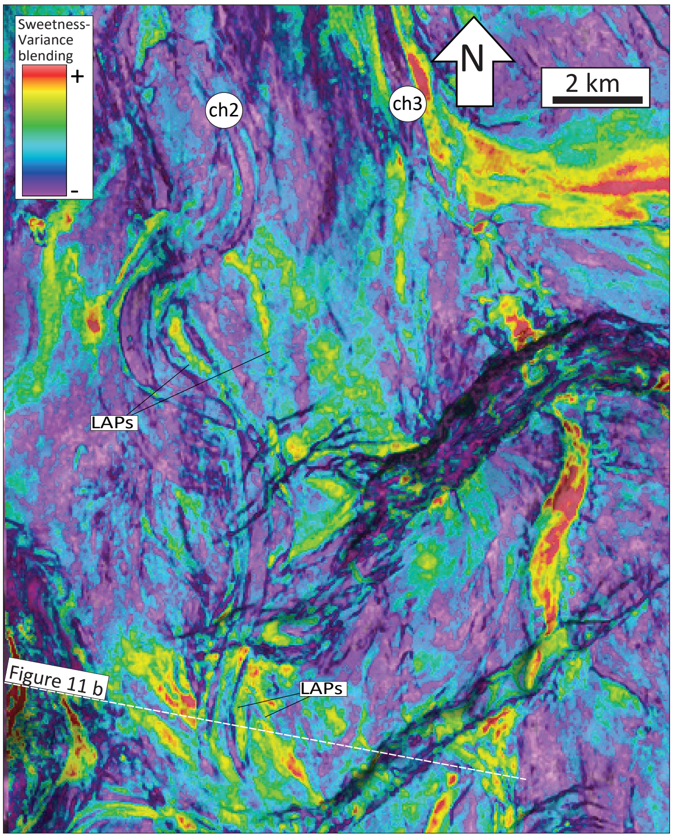

(b)

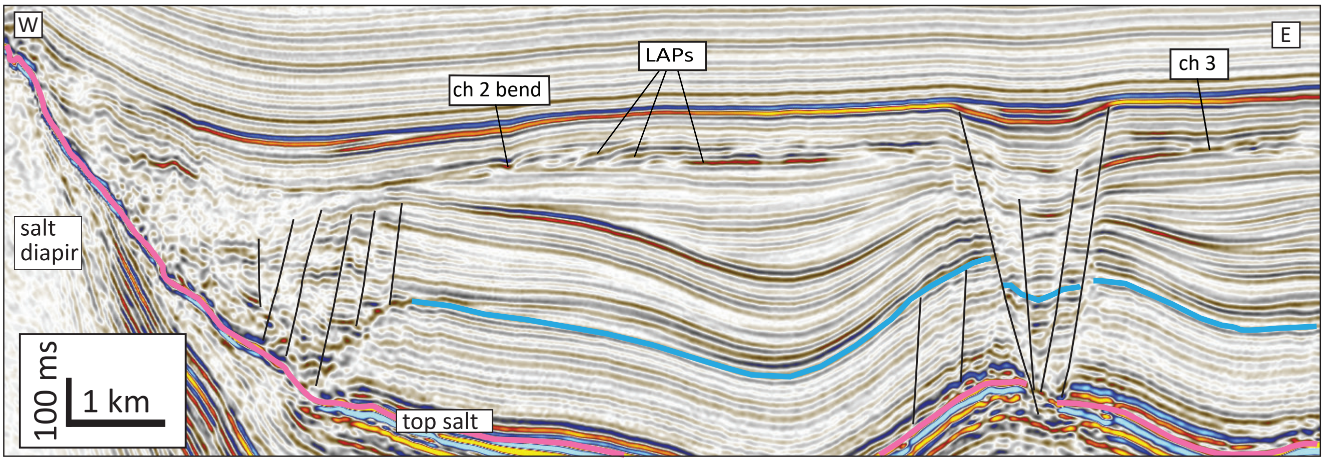

FIGURE 11: (a) Sweetness and variance blending illustrating local increase in channel sinuosity and lateral accretion packages described in Table 3. See channel 2 location and associated structural elements in Figure 10. (b) Seismic section illustrating channel bend and high-amplitude lateral accretion packages. See Figure 11a for location of seismic section.

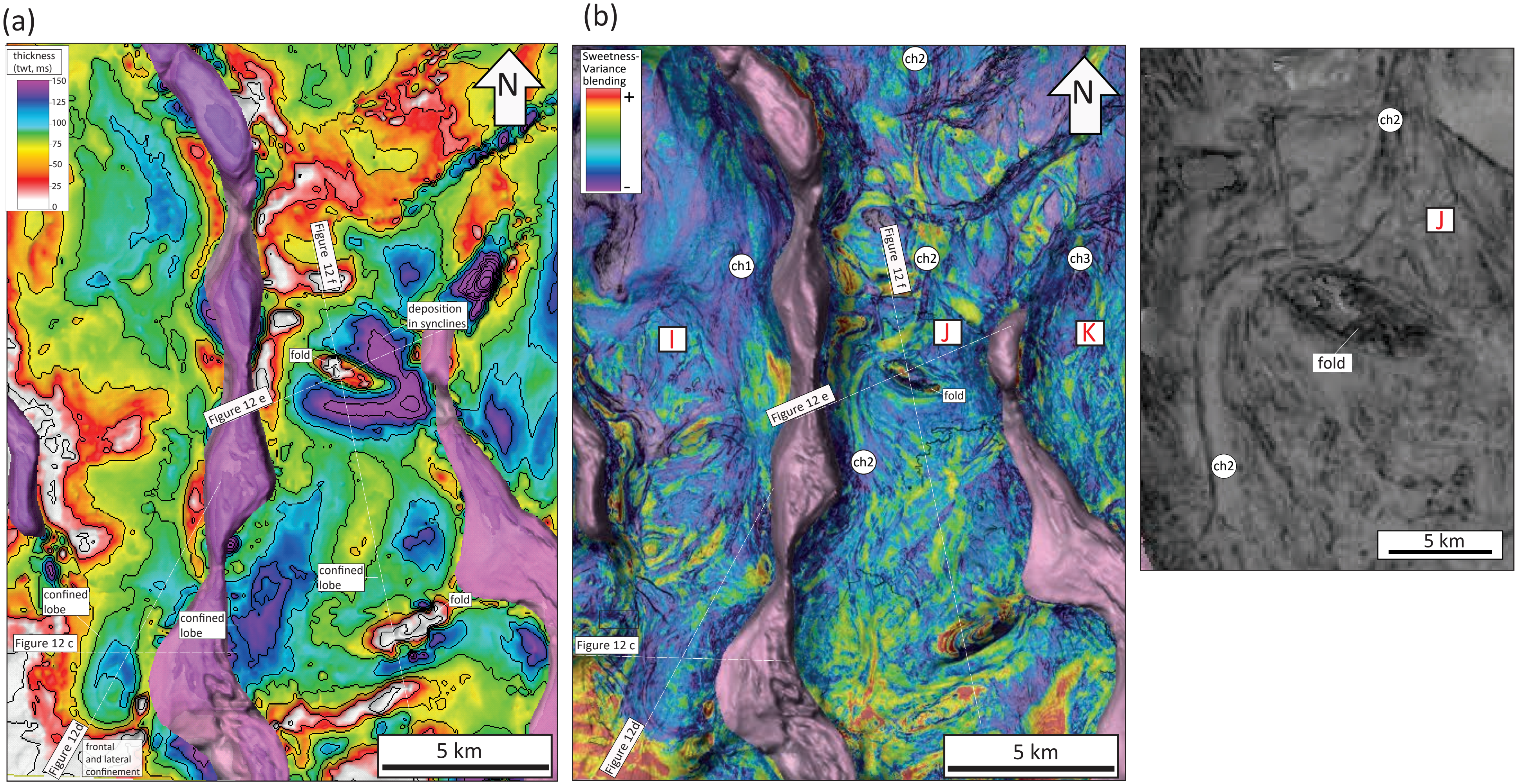

FIGURE 12: Isochron (a) and seismic attribute blending (b) for unit 3 covering minibasins I and J illustrating salt-related controls on coeval deep-water depositional systems. Increase in thickness occurs around salt-cored folds and associated to lobes deposition where frontally confined. Deflection of submarine channel 2 (ch2) occurs around a salt-cored fold in Minibasin J and this is highlighted in the amplitude contrast attribute in the inset. See interpretation and location in Figure 10. (c) and (d): Seismic sections across the distal part of minibasin I, illustrating lobes deposition and confinement. (e) and (f) Seismic sections across and along minibasin J. illustrating salt-related controls on deposition. Location of seismic sections are highlighted in Figures 12 a and b

FIGURE 12

Minibasin I

(c)

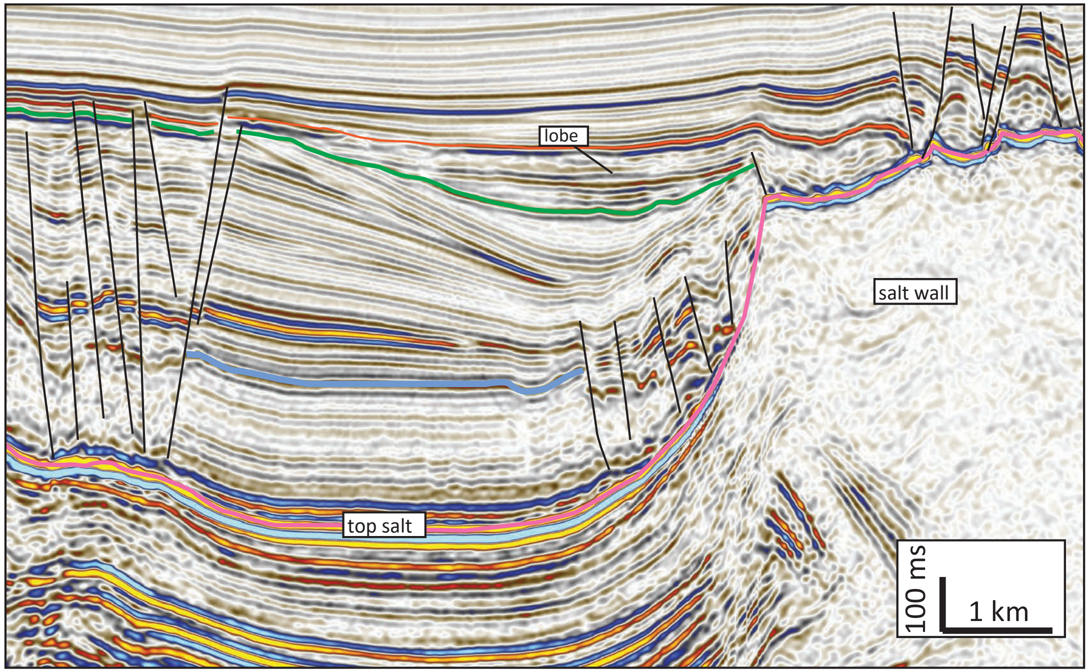

(d)

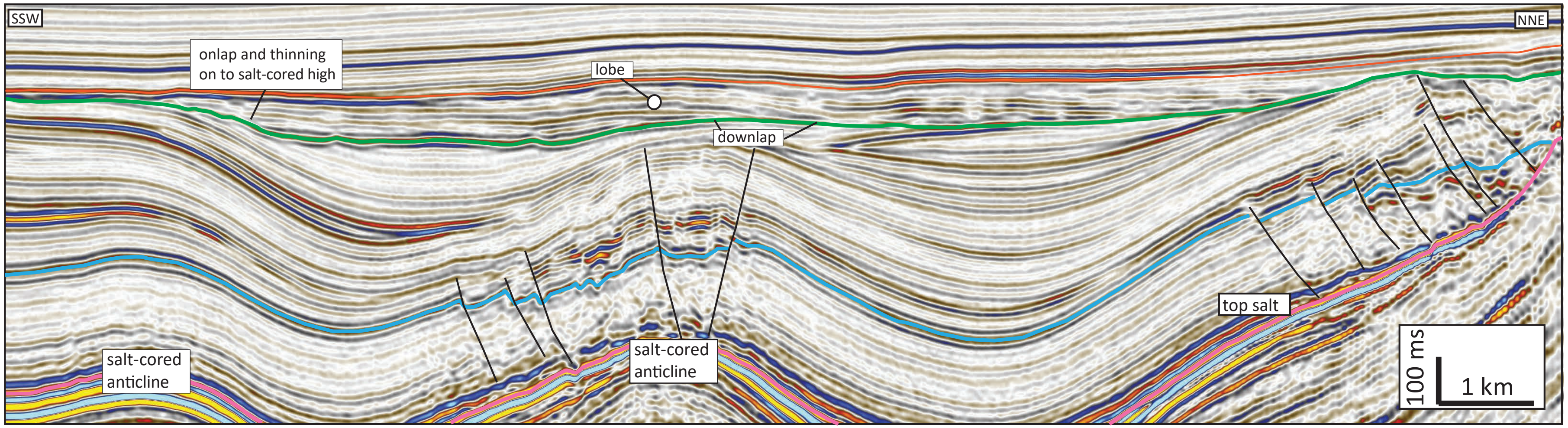

(e)

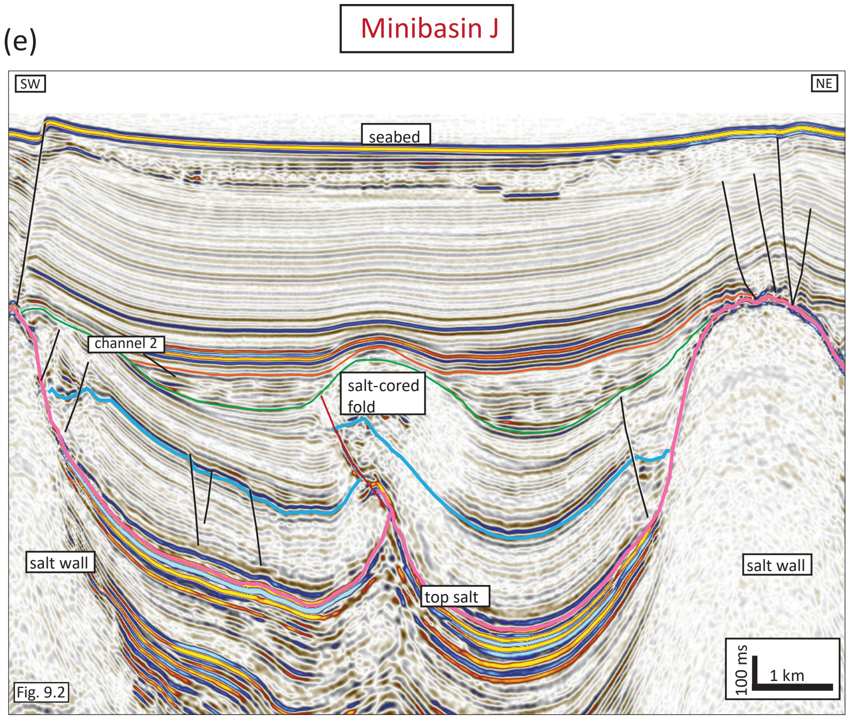
Minibasin J
SW
NE
seabed
channel 2
salt-cored
fold
salt wall
salt wall
top salt
100 ms
1 km
Fig. 9.2

(f)

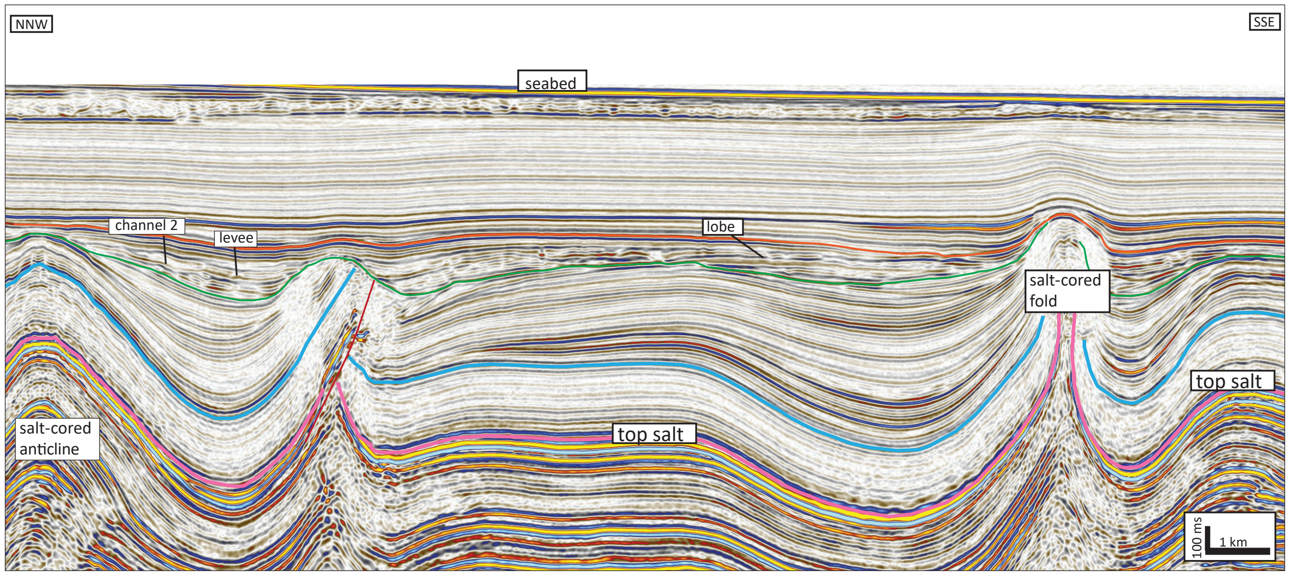
NNW
SSE
seabed
channel 2
levee
lobe
salt-cored
fold
top salt
top salt
salt-cored
anticline
100 ms
1 km

FIGURE 12

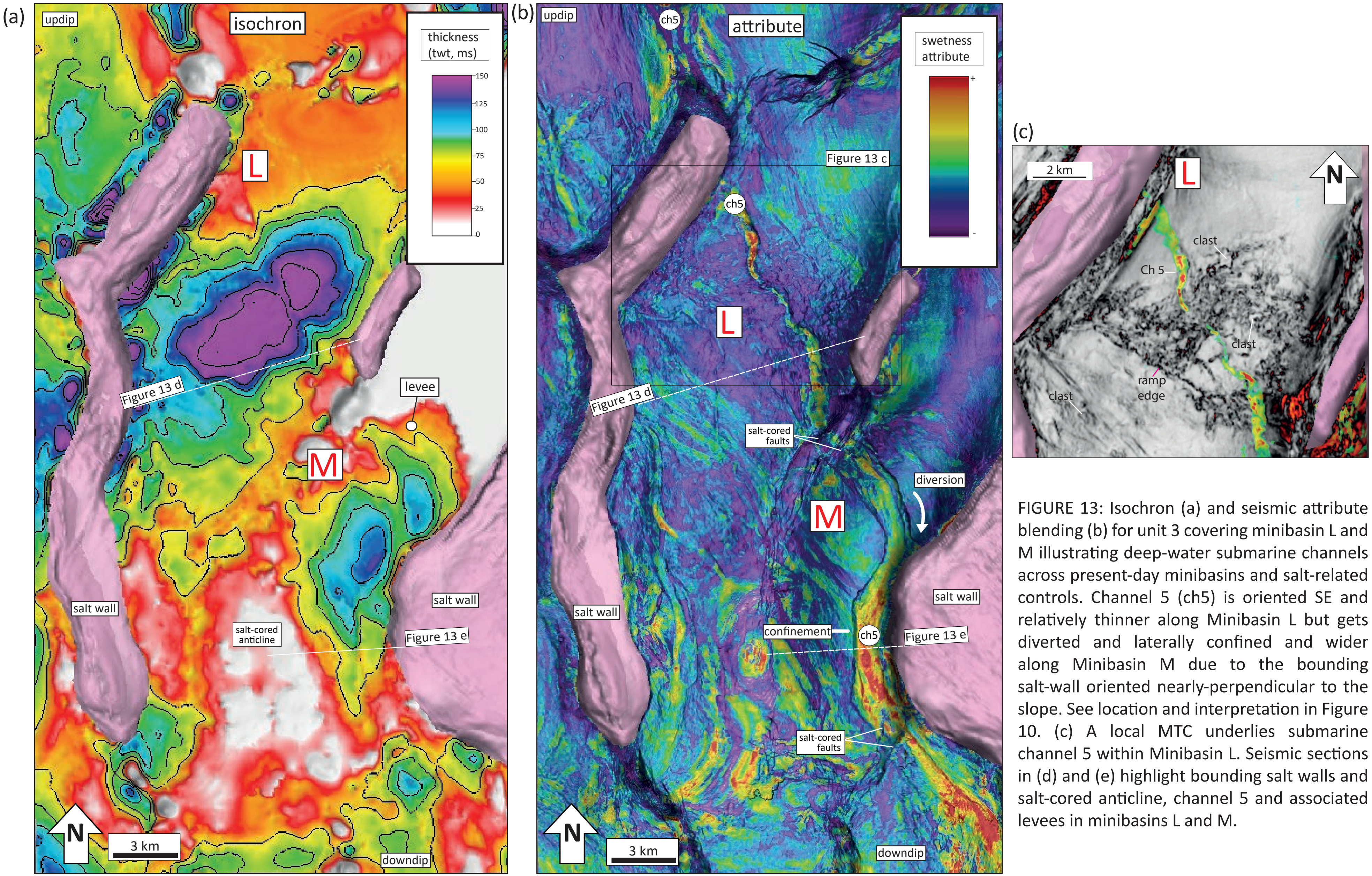

FIGURE 13: Isochron (a) and seismic attribute blending (b) for unit 3 covering minibasin L and M illustrating deep-water submarine channels across present-day minibasins and salt-related controls. Channel 5 (ch5) is oriented SE and relatively thinner along Minibasin L but gets diverted and laterally confined and wider along Minibasin M due to the bounding salt-wall oriented nearly-perpendicular to the slope. See location and interpretation in Figure 10. (c) A local MTC underlies submarine channel 5 within Minibasin L. Seismic sections in (d) and (e) highlight bounding salt walls and salt-cored anticline, channel 5 and associated levees in minibasins L and M.

FIGURE 13 (cont)

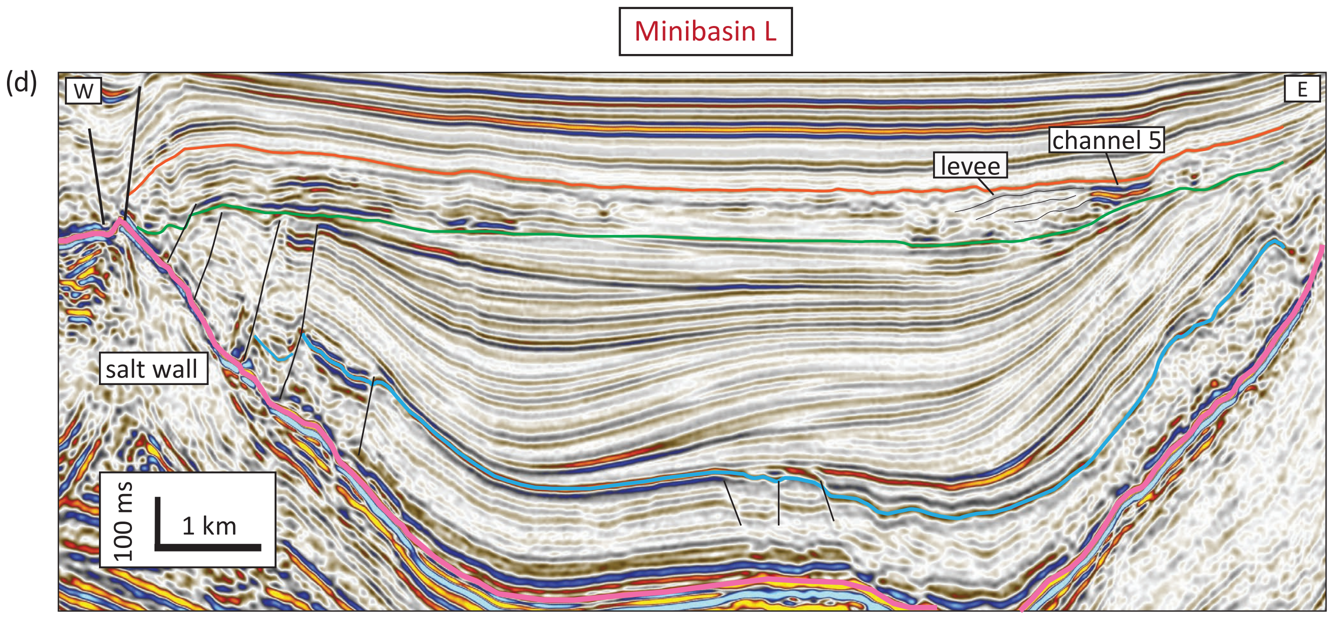

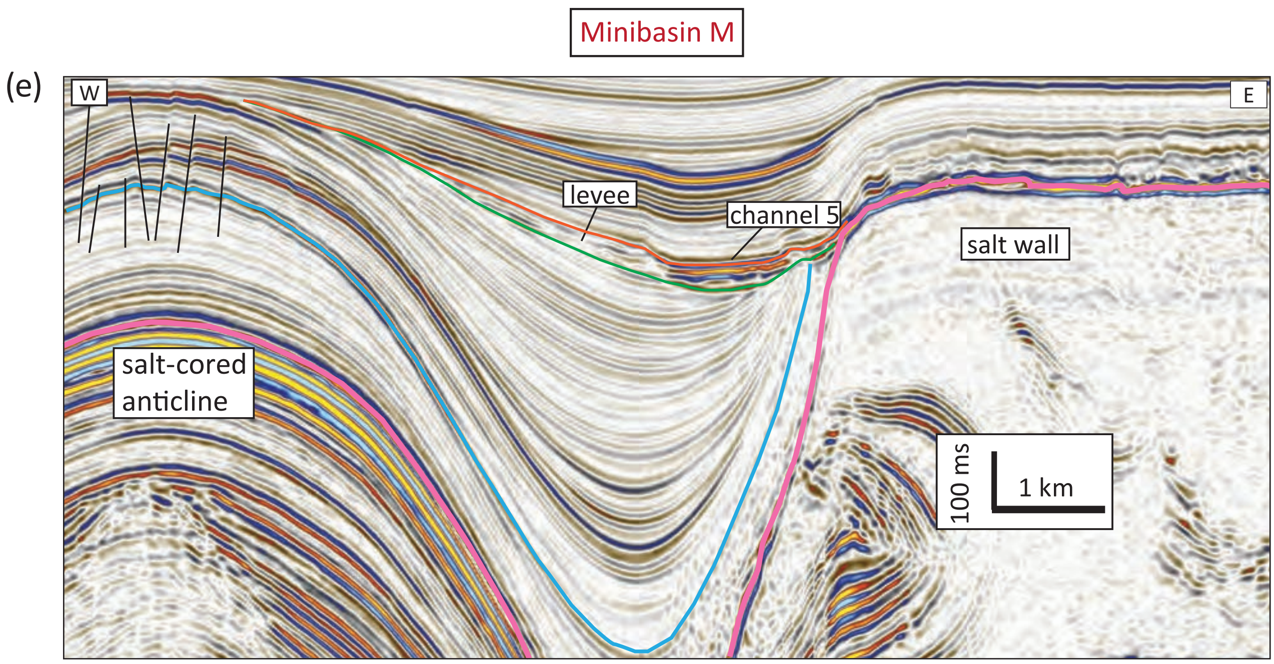

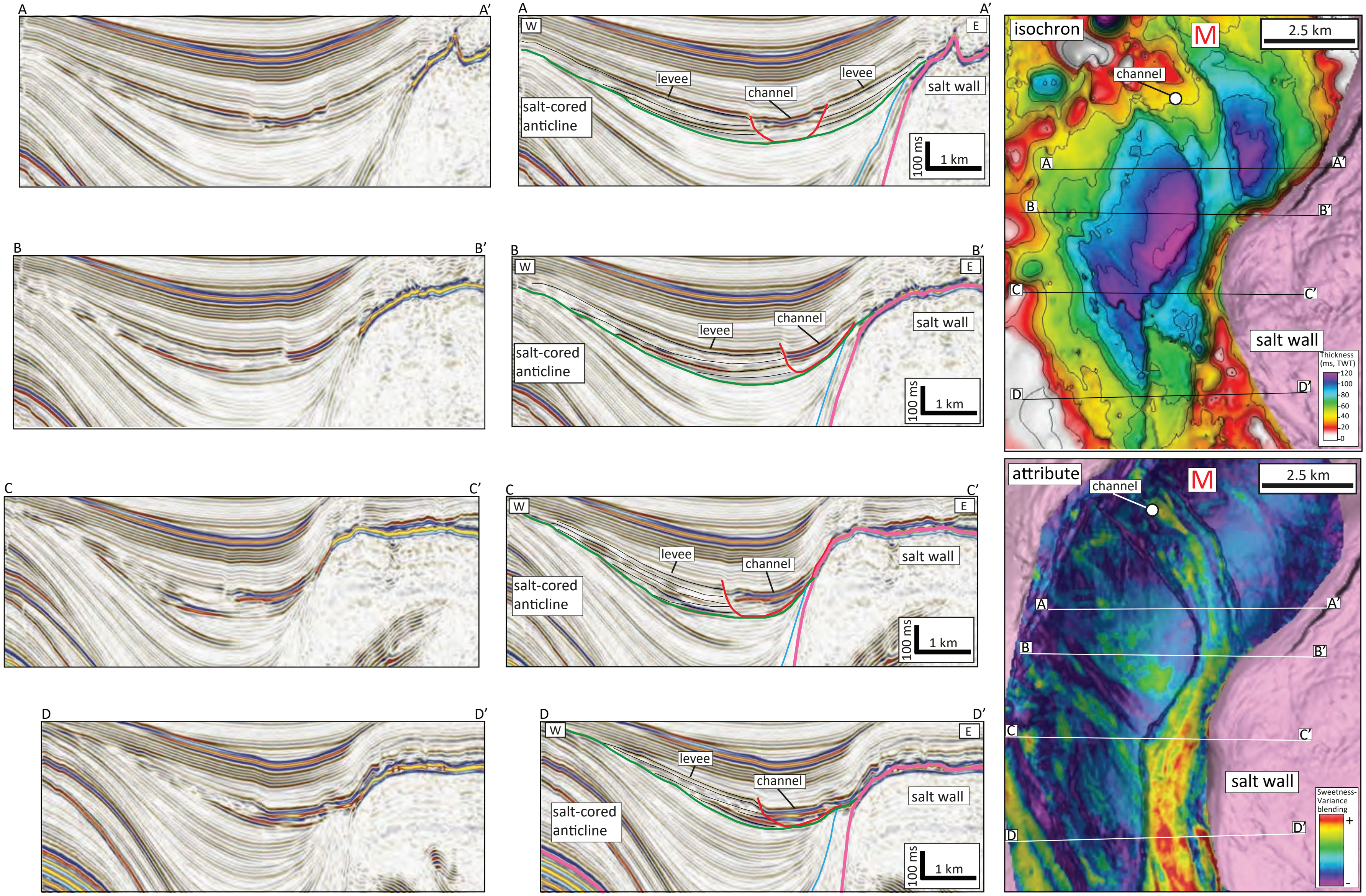

FIGURE 14: : Submarine channel and levee geometry variations along Minibasin M. Isochron and section A-A' illustrate wing-shaped levees developed adjacent to the channel. Seismic attribute and sections illustrate that high-amplitudes are restricted to the channel axis, whereas the levees are characterized by medium to low amplitudes. Channel onlaps and its apparently tilted and rotated where it gets diverted and closer to the bounding salt wall (section B-B'). Intra-levee reflections are rotated towards the channel axis (sections C-C' and D-D') indicating salt movement during deposition

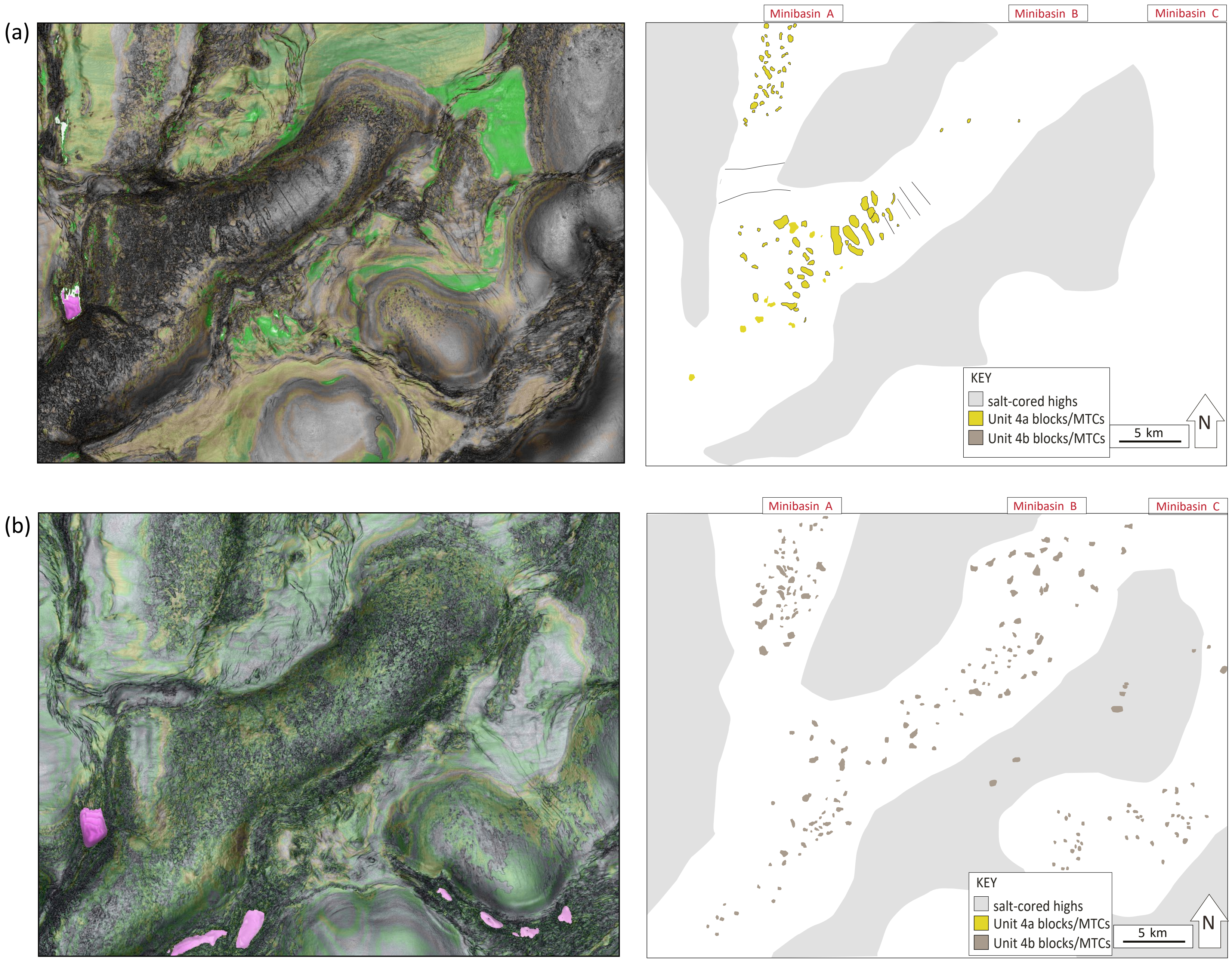

FIGURE 15: Seismic attributes sweetness and variance blending and interpretation of intra-minibasin clasts characterizing MTCs in proximal updip minibasins during deposition of Unit 4. See location of minibasins A, B and C in regional map Figure 6c and seismic and geoseismic sections in Figures 9a and 9b.

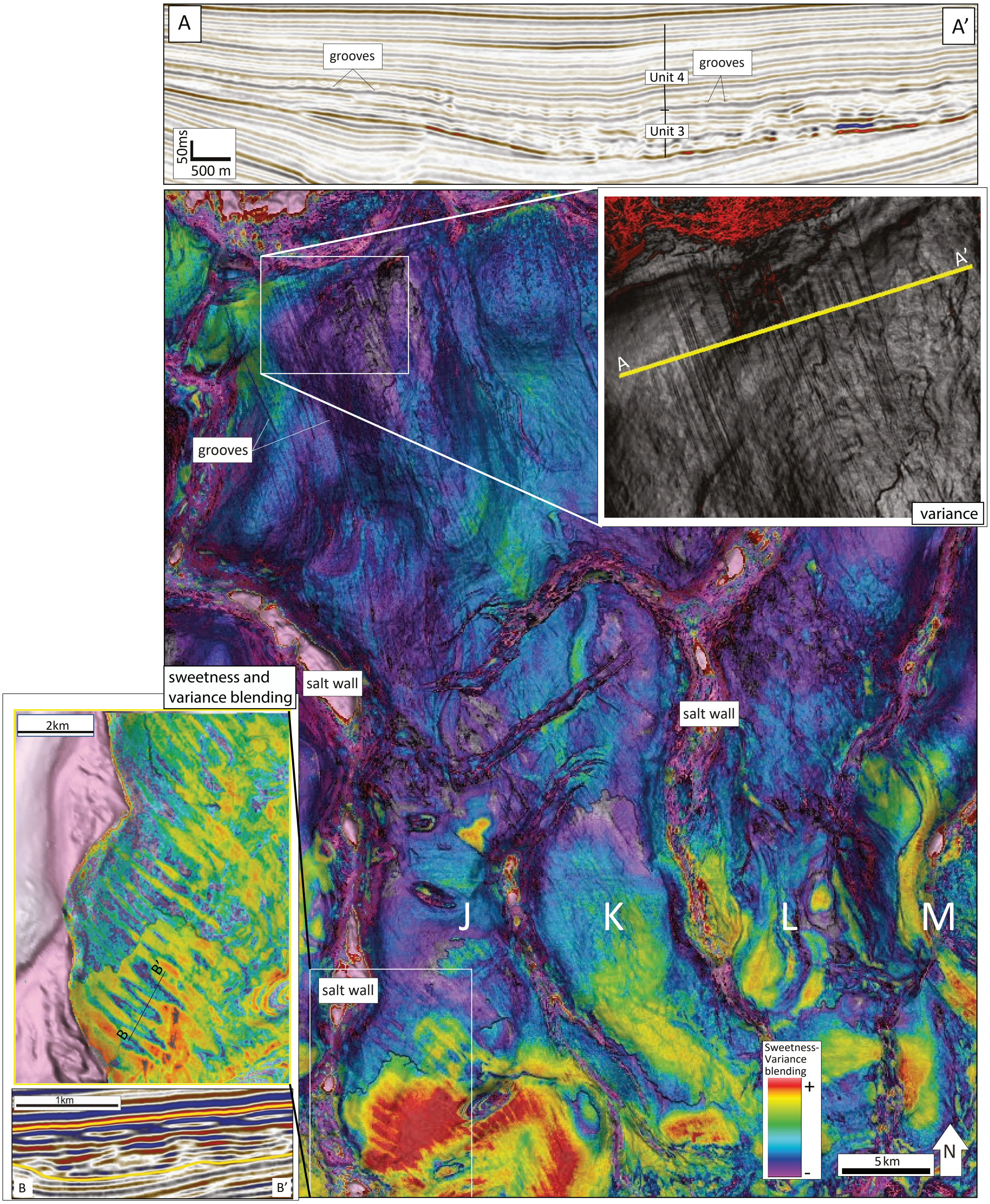

FIGURE 16: Seismic attributes and seismic sections illustrating linear grooves characterizing regional-scale MTCs across the Sao Paulo inner fold-belt and the Sao Paulo plateau and highlighting a drastic change in the evolution of the central deep-water Santos Basin during deposition of Unit 4. See location of minibasins J, K, L, and M in regional map Figure 6c

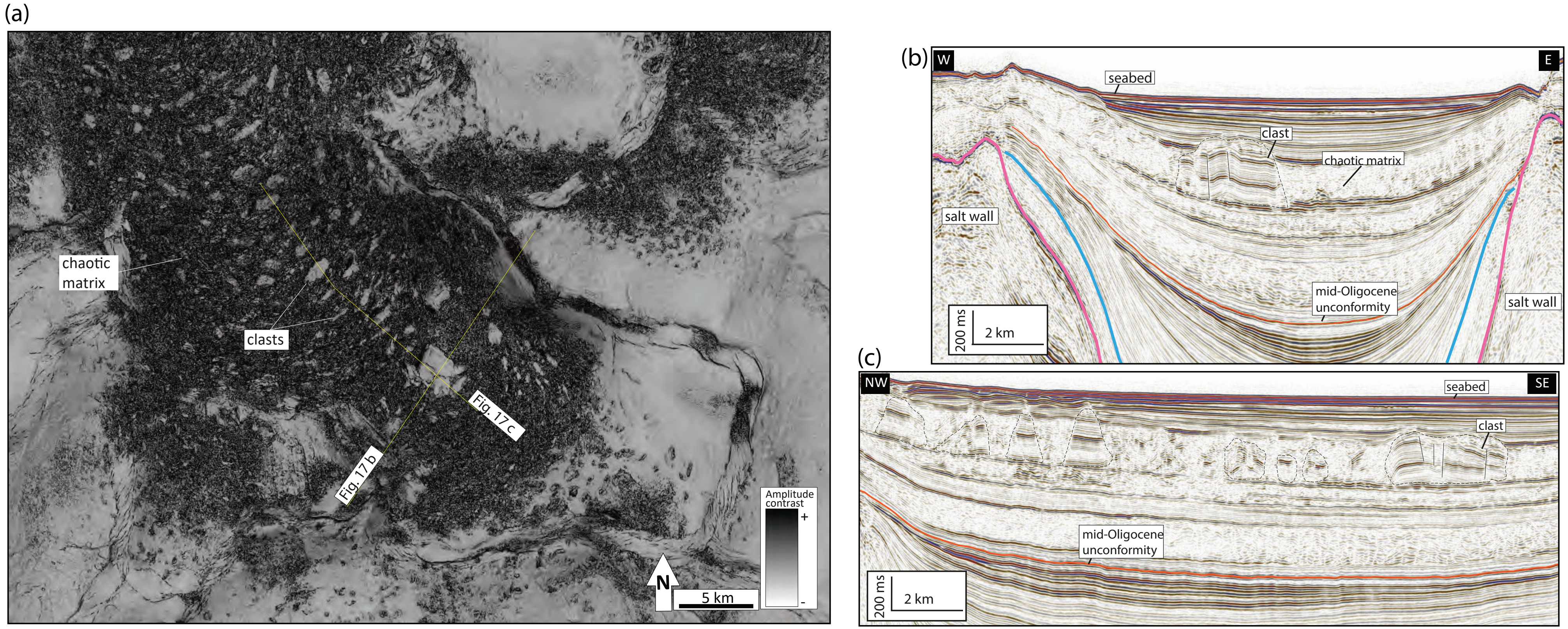

FIGURE 17: Seismic expression of MTCs within Unit 5. a) Amplitude contrast attribute of intra-Unit 5 horizon highlighting clasts and a chaotic matrix; b) seismic section across the minibasin; c) seismic section along the minibasin.

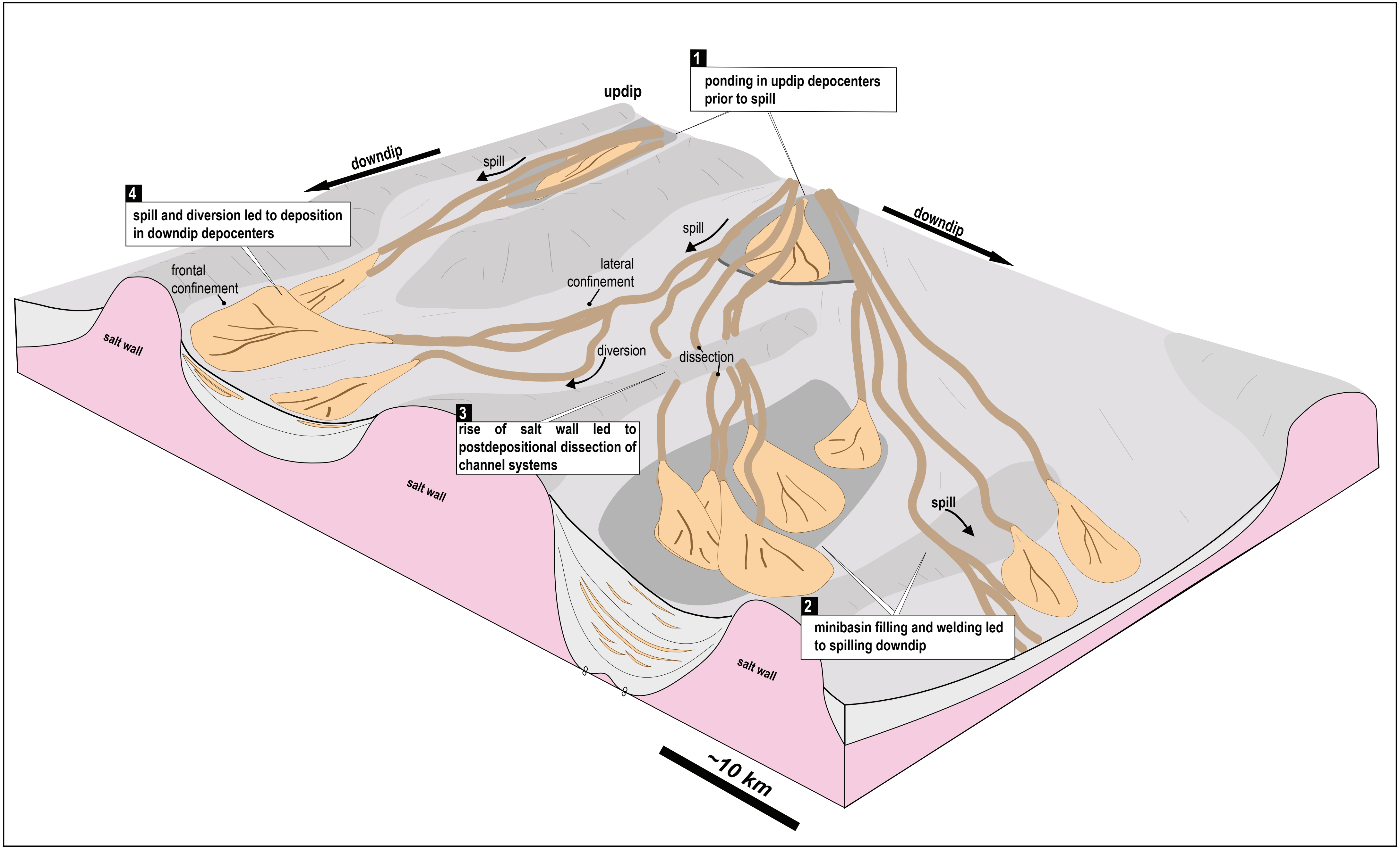

FIGURE 18: a) Block diagram illustrating sedimentation within proximal minibasins: Ponding occurs within proximal, updip, intra-minibasin depocenters prior to spilling and deposition along the minibasins (1). Filling of minibasins and subsequent welding of minibasin floor led to spilling towards downdip minibasins (2). Channel systems are post-depositionally dissected by rising salt walls bounding the present-day minibasins (3). Subsequent spilling from updip depocenters and diversion by rising salt walls led to deposition in downdip depocenters (4).

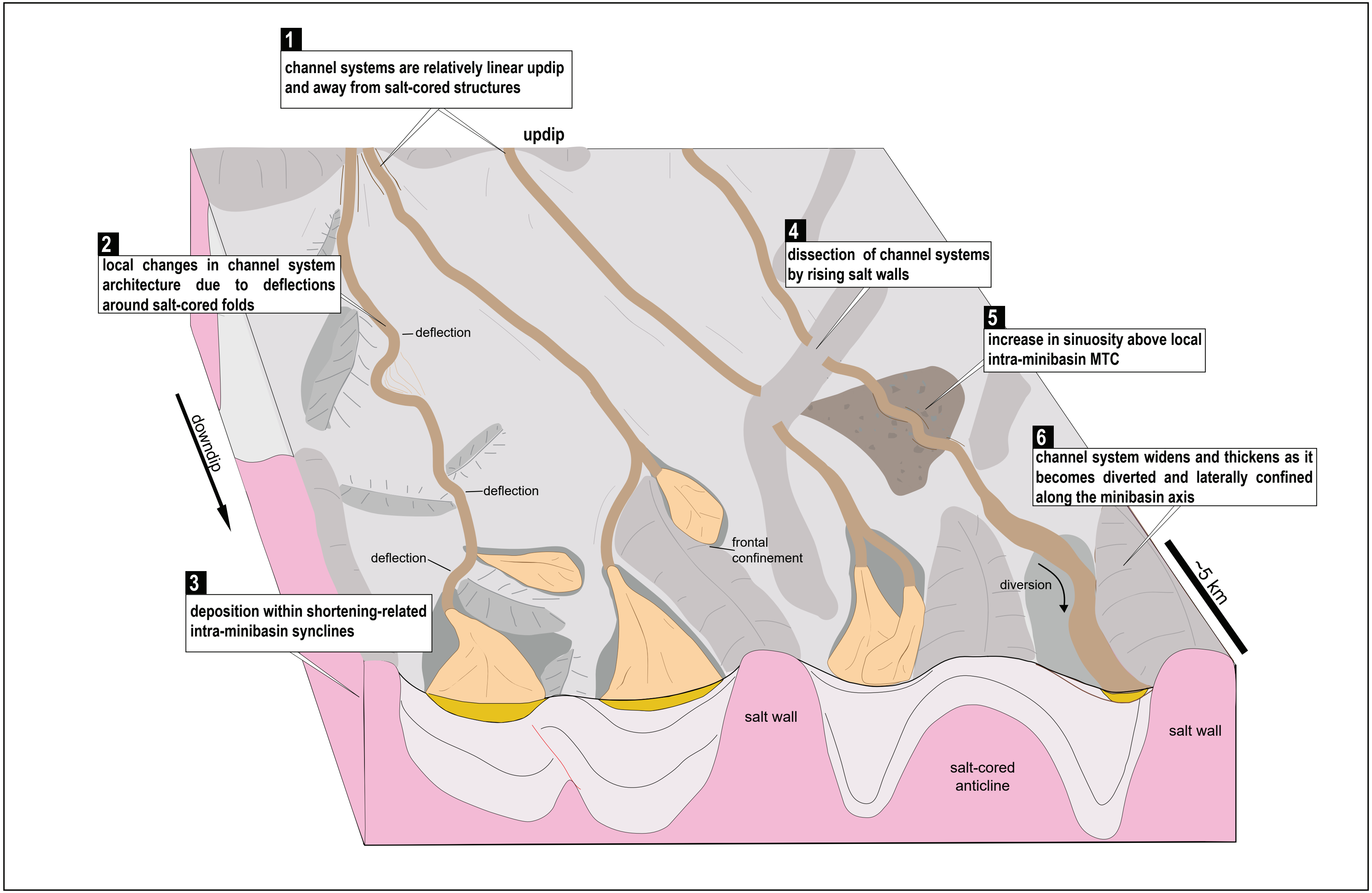

FIGURE 18 (cont.): b) Block diagram summarizing salt-related controls in deep-water sedimentation across part of the São Paulo inner fold-belt and the distal minibasins in the São Paulo plateau. Channel systems spilling from the proximal minibasins are relatively linear updip and away from salt-cored structures (1). Local controls in channel system architecture (2) and sediment distribution (3) are observed. Present-day salt walls dissected channel systems similarly to what it is observed in the updip minibasins (4). The architecture of channel systems varies between adjacent minibasins controlled by the presence of intra-minibasin MTCs and confinement (5 and 6).

TABLE 1: Vertical seismic resolution of intervals of interest and accross structural domains

Structural Domains	Borehole	Formation	Interval Velocity (m/s)	Frequency (Hz)	Resolution (m)
Proximal deep minibasins	329D	Marambaia	2125	52	10
		Itajai-Acu	3525	37	24
		Itanhaem	4300	17	63
Medial shallow minibasins	369A	Marambaia	1700	37	11
		Itajai-Acu	2300	30	19
		Itanhaem	3700	23	42
Distal elongated minibasins	723C	Marambaia	1500	45	8
		Itajai-Acu	1900	42	11
		Itanhaem	2750	30	23
	709	Marambaia	1500	48	8
		Itajai-Acu	2200	42	13
		Itanhaem	2300	30	19

Table 2: Seismic facies interpretation and seismic attributes calibration with lithology from borehole 329D, minibasin C. See Figure 4a for location

Seismic facies	Amplitude	Continuity	Swetness attribute response	Variance attribute response	Lithology proportions (borehole 329D)
SF1	High	Variable	Moderate to high (light blue to red colors)	Low (grey to white colours)	40% sandstone 56% mudstone 4% siltstone, marlstone and carbonate
SF2	Modetate to high	Discontinous	Medium (light blue)	High (black colour)	56% sandstone 28% mudstone 16% marlstone and carbonate
SF3	Low	Continuous	Low (dark blue to dark pink colors)	High (black to red colors)	70% mudstone 25% sandstone 5% marlstone and carbonate

Deepwater depositional elements					
	Seismic Stratigraphy	***Seismic geomorphology***	***Reflection character***	***Geometry***	***Interpretation***
Channels	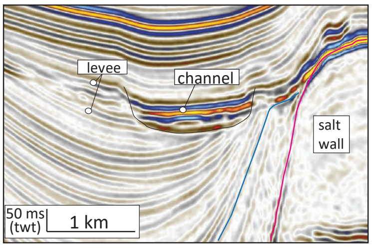	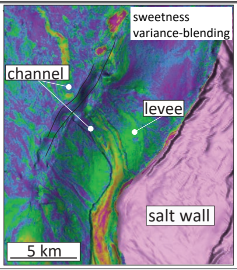	Parallel, continuous, moderate-to-high amplitude seismic reflections. Some low-amplitude channels also occur Bases are flat and weakly erosional 20-150 m thick	Relatively narrow, elongate, low sinuosity, channel forms 0.2 - 3 km wide up to 200 km long sinuosity (<1.5)	Turbidite-fed submarine channels (e.g., Kolla et al. 2000; Fonnesu, 2003; Prather, 2003; Gee and Gawthorpe; 2006, 2007; Alves et al., 2009) Sandstone-prone channel-axis if defined by SF1 (Table 2). Siltstone and mudstone-prone if defined by SF3 (Table 2)
	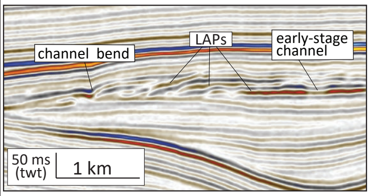	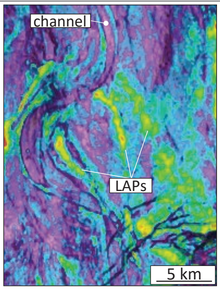	Laterally stacked moderate-to-high amplitude seismic reflections dipping in towards the channel axis up to 50 m thick	Crescent-shaped forms flanking the inner bend of more sinous channels up to 1 km wide up to 5 km long	Lateral accretion packages developed due to channel lateral migration (e.g., Kolla et al., 2000; Abreu et al. 2003; Janocko et al. 2013) Sandstone or siltstone prone when defined by SF1 seismic facies (Table 2)
Levees	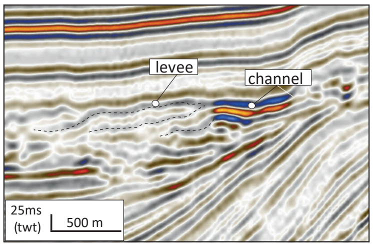	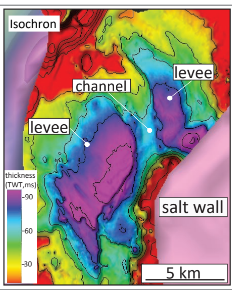	Wedge-shaped seismic packages of subparallel, low-to-moderate amplitude seismic reflections adjacent to the channels up to 150 m thick but typically thinner	Asymmetrically developed on both sides of the channel axis up to 5 km wide up to 10 km long	Levees deposited by sediment gravity-currents that escaped from submarine channels (e.g. Fonnesu, 2003; Gee and Gawthorpe, 2007; Clark and Cartwright, 2011; Ortiz-Karpf et al., 2015) Generally fine-grained mudstone or siltstone composition based on seismic facies SF3 (Table 2)
Lobes	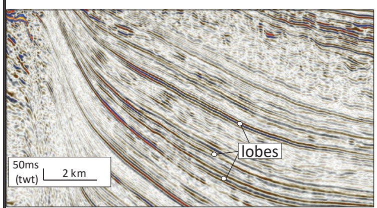	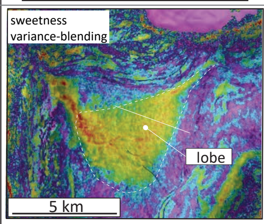	Tabular to mounded packages of subparallel, continous, moderate-to-high amplitude seismic reflections thinning towards the fringes downlap up to 200 m thick	Sub-rounded, to lobate to elongate up to 5 km wide up to 10 km long	Lobes deposited at the mouth of submarine channels (e.g. Gee and Gawthorpe, 2006; Saller et al., 2008; Prélat et al., 2010) Largely composed of sandstone based on high amplitude and evidence of differential compaction
MTCs	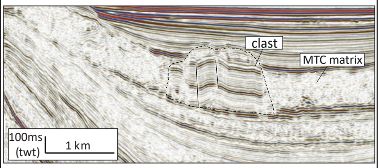	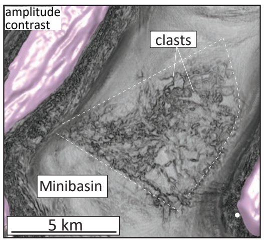	Discontinous to chaotic, low-to-moderate amplitude seismic reflections up to 200 m thick Basal surfaces are sharp and not erosional or highly irregular with v-shaped grooves Clasts are parallel continous moderate-to-high-amplitude reflections. Up to 200 m thick	Fan-shaped or subparallel lineations up to 50 km long Semi-circular to angular clasts of varios sizes: 0.1 to 200 m wide 0.2 to 1 km long	Mass transport complexes (e.g., Posamentier and Kola, 2003; Gee and Gawthorpe, 2006, 2007; Gamboa et al. 2010; Jones et al. 2012; Oluboyo et al. 2014) Variable composition based on seismic facies (SF2 and SF3, Table 3)
Background deposits	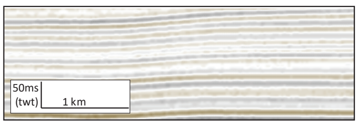	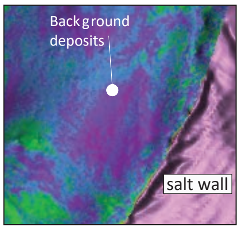	Parallel, continous, low-to-moderate amplitude reflections	Continous with slight variations in seismic amplitudes	Fine-grained deep-water deposits emplaced by dilute turbidity currents or suspension setting (e.g., Hadler-Jacobson et al. 2007; Oluboyo et al. 2014)

Table 3: Seismic geomorphogic elements identified within the post-salt sequence in central deep-water Santos Basin. Interpretation is mainly based on the analysis of the seismic stratigraphy and seismic geomorphology